Morphology Evolution during Dealloying at High Homologous Temperature

by

Ke Geng

A Dissertation Presented in Partial Fulfillment
of the Requirements for the Degree
Doctor of Philosophy

Approved April 2017 by the
Graduate Supervisory Committee:

Karl Sieradzki, Chair
Peter Crozier
Candace Chan
Yang Jiao

ARIZONA STATE UNIVERSITY

May 2017

ABSTRACT

Dealloying, the selective electrochemical dissolution of an active component from an alloy, often results in nanoscale bi-continuous solid/void morphologies. These structures are attracting attention for a wide range of applications including catalysis, sensing and actuation. The evolution of these nanoporous structures has been widely studied for the case at low homologous temperature, T_H, such as in Ag-Au, Cu-Au, Cu-Pt, etc. Since at low T_H the solid-state mobility of the components is of order 10^{-30} cm^2s^{-1} or less, percolation dissolution is the only mechanism available to support dealloying over technologically relevant time scales. Without the necessity of solid-state mass transport, percolation dissolution involves sharp transitions based on two key features, the parting limit and critical potential.

Dealloying under conditions of high T_H, (or high intrinsic diffusivity of the more electrochemically reactive component) is considerably more complicated than at low T_H. Since solid-state mass transport is available to support this process, a rich set of morphologies, including negative or void dendrites, Kirkendall voids and bi-continuous porous structures, can evolve. In order to study dealloying at high T_H we have examined the behavior of Li-Sn and Li-Pb alloys. The intrinsic diffusivities of Li were measured in these alloys using electrochemical titration and time of flight measurements. Morphology evolution was studied with varying alloy composition, host dimension and imposed electrochemical conditions. Owing to diffusive transport, there is no parting limit for dealloying, however, there is a compositional threshold (p_{PD}) as well as a critical potential for the operation of percolation dissolution and the formation of bi-continuous structures. Negative or void dendrite morphologies evolve at compositions below p_{PD} and at large values of the applied electrochemical potential when the rate of dealloying is limited by solid-state mass transport. This process is isomorphic to dendrite

formation in electrodeposition. Kirkendall voiding morphologies evolve below the critical potential over the entire range of alloy compositions.

We summarize our results by introducing dealloying morphology diagrams that we use to graphically illustrate the electrochemical conditions resulting in various morphologies that can form under conditions of low and high T_H.

I dedicate this work to my parents for making me be who I am and my husband for his unconditional love, support and understanding during the past few years.

ACKNOWLEDGMENTS

Foremost, I would like to express my sincere gratitude to my advisor Prof. Karl Sieradzki for leading me into the field of materials science, for continuously supporting my Ph.D study and related research, for his encouragement, patience, persuasion, motivation and immense knowledge. Whenever I ran into trouble with my experiment, writing or courses, the door to Prof. Sieradzki's office is always open. Without Prof. Sieradzki's skillful guidance, innovative ideas and insightful discussions and suggestions, this dissertation would not have been possible.

I would also like to thank Prof. Peter Crozier, Prof. Candace Chan and Prof. Yang Jiao for serving as my committee members and providing many valuable feedbacks. I am very grateful to my mentors and labmates Dr. Shaofeng Sun, Dr. Xiaoqian Li, Dr. Nilesh Badwe, Dr. Qing Chen, Dr. Allison Handler, Dr. Minglu Liu, Ashlee Aiello, Erin Karasz and Julia Fisher for all electrochemical fundamental knowledge and experimental trainings and making my Ph.D. experience wonderful.

I am thankful that Xiying Chen has always been my friend, mentor and coworker ever since I started my project.

A very special gratitude goes out to National Science Foundation, Division of Materials Research; DMR-1306224 for providing the funding for this work.

TABLE OF CONTENTS

LIST OF TABLES

LIST OF FIGURES

Figure Page

Figure Page

CHAPTER 1

INTRODUCTION

1.1 Importance Of Dealloying Morphology Evolution

Dealloying, the selective electrochemical dissolution of an active component from an alloy, often results in nanoscale bi-continuous solid/void morphologies. As shown in Fig. 1.1, these structures are attracting attention for a wide range of applications including catalysis [1]–[3], super capacitors [4], composites [5]–[7], sensing [8]–[11], and actuation [12]–[15]. Erlebacher et al. [1] manufactured a high surface area nanoporous Ni-Pt (np-NiPt) alloy from electrochemical dealloying in Nickel (II) sulfate. np-NiPt impregnated with hydrophobic, high-oxygen-solubility and protic ionic liquid exhibited higher mass activity for the oxygen reduction reaction (ORR) compared with any other catalyst for this reaction in fuel cells. Stamenkovic et al. [2], [3] also proposed higher ORR catalytic properties of Pt-skeleton fabricated by dealloying in acidic electrolyte of Pt-M alloys, where M is Co, Fe or Ni. Cui's [4] group reported tunable distinct pore evolution in zinc oxide, silicon and silver nanowires. The pore size in nanoporous silicon nanowires was tuned by cycling. Compared to architectures incorporating activated carbon, the single crystal nanoporous Si nanowires showed energy and power densities of ∼20 Wh/kg and ∼22 kW/kg, respectively. Weissmüller and Wang [5] impregnated dealloyed nanoporous gold (NPG) with epoxy resin to form an nanocomposite material with near-metallic electric conductivity, with higher ductility and strength than either individual constituent phases. Weissmüller's group [6] also explored other polymer filler materials, including two epoxy resins and polyurethane, for impregnation of NPG made by dealloying. The composites were strong and deformable in compression and showed good tensile ductility. The strain evolution of these composites during compression testing was monitored by in situ X-ray diffraction and was found

to follow proposed micromechanics models in small ligament size while deviations from model results at larger ligament sizes were caused by coarsening defects [7]. Zhang et al. [8] immobilized probe with target DNA and reporter DNA on Au nanoparticle and NPG prepared by dealloying Ag from Ag-Au alloys in nitric acid. The DNA biosensor fabricated by hybridizing the target DNA with reporter DNA exhibited excellent selectivity and detectability. Seker et al. [9] investigated DNA detection performance of NPG in biofouling condition with different length scale of nanopores. The target DNA detection performance was reported to be better with coarsened NPG in Phosphate-buffered saline (PBS). While small pores exhibited enhanced detection performance with biofouling resilience in complex biological media (i.e., fetal bovine serum (FBS)). Seker [10] also reported NPG as a promising neural interface material to enhance long-term electrophysiological recording performance by showing the ability of NPG to tune astrocytic focal adhesion formation by tuning the length scale of ligaments in the NPG structure. Arnob et al. [11] demonstrated better molecular detection and identification of hydrocarbons on NPG disk substrates in the 1 – 2.5 μm near-infrared (NIR) wavelength range. The enhancement factor of first C-H combination band in NIR absorption spectroscopy using NPG was reported to be ~10^4. Biener et al. [12] invented a surface-chemistry-driven actuator based on NPG, whose surface stress tuned by surface oxygen coverage could result in reversible strain amplitudes in the range from 0.05 to 0.5 %. The theory of their NPG actuator is that alternating exposure of NPG to ozone and carbon monoxide could control the surface oxygen coverage. Cheng et al. [13] utilized double layered dealloyed nanoporous Nickel nanowire to fabricate a surface-charge induced actuator. Strain amplitude of 0.04 % controlled by cyclic voltammetry at voltage range of 0.6 V in 0.1 M NaOH electrolyte was obtained with high strain response time of 0.1 s and stable actuation performance beyond ~800 actuation loops. Jin and Weissmüller [14] reviewed

electrochemical actuation based on nanoporous Pt and Au samples. Under cyclic voltammetry, the change of sample dimension was in agreement with surface stress changes, which also agreed with density functional theory. Weissmüller's group [15] observed large reversible strain amplitudes (1.3 % and 0.35 % for nanoporous Au-Pt alloys with an oxygen-covered and clean surface, respectively). What's more, the high surface area and metallic nature of these materials being considered for anodes in lithium ion batteries (LIB) since the nanoscale dimensions could reduce mass transport distances and lower the propensity of cracking and fracture [16].

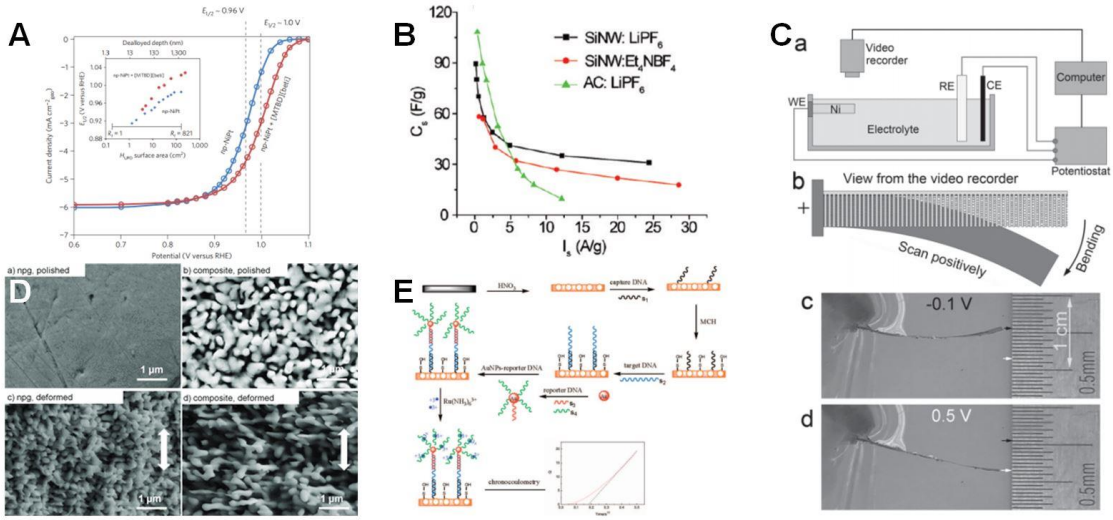

Figure 1.1. Review of applications of nanoporous materials formed by dealloying. A. Linear sweep voltammetry of dealloyed nanoporous Ni-Pt as a catalyst for oxygen reduction [1]. **B.** Capacitance as a function of current density compared between dealloyed Si nanowires and activated carbon [4]. **C.** Bending performance of an electrochemical actuator based on bi-layered dealloyed nanoporous Ni [13]. **D**. Comparison of compression deformation of NPG and NPG with epoxy resin [5]. **E.** The mechanism of DNA hybridization determination with a biosensor based on NPG and Au particles [8].

1.2 Dealloying Morphology Evolution At Low Homologous Temperature (Low T_H)

The evolution of these nanoporous structures has been widely studied for ambient temperature dealloying of high melting point alloy systems, such as Ag-Au, Cu-Au, Cu-Pt, etc [17]–[19]. For

dealloying performed at low homologous temperature, low T_H, solid-state diffusion is about 20 orders of magnitude too low to contribute to dealloying processes over technologically relevant time scales. Here our use of the term low T_H is meant to designate that the solid-state mobility of the component that is selectively dissolved is smaller than order 10^{-12} cm^2s^{-1}. "Percolation dissolution" first proposed by Sieradzki and Newman [20] is the operative atomic-scale mechanism for the morphology evolution of these systems since there is negligible solid-state mass transport occurring at ambient temperature.

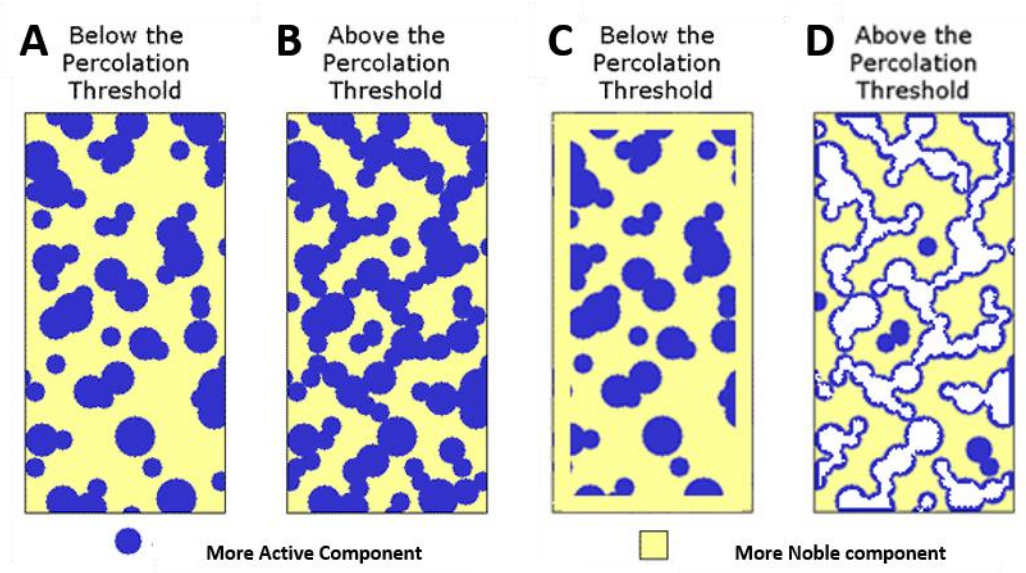

Figure 1.2. Cartoons showing cross-section views of noble-metal alloy systems before and after dealloying. **A-B**. Parent-phase alloy systems: **A**, isolated clusters of the active component below percolation; **B**, active paths of the active component above percolation. **C-D**. dealloyed morphologies: **C**, intact parent-phase alloy covered by a compact passivation layer of the noble atom; **D**, bicontinuous porosity.

The morphology evolution of alloy A_xB_y, at low T_H involves sharp transitions based on two key features, which are the parting limit and critical potential. The parting limit is the lower compositional threshold of less noble component, A, for dealloying to occur and bicontinuous porosity to evolve. In principle, the percolation threshold concentration is the lower bound of the

parting limit. However, for the noble metal alloys the parting limit is usually closer to 60 at.% of the more reactive component, whereas percolation thresholds are in the range of 20-30 at.% depending on crystal structure (number of nearest neighbors [21]. As shown in Fig. 1.2, when the A component is below the percolation threshold, A components form isolated islands in the parent-phase alloy, which cannot be fully dealloyed without the solid-state mass transport taking into place. Hence, only surface dealloying can occur resulting in a surface enrichment of the more noble alloy component and passivation. One possible explanation for why parting limits are larger than percolations thresholds is that near the percolation threshold the continuous paths are simply not large enough in diameter to allow electrolyte penetration and support the dealloying process. Another possible explanation is that with decreasing active component atom fraction the critical potential increases which eventually results in oxidation of the more-noble component. This oxidation reduces the surface mobility of this component, which can also result in void channels that re too narrow for electrolyte penetration.

The formation of bi-continuous porous morphologies also depends on the dealloying threshold (used here interchangeably with parting limit). A transition from surface dealloying to development of a macroscopic three-dimensional (3D) bicontinuous porous dealloyed structure occurs at a certain value of potential referred to in the literature as the critical potential, E_{crit}. At low potentials $E < E_{crit}$, dissolution of A proceeds via kink sites on ledges, which creates no new solid/liquid interfacial area. Owing to surface step fluctuations, A-atoms in terrace sites eventually find their way to kink sites from which they dissolve. Eventually, this leads to a surface highly enriched in the B component and passivation [22]. At high potentials ($E > E_{crit}$, dissolution of the more active component from surface terrace sites occurs resulting in new interfacial area owing to the creation of surface vacancies. This can be described by adding a

term to a standard form of the Nernst equation, $E = E_0 - \frac{RT}{nF} ln\left(\frac{a_{A^{n+}}}{a_A}\right)$($a_{A^{n+}}$ is the activity of A^{n+} in the electrolyte, a_A is the activity of A in the alloy, E_0 is the reversible potential adopted by elemental A, R is gas constant, T is temperature, n is the number of electrons transferred, and F is the Faraday's constant). This additional term describes the extra energy required to dissolve A atoms from terrace sites resulting in surface vacancy cluster injection. This term is given by $\frac{\gamma\Omega}{nq\xi}$ (γ is the solid/liquid interfacial free energy per unit area; Ω is the atomic volume of A; nq is the charge number associated with the dissolution process). ξ is the compositionally dependent average A-atom cluster size, $\xi = a(1+p)/(1-p)$,(Here a is the nearest neighbor spacing and p is the atom fraction of the dissolving component) taken from percolation theory [23]. The critical potential is given by, $E_{crit} = E - E_0 = \frac{RT}{nF} ln\left(\frac{a_{A^{n+}}}{a_A}\right) + \frac{\gamma\Omega}{nq\xi}$ [23], where the first term is overpotential predicted by Nernst equation and the second term is associated with injecting regions of negative curvature into the surface [23]–[25]. As seen in the quantitative formula for calculating E_{crit}, E_{crit} is a function of both the alloy and electrolyte composition.

Dealloying morphology evolution at low T_H could be summarized to be an interface controlled process with interplay of active component dissolution and noble element surface diffusion. This percolation dissolution governed process takes only noble element surface diffusion into consideration since bulk diffusion for noble metal alloys is negligible at room temperature [26]–[28].

1.3 Dealloying Morphology Evolution At High Homologous Temperature (High T_H)

While the dealloying morphology evolution with negligible solid state mass transport is well studied and understood, few attempts have been made to answer the question of how bulk

diffusion could affect dealloying morphology evolution. One way to answer this question is by monitoring dealloying morphology evolution of high melting temperature alloy systems at elevated temperature. There are relatively few works reported on elevated temperature electrochemical dealloying, where solid-state mass transport, such as lattice and grain boundary diffusion, is large enough to support/influence dealloying processes.

The anodic dissolution of Ag from Au-Ag alloys with Ag concentration of 88, 65 and 44 at.% in molten AgCl at 800°C with anodic potential of 0.2 V vs. Ag^{+}/AgCl was conducted by Harrizon and Wagner [29]. No microscopic examination of sectioned and etched samples was shown in their work. While no definitive statements could be made for the behavior of the 65 at.% Ag alloy, some type of porosity (stated as rugged penetration) was apparently observed for the 88 at.% Ag alloy and grain boundary penetration without transgranular penetration was shown in the 44 at.% Ag alloy.

Another way to investigate morphology evolution of dealloying at high homologous temperature, T_H, is by studying the morphology evolution of dealloying in low melting point alloys at ambient temperature.

Kaiser conducted selective dissolution of Indium (In) from $In_{0.05}Sn_{0.95}$, γ-InSn (20 at.% In) and β-InSn (80 at.% In) [30]. No images of dealloyed In-Sn alloy were provided. The void formation for β-InSn was attributed to the solid-state mass transport of In in the parent and product In-Sn phases. The dealloyed void morphology (not shown in the paper) was stated to be either Kirkendall porosity or a surface instability, which were resulted from diffusion process in single phase alloys. However, the rate-limiting step of dealloying was predicted to be a combination of charge transfer step from In^{+} to In^{3+} and In^{3+} transportation in the electrolyte. No critical

potential was observed for dealloying of $In_{0.05}Sn_{0.95}$. What's more, the availability for dealloying to happen in $In_{0.05}Sn_{0.95}$ with In composition as low as 5 at.% indicated the missing of parting limit for low melting point alloy, In-Sn. Due to the fact that both current decay follows a $t^{-1/2}$ power law in potentiostatic delithiation and height of voltammetric peak was normalized by square root of sweep rate, $\sqrt{s}$, dealloying mechanism of $In_{0.05}Sn_{0.95}$ was attributed to solid-state mass transport controlled process. Diffusion-controlled phase transformations from γ-InSn to β-Sn was claimed to occur during dealloying of γ-InSn. Due to the dealloyed layer thickness (ξ) followed a parabolic law $\xi^2 = kt$, where constant k increased with increasing temperature and electrode potential, the dealloying of γ-InSn was also attributed to a solid state diffusion controlled process.

In recent work, Cui's group considered nano-pore evolution by alloying/dealloying cycles of Li in ZnO nano-rods, Si nano-wires and Ag nano-wires [4]. In ZnO, pore formation in the size range of 1-8 nm was attributed to a Kirkendall process caused by diffusion rate difference between Zn and O^{2-} ions in the mixture of LiZn and Li_2O. No specific mechanisms were discussed in regard to pore formation in dealloying of $Li_{4.4}Si$ and Li-Ag alloys. Pore formation of all anodes of LIB was stated to be a combination effect of volume expansion during lithiation and diffusion process of host atoms (Zn, O^{2-}, Si and Ag) during delithiation, where slow diffusion rate of the host material hindered the host atom from retuning its original structures. TEM images (Figure 5 of their Supporting Information) of de-lithiated Ag showed encased nano-voids; similar to what some researchers have observed in NPG or cycling of Pt-alloy nanoparticles [31].

Liu et al. considered pore formation on alloying/dealloying cycles of Li in Ge nanowires using in situ transmission electron microscopy (TEM) [32]. They claimed the dealloyed Ge nanowires possessed porous morphologies with interconnected ligaments, however, there were no clear images of such morphologies as shown in their continuum phase field modelling results in the TEM images. The 2D projections that they presented by TEM is not a comprehensive tool for quantitatively analyzing 3D porosity. The porosity evolution was attributed to a dealloying process by a mechanism analogous to that for NPG involving selective dealloying of Li and agglomeration of vacancies. Even though Li diffusion in Li-Ge was discussed as one crucial aspect for pore formation during delithiation, solid-state mass transport was not taken into consideration in their continuum phase field model.

Chao et al. examined the microstructural evolution of Sn and Sn-Sb anode reservoirs during lithiation/de-lithiation cycling using in situ X-ray microscopy and observed the formation of porosity and cracking of micron-size particles [33]. The image resolution was poor and the morphology after dealloying and subsequent 3 h rest period seemed to consist of isolated pores and slit-shaped pores for Sn and Sn-Sb particles, respectively. The formation of pores was attributed to vacancy condensation, through which surface energy of vacancies created by removal of Li was minimized. The evolution of pores after rest period were predicted to due to the slow recrystallization of Sn and Sn-Sb at room temperature.

Our group's recent research examined dealloying morphology evolution of Mg-Cd alloy with 10, 45 and 65 at.% Mg with selective dissolution of Mg at homologous temperatures in the range of 0.53-0.69 [34]. Bi-continuous structures were observed in dealloying of 45 and 65 at.% alloys, while negative dendrite structures were reported for dealloying the 10 at.% Mg-Cd alloy. These

non-interconnected grain oriented negative dendrite structures were attributed to diffusion limited dealloying, where both surface and bulk diffusion with dealloying were non-negligible at ambient temperature. This solid-state mass transport controlled dealloying process is an interplay of metal dissolution and solid-state mass transport, which tends to homogenize the active component concentration in the alloy during the dealloying process. In order to further understand the diffusion-limited process, Chen and Sieradzki investigated the dealloying morphology evolution of particulate Li-Sn at ambient temperature [35]. Depends on the effect of Li composition, dealloying rate and particle size, Kirkendall voids, bicontinuous porous and sinusoidal rough surface morphologies were observed. No parting limit and critical potential were reported since dealloy never ceased below certain Li composition of alloy or any dealloying potential. Bicontinuous porosity formed from percolation dissolution were associated to voltammetric peak at potential ~ 450 mV of linear sweep voltammetry.

No clear and complete observation of morphology evolution of dealloying with significant solid-state mass transport has ever been reported. In order to address this issue, dealloying morphology evolution mechanism of alloy systems at low T_H, where solid-state mass transport at ambient temperature is non-negligible for dealloying process, is the focus of the work discussed here.

1.4 Importance And Objectives For Dealloying Morphology Evolution Of Li-Sn And Li-Pb Systems

The objective of my Ph.D. study is to examine the morphology evolution of dealloying with significant solid-state mass transport by addressing the following questions:

- Under what experimental conditions will percolation dissolution dominate the dealloying mechanism and generate bi-continuous porous morphology?

- Under what experimental conditions (dealloying rate, alloy composition, etc.) will solid-state mass transport controlled dealloying occur and what forms will the resulting dealloyed morphologies take?

In order to answer these two questions, suitable alloy systems need to be identified and then characterized by focus-ion beam (FIB) milling and scanning electron microscopy (SEM). We were interested in identifying alloys sytems for this study that fulfill two requirements: 1, suitable solid-state mobility of the active component at ambient temperature; and 2, the alloy composition should be easily variable by a process such as electrochemical alloying. Based on these requirements, Li alloys were chosen for the high room temperature chemical diffusivity of Li ($\overline{D}_{Li}^{Sn}$~10^{-12}cm^2/s when x(Li)~4.4 @T=25 ˚C), with which alloying and dealloying process could be done at room temperature over reasonable times. In this work, Li-Sn and Li-Pb alloys were chosen since they have a rich history, with abundant thermodynamics, kinetic and structural data available. Additionally, since these alloys can be fabricated at ambient temperature by electrochemical processing it is relatively straightforward to access a range of alloy compositions necessary to examine morphology evolution (Fig. 1.3). A significant difference between the more-studied noble metal alloys and Li-Sn and Li-Pb alloys is also in the nature of the equilibrium phase diagrams. Li-Sn and Li-Pb displays multiple stoichiometric intermetallic phases not all of which are accessible at ambient temperature (as summarized in chapter 1.4). What's more, as shown in Table 1.1, Sn is often considered to be an attractive candidate LIB anode reservoir due to its high specific capacity (993 mAh/g for $Li_{22}Sn_5$), cascading voltage profile, safety, wide and availability [36]–[39]. Although Sn offers a specific capacity more twice that of graphite, it suffers large irreversible capacity losses during the first few charge-discharge cycles. One contributing factor is the large volume expansion and shrinkage of Sn

during lithiation-delithiation cycles causing among other things electric contact loss and fracture. An important step in understanding and controlling the large irreversible capacity loss is to study the morphology evolution of dealloying.

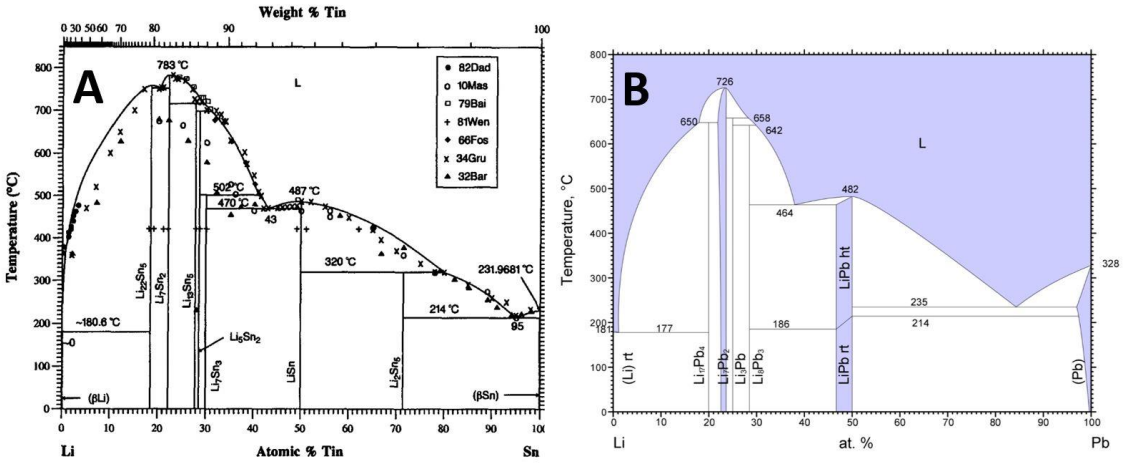

Figure 1.3. Phase diagrams. **A**. Li-Sn [40]. **B**. Li-Pb [41].

Table 1.1. Comparison of LIB related properties of Sn, Pb and graphite, the commercially used anode of LIB.

Materials	Graphite (LiC_6)	Sn ($Li_{4.4}Sn$)	Pb ($Li_{4.4}Pb$)
Theoretical specific capacity (mAh g^{-1})	372[42]	993.4	569.1
Theoretical charge density (mAh cm^{-3})	837[42]	7238.9	4654.1
Volume change (%)	9.35[43]	676.31[43]	233.66[43]
Crystal structure	-	tetragonal	FCC

As shown in Table 1.1, similar to Sn, Pb also has a larger specific capacity than graphite and has a different crystal structure than Sn. Plus, the crystal structures of Li_xPb and Li_xSn phases have huge differences as shown in Tables 1.2 and 1.3. Thus, by comparing Li-Sn and Li-Pb systems, the effect of crystal structure on dealloying morphology evolution could be investigated.

1.5 Reviews On Relationship Between Electrode Potential And Li Composition Of Li-Sn And Li-Pb

During electrochemical Li-Sn and Li-Pb alloy synthesis, the alloy composition are controlled by the lithiation potential. Typically, the relation between working electrode potential and Li concentration is obtained according to the plot of the quasi-equilibrium potential versus alloy composition, which could be calculated by the charge consumed during lithiation from titration measurements and corresponding X-ray diffraction data. For the alloys examined in our study there is more than sufficient existing data in this regard.

During the electrochemical lithiation of the M electrode, where M stands for Sn or Pb, there are two components (Li and M) and either one or two phases (Li_xM) can form at a particular potential. At fixed temperature and pressure, the Gibb's phase rule can be written as $f = C-P$ where f is the degrees of freedom of the intensive variables, C is the number of components and P is the number of phases present. In a two-component system at fixed temperature and pressure the only degree of freedom available is the mole fraction (or chemical potential) of the components. When a single phase is present, there is one degree of freedom and the electrochemical potential of the components will depend on composition. When two phases are present, the electrochemical potential of each component in each phase must be equal so that in this two-phase co-existence region the electrochemical potential is fixed. The only thing that changes within a two-phase region is the volume fraction of each of the phases as Li is alloys or dealloyed. Thus, the voltage profile of M lithiation is consisted of a series of two-phase plateaus separated by single-phase regions as shown in Fig. 1.4 [44]. From a thermodynamic point of view, all equilibrium phases shown in the Li-M phase diagram should be observed in voltage profiles obtained through room temperature electrochemical reactions at corresponding Li concentration if near-equilibrium conditions are maintained. Thus, phases at the slope-non-zero

single phase regions could be assigned based on x abscissa of Fig. 1.4. Therefore, Li_xM alloy phases with known Li concentration could be manufactured by potentiostatic lithiation based on the equilibrium potential of different Li_xM single phases.

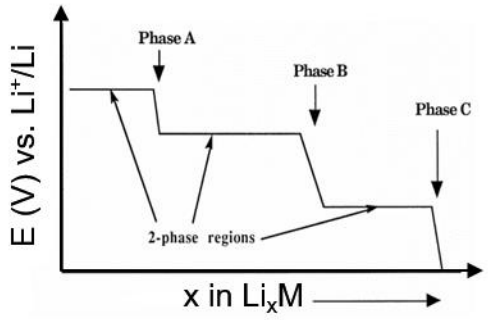

Figure 1.4. Schematic representation of titration curve of Li-M with three intermediate phases under equilibrium conditions [44].

1.5.1 Review Of Voltage-Profiles For Li-Sn And Li-Pb

Voltage profiles as shown in Fig. 1.4 can be obtained experimentally either at near equilibrium or non-equilibrium conditions. As shown in Fig. 1.5 A, Huggins [44] reported a voltage profile for the Li-Sn system obtained using a coulometric titration technique with cells of the type $Li_ySn|1\ M\ LiAsF_6\text{-}PC|Li_xSn$. After passing a known amount of charge through the cell, the equilibrium potential was recorded as the time independent open circuit potential reflecting the equality of chemical potentials of Li in the alloy and Li ions in the electrolyte. According to the Li concentration, which was calculated from the charge consumed during coulometric titration, sharp drops in potential were assigned to single phase regions of Li-Sn. Except for Li_5Sn_2, which was only observed in coulometric titration curved obtained at 400 ˚C, all six intermetallic phases shown in Li-Sn phase diagram at room temperature were observed, as summarized in Table 1.2. The plateau potential for formation of Li_2Sn_5, LiSn, Li_7Sn_3, $Li_{13}Sn_5$, Li_7Sn_2, and $Li_{22}Sn_5$, was

reported be at 0.76 V, 0.66 V, 0.53 V, 0.49 V, 0.42 V and 0.38 V vs. Li^+/Li, respectively. Besides the equilibrium potential observed at near equilibrium condition, Huggins also showed voltage profiles obtained from galvanostatic lithiation at current densities of 0.24 $mAcm^{-2}$ and 0.5 $mAcm^{-2}$ (figure 3 in Huggins paper [45]). Under this non-equilibrium condition, the plateau at voltage ~ 420 mV vs. Li^+/Li was associated to the formation of Li_7Sn_3, which was in good agreement with others galvanostatic lithiation results shown in Table 1.2. The deviation in plateau voltage obtained from galvanostatic lithiation and coulometric titration was caused by deviation from equilibrium condition and increased with increasing current density/dealloying rate.

Table 1.2. Plateau potentials of several Li_xSn_y phases obtained by electrochemical titration at 25 ˚C. References (Refs.), where the data are taken from, are cited in the bottom row.

Li_xSn_y	Plateau potential for formation at 25 ˚C (V vs. Li^+/Li)		
Li_2Sn_5	0.76	0.68	0.70
LiSn	0.66	0.57	0.59
Li_7Sn_3	0.53	0.40*	0.45*
$Li_{13}Sn_5$	0.49	0.40*	0.45*
Li_7Sn_2	0.42	0.40*	0.45*
$Li_{22}Sn_5$	0.38	0.40*	0.45*
Refs.	[44]	[46]	[47]

Different results from those reported by Huggins have been reported by other researchers for conditions that likely were further from equilibrium. These results generally show only three plateaus (Fig. 1.5). At a charging current density of 25 μA cm^{-2} for electroplated Sn, Winter [47] associated the plateaus at 0.7 V and 0.59 V vs. Li^+/Li to the formation of Li_2Sn_5 and LiSn, respectively. Similarly, for Sn powder electrodes at current density of 37.2 mA g^{-1}, Dahn [46] reported plateau potential for formation of Li_2Sn_5 and LiSn to be 0.68 V and 0.57 V vs. Li^+/Li, respectively. As shown in Fig. 1.5 C, an interesting point of Dahn's voltage profile is that charge

consumed from galvanostatic lithiation and delithiation were exactly the same, which had never been seen in other researcher's results in chronopotentiometry. Even in another of Dahn's reported voltage profiles (figure 2a in [48]) of Sn powder electrodes with the same cell configuration and current density, huge capacity loss was seen in lithiation-delithiation cycles. Both results showed a single-phase behavior at high Li concentration, Li_xSn ($x > 2.33$) at voltages less than ~ 0.4 V vs. Li^+/Li. It is hard to decide which Li-rich Li_xSn ($x > 2.33$) phase exists in what potential range from the voltage profile data only. Thus, phase evolution during galvanostatic lithiation studied using computational and experimental characterization methods are reviewed in the next chapter.

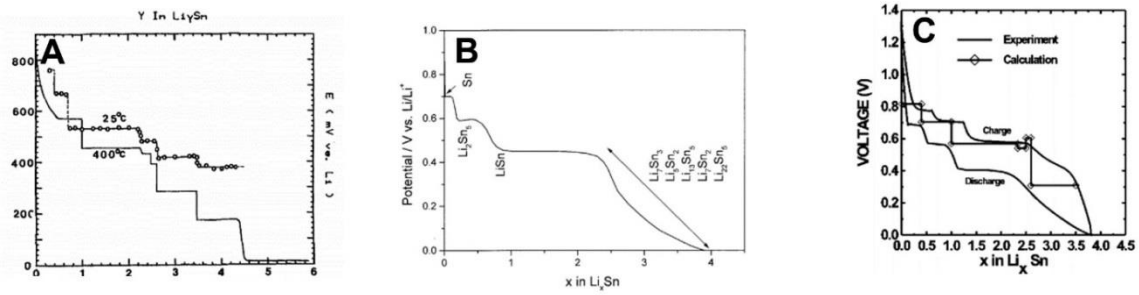

Figure 1.5. Voltage profile of Li-Sn system. A. Equilibrium potential as a function of Li composition by coulometric titration at 25 ˚C (dashed line with hollow circle indicating data points) and 400 ˚C (solid line) [44]. **B**. Charge curve for electroplated Sn in 1 M $LiClO_4$-PC by galvanostatic lithiation at current density of 25 μA cm^{-2} [47]. **C**. Experimental and calculated electrochemical voltage profiles for Sn powder in 1 M LiPF6-3:7 (v/v) mixture of ethylene carbonate and diethyl carbonate by galvanostatic lithiation at current density of 37.2 mA g^{-1} [46].

The voltage profile of Li-Pb from coulometric titration in 1 M $LiAsF_6$-PC at 25 ˚C was reported by Huggins [49]. Similar to their work on Li-Sn [44], the time independent open circuit potential was measured after intermittent pulses of constant current through a three electrode cell with Li foils as counter and reference electrodes. Four Li_xPb intermediate alloy phases were assigned to sharp potential drop shown in the coulometric titration curves (Fig. 1.6 A). The plateau potentials

for formation of LiPb, Li_3Pb, $Li_{3.2}Pb$ and $Li_{4.5}Pb$ were reported to be 0.601 V, 0.449 V, 0.374 V and 0.292 V vs. Li^+/Li, respectively [50]. However, no Li-Pb equilibrium phases were found in the phase diagram of Li-Pb at room temperature at the compositions $Li_{3.2}Pb$ and $Li_{4.5}Pb$.

Little information on voltage profile by galvanostatic lithiation of lead was ever reported. Here, the galvanostatic lithiation curve and the corresponding differential capacity plots of lead oxide based LIB anode are reviewed. Sánchez [51] analyzed Li_xPb phase formation potential of spray pyrolized Pb (II) oxide using galvanostatic cycling and PITT. Two capacitance peaks at potentials of 0.53 and 0.38 V vs. Li^+/Li in differential capacity plot from galvanostatic cycling at current density of 0.25 mA cm^{-2} were associated to formation of $Li_{2.5\text{-}3}Pb$ and $Li_{3.2}Pb$, while another two peak at 0.18 V and 0.05 V vs. Li^+/Li were corresponded to Li-rich Li_xPb phases (x = 3.5, 4 or 4.5). Sánchez [52] also conducted galvanostatic lithiation of Pb-based materials with PbO_2, PbO and Pb as main phases and summarized the lead alloy existence potential. The existence potentials of LiPb, $Li_{2.6}Pb$, $Li_{3.5}Pb$ and $Li_{4.4}Pb$ in lithiation direction were reported to be 0.53 V, 0.3-0.26 V, 0.12 V and 0.05 V vs. Li^+/Li. Pan [53] reported voltage profile for galvanostatic lithiation at current density of 0.3 mA cm^{-2} and cyclic voltammetry (CV) curves at sweep rate of 0.5 mV s^{-1} of PbO@C. The cathodic peak in CV were attributed to formation of different Li_xPb ($1 < x < 4.4$) alloys. Two plateaus were shown in voltage profiles at potentials of 0.53 V and 0.35 V vs. Li^+/Li. However, no specific phase formation information was discussed.

1.5.2 Review Of Voltage-Profile Of Li-Sn And Characterization Methods (XRD/AFM/Ab Initio Calculation)

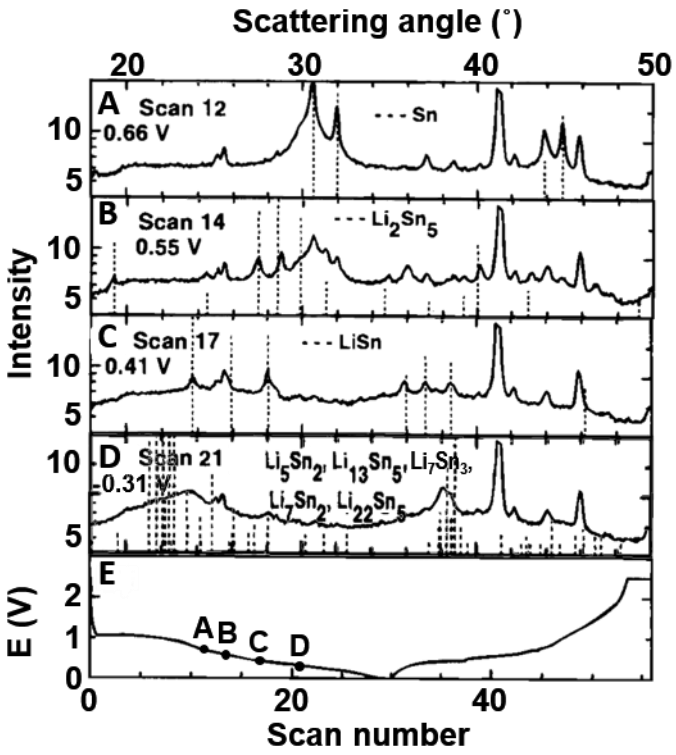

Figure 1.6. In situ XRD results and voltage profile for lithiation of SnO at different XRD scan numbers and electrode potentials selected from reference [48]. **A-D**. XRD spectrum of SnO electrode with logarithmic intensities versus scattering angle with calculated patterns corresponding to indicated Li_xSn phases in dashed lines. **B**. voltage profile (scan number vs. voltage) for current galvanostatically cycled at current density of 9.3 mA g^{-1} with dots labelled as A-D indicating lithiation stage corresponding to XRD data shown in **A-D**.

Dahn [48] studied the crystalline phase evolution in lithiation of tin oxide, SnO, using in situ X-ray diffraction. SnO powder electrodes in the situ XRD cell were galvanostatically cycled at current density of 9.3 mA g^{-1} in a voltage range between 0 V and 2.5 V vs. Li^+/Li. The SnO electrode was consecutively scanned employing a Cu K_α source. It was shown that SnO was reduced to pure Sn when electrode potential dropped from open circuit potential of SnO to 0.94 V vs. Li^+/Li. Selected XRD spectra for SnO lithiation after Sn formation was summarized in Fig.

1.6. As shown in Fig. 1.6 B, broad Sn peaks shown in Fig. 1.6 A declined with the emergence of Li_2Sn_5 peaks, which proved the formation of Li_2Sn_5 between 0.66 V and 0.55 V. At 0.41 V (Fig. 1.6 C), Li_2Sn_5 peaks disappeared and LiSn peaks as shown in broken lines presented. When electrode potential reached 0.31 V vs. Li^+/Li, broad peaks associated to formation of mixture of all Li-rich Li_xSn phases ($x > 2.33$) was shown in Fig. 1.6 D. No obvious plateau was shown in voltage profile in Fig. 1.6 E, but the correlation between phase existence and electrode potential are summarized in Fig. 1.7.

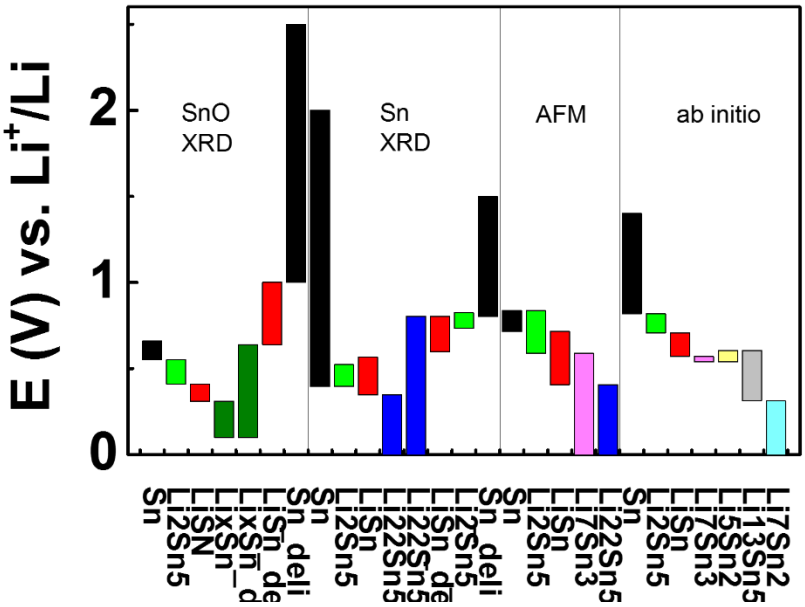

Figure 1.7. Summary of voltage profiles obtained by XRD of SnO [48] and Sn [54], AFM [55], and ab initio calculation [46]. Voltage ranges corresponds to different Li_xSn phases represented as different colored columns: black, Sn; light green Li_2Sn_5; red, LiSn; dark green Li_xSn ($x > 2.33$); pink, Li_7Sn_3, yellow, Li_5Sn_2, grey, $Li_{13}Sn_5$; cyan, Li_7Sn_2; dark blue, $Li_{22}Sn_4$.

Dahn [46] also conducted *ab initio* calculations using a pseudopotential plane-wave method to derive a theoretical electrochemical voltage profile for the Li-Sn system. Lattice constants, crystal structures and lattice site coordinates of Li-Sn phases (Sn, Li_2Sn_5, LiSn, Li_7Sn_3, Li_5Sn_2, $Li_{13}Sn_5$, Li_7Sn_2 and Li) were used to calculate their total internal energy. Voltage drops (V)

between potential plateaus were derived by their internal energy (E) from $V = -(E(Li_{x+\Delta x}Sn) - E(Li_xSn) - \Delta x E(Li))/nF$, where Δx refers to the number of lithium atoms transferred in the reaction between Li_xSn and $Li_{x+\Delta x}Sn$. As shown in Fig. 1.5 C, the ab-initio calculation resulted voltage profile predicted six voltage plateaus corresponding to phase transformation reaction involving six Li_xSn phases. Comparison between experimental and calculation results depicts that the single-phase like voltage changing region between potential of 0.405 V and 0 V vs. Li^+/Li in the experimental discharge curve are related to phase transformation between Li-rich Li_xSn ($x > 2.33$) phases. Notice that the formation of Li_5Sn_2 was also predicted by ab-initio calculation at room temperature, even though no experimental results had ever proved existence of Li_5Sn_2 in electrochemical lithiation of Sn at room temperature.

Rhodes [54] conducted in situ XRD measurements on sputtered Sn thin film with thickness of 5 μm lithiated and then delithiated at constant current density of 230 μA cm^{-2}. Two plateaus at potential of 0.56 V and 0.38 V vs. Li^+/Li were related to the phase transformation between Li_2Sn_5 and LiSn and LiSn and $Li_{22}Sn_5$, respectively. Close inspection of lithiation voltage profile (figure 5 in [54]) shows a slope change of electrode potential versus lithiation duration at potential ~ 0.6 V vs. Li^+/Li. This slope change region shows up at the same potential range of single-phase Li_2Sn_5 as predicted by other researchers. The existence of Li_2Sn_5 was also detected from XRD at potential ~ 0.6 V vs. Li^+/Li. Also, Rhodes pointed out that the lower overall peak intensity at about 9 – 27.5 h might indicate existence of amorphous Li_7Sn_3.

Dahn [55] investigated the effect of electrochemical reaction of Li and Sn on Sn tower height by in situ AFM and reported relationship between volume increase percentage and Li-Sn phases. Sn towers with dimension of 7.5 μm x 7.5 μm x 0.3~0.5 μm (length x width x height) sputtered on

Cu foil were electrochemically cycled at current density of 38 μA cm^{-2} versus a Li metal counter in the electrolyte of 1 M $LiPF_6$-EC/PC (mixture of ethylene carbonate and propylene carbonate in 50/50 volume ratio). The relationship between volume changing, potential evolution and lithiation duration of Sn towers was reported in figure 11 of [55]. The phase transformation reaction plateaus determined by volume increase percentage were larger than those determined by electrochemical methods by ~ 200 mV. Plus, one plateau at ~ 600 mV vs. Li^+/Li was indicated as a single-phase region of LiSn, which did not seem to be reasonable.

Voltage profiles obtained from non-electrochemical methods were compared in Fig. 1.7. SnO XRD data were extracted from figure 4-11 of Dahn's work [48]; Sn XRD data were taken from figure 3 and 4 of Rhodes's paper [54]; voltage profile from AFM was replotted from figure 11 of Dahn's work [55]; ab initio calculation data were drawn from figure 1 of Dahn's paper [46]. Existence voltage range of Sn, Li_2Sn_5 and LiSn phase obtained from XRD characterization of SnO and Sn powder cells was in good agreement. Li-rich Li_xSn ($x > 2.33$) phases were detected in almost same voltage ranges from ~ 0.3 V to 0 V in lithiation direction and from 0 V to ~ 0.6 V in delithiation direction. According to the crystal structure study of $Li_{22}Sn_5$ conducted by Dahn [56], narrow strong peak of electrochemical synthesized $Li_{22}Sn_5$ could not be observed in XRD spectrum since the Li-rich Li_xSn ($x > 2.33$) phase formed electrochemically are all based on BCC lattice with randomly positioned groups of tin tetrahedral, which leads to broad oscillations around 22˚ and 38˚. The phase transformation reactions obtained from in situ AFM methods follows the same trend of phase evolution as those in XRD results. However, the phase existence regions seemed not to be well related to voltage plateaus obtained from electrochemical lithiation curves. The phase existence voltage seemed to be higher in ab initio calculation, which is reasonable for ab initio assumed the system was lithiated at equilibrium condition. Thus, the

deviation of real life time scale from infinite long equilibrium time scale caused lower phase existence potentials as predicted in XRD and AFM characterization methods.

1.5.3 Crystallographic Information For Li-Sn And Li-Pb Intermetallic Compounds

An important step in understanding and interpretation of XRD spectrum of electrochemically synthesized Li_xSn phases is to know the crystal structure information of all possible Li_xSn phases stable at room temperature. The difficulty with using Sn and Pb as anode of lithium-ion battery lies in a two to threefold volume change associated with alloying of lithium. This huge volume expansion can cause cracking and crumbling of the metal anode. Volume expansion during lithiation are related to theoretical volume change for crystalline Li-Sn alloy phases, which is determined by crystal structures and lattice parameters of Li-Sn phases. There are lots of crystal structure information published on Li-Sn and Li-Pb systems. The crystal information of Li-Sn and Li-Pb is summarized in Table 1.3, Table 1.4, Fig. 1.8 and Fig. 1.9.

Table 1.3. Crystal structure information for room temperature equilibrium Li_xSn alloys.

phase	Space group	Lattice constants (Å)	Volume per mol Sn (cm^3/mol)
Sn	-	-	16.18*
Li_2Sn_5	P4/mbm	a= 10.274, c = 3.125 [57]	19.88*
LiSn	P2/m	a = 51.7, b = 7.74, c = 3.18, γ = 104.5˚ [58]	24.74*
Li_7Sn_3	$P2_1/m$	a = 9.45, b = 8.56, c = 4.72, γ = 105.95˚ [59]	36.95*
Li_5Sn_2	$R\bar{3}m$	a= 4.74, c = 19.83 [60]	44.64*
$Li_{13}Sn_5$	$P\bar{3}m1$	a= 4.70, c = 17.12 [61]	45.45*
Li_7Sn_2	Cmmm	a = 9.80, b = 13.80, c = 4.75 [62]	48.31*
$Li_{22}Sn_5$	F23	19.660 [40]	58.14*

*the volume per mol Sn data were extracted from Dahn's work [48].

Table 1.4. Crystal structure information for room temperature equilibrium Li_xPb phases.

phase	Cell type	Space group	Lattice constants (Å)
Pb	cubic	Fm3m	a = 4.950, α = 89.5 ˚ [63]
β'-LiPb	cubic	Pm3m	a = 3.563 (220 ˚) [64]
Li_8Pb_3	monoclinic	C2/m	a = 8.24, b = 4.757, c = 11.03, γ = 104.5˚ [65]
Li_3Pb	cubic	Fm3m	a = 6.687 [66]
Li_7Pb_2	hexagonal	P321	a = 4.751, c = 8.589 [66]
$Li_{17}Pb_4$	cubic	F$\bar{4}$3m	a = 19.842 [67]
Li	cubic	Im3m	a = 3.508 [68]

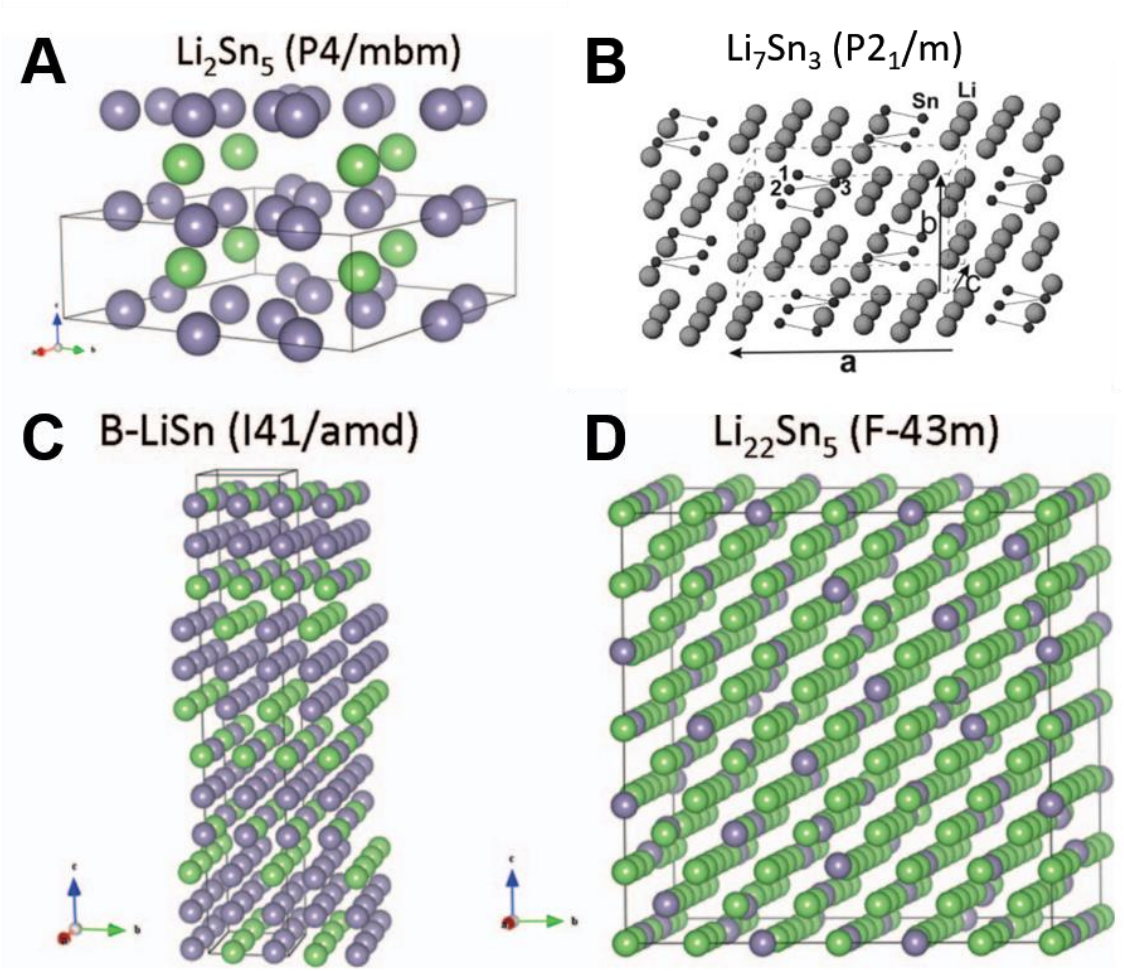

Figure 1.8. Crystal structures of Li_2Sn_5, Li_7Sn_3, LiSn and $Li_{22}Sn_5$. Sn and Li atoms are represented in gray and green, respectively, with superimposed prism representing the unit cell of each plane [54]. **B**. Li atoms are represented by the larger spheres while Sn atoms are represented by the smaller spheres. Dashed line represents the unit cell of Li_7Sn_3 [69].

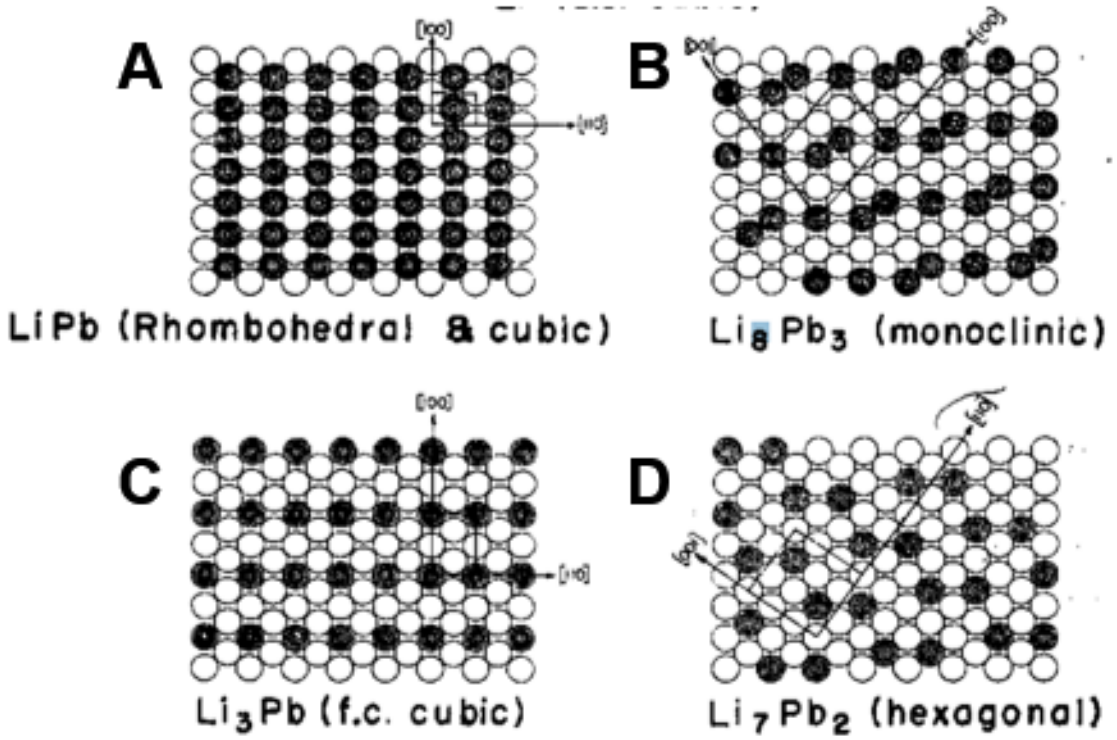

Figure 1.9. Crystal structures of Li-Pb phases. A. LiPb, **B.** Li_8Pb_3, **C.** Li_3Pb, **D.** Li_7Pb_2. Pb and Li atoms are represented in black and white balls, respectively [70].

As shown in Fig. 1.8, Sn-rich Li-Sn alloy phases, Li_2Sn_5 and LiSn have a crystal structure similar to that of β-Sn (tetragonal). While, as shown in Table 1.3, Li-rich Li-Sn alloy phases, Li_5Sn_2, $Li_{13}Sn_5$, Li_7Sn_2, and $Li_{22}Sn_5$ all possess a BCC based unit cell (Li is BCC) and only differ in the arrangement of Li and Sn on the lattice sites. The similarity in crystal structures of Li-rich Li-Sn alloys makes it harder to distinguish one from another in XRD spectrum. The molar volume based on the molar quantity of Sn depicts large volume dilation ~ 3.6 relative to Sn.

1.6 Diffusion Measurements

In order to quantitatively understand the role of solid-state mass transport in morphology evolution of dealloying, the intrinsic diffusion coefficient of Li in Li metal alloys has to be measured. The galvanostatic intermittent titration technique (GITT) and potentiostatic

intermittent titration technique (PITT) are two electrochemical methods, which combine transient and steady-state measurements to determine the chemical diffusion coefficient, $\overline{D}$. These two techniques were introduced by Wepper, Huggins and co-workers [71],[72].

The GITT and PITT are established based on several assumptions: first, the volume expansion/shrinkage of the Li metal alloy system during discharging/charging process is negligible; second, the rate-limiting step is solid-state diffusion; third, the system is isothermal and isobaric; fourth, the solid-state diffusion corresponds to one-dimensional transport and obeys Fick's second law of diffusion (Eq. 2); fifth, the interface between Sn and Cu (serving as the current collector) is impermeable to Li [72].

Another time of flight technique based on the Devanathan Stachurski cell was also used to determine the intrinsic diffusion coefficient of Li in Li-Sn alloys. Here this technique is abbreviated as DS measurement. This technique was first introduced by Devanathan and Stachurski to measure hydrogen permeation in palladium [73]. According to the anodic current response of DS measurement, the diffusion coefficient can be calculated from the lag time, rise time, breakthrough time, and decay time constant based on the what electrochemical inlet and outlet condition is applied to the diffuser.

1.6.1 Principle Of GITT, PITT And DS Measurements

Galvanostatic method—GITT includes transient constant current steps and open circuit potential measurements between current steps. The composition of the working electrode is displaced from $Li_{\delta}Sn$ to $Li_{\delta+\Delta\delta}Sn$ by the imposition of a constant current, I, for a time interval, τ. Meanwhile, the transient voltage, E_t, is measured as a function of time, t. When measuring the open circuit potential, the time dependent transient voltage is measured until a steady-state is

achieved. This final stable potential is recorded as the steady-state equilibrium voltage, E_s, defining the alloy composition at the alloy/electrolyte interface. The schematic diagram of applied current and recorded voltage for the first two discharging GITT cycle of the working electrode is shown in Fig. 1. 10 A.

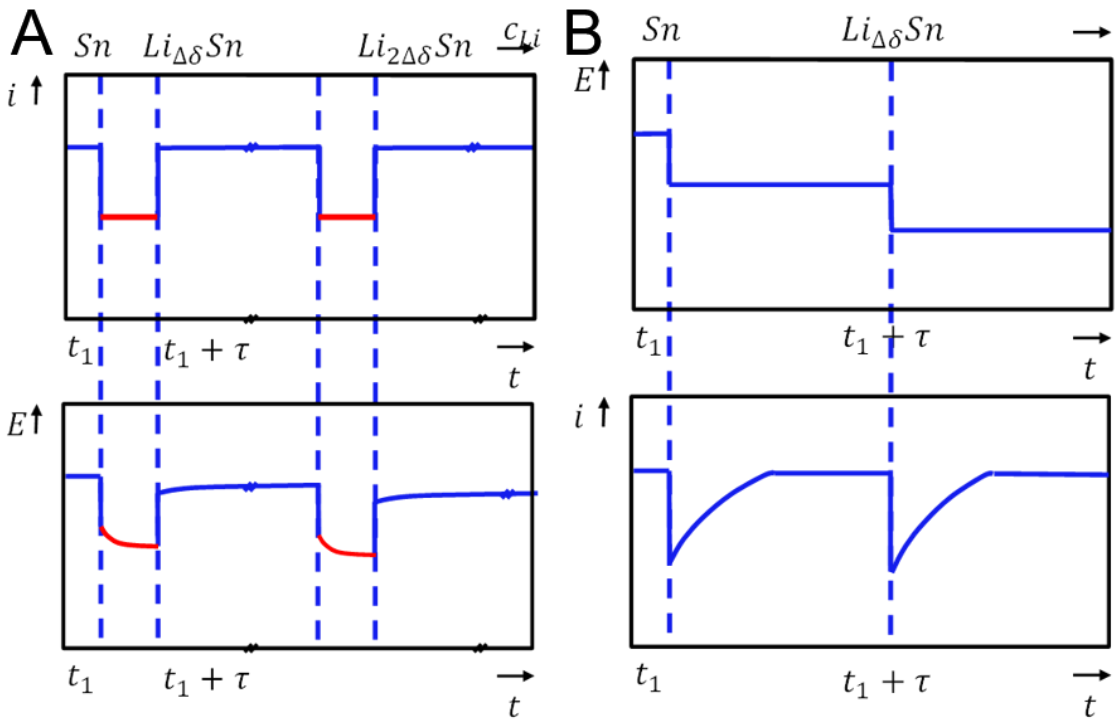

6

Figure 1.10. Schematic diagram of first two discharging cycles. A. GITT. **B.** PITT.

For each current-on period, the stoichiometric change of Li, $\Delta\delta$, during the time interval, τ, is $\frac{I\tau M_M}{Z_{Li}Fm_M}$ (derivation shown in eq. 1), where M_M is the molar mass of M, Z_{Li} is the number of charge carried by Li^+, F is the Faraday constant, and m_M is the mass of M on the working electrode.

$$\Delta\delta = \frac{\Delta n_{Li}}{n_{Sn}} = \frac{\frac{I\tau}{z_{Li}F}}{\left(\frac{m_M}{M_M}\right)} = \frac{I\tau M_M}{Z_{Li}Fm_M} = \frac{I\tau M_M}{Z_{Li}F\rho_M A_M th_M} \quad (1)$$

Here Δn_{Li} is the molar change of Li in each current-on period, n_M, ρ_M, A_M, and th_M is the molar quantity, density, active area and thickness of the M electrode.

The current pulse causes a constant flux of Li across the electrode-electrolyte interface. The Li diffusion process is described by Fick's second law of diffusion (Eq. 2).

$$\frac{\partial C_{Li}(x,t)}{\partial t} = -\overline{D}\frac{\partial^2 C_{Li}(x,t)}{\partial x^2} \quad (2)$$

Here C_{Li} is the local concentration of Li, x is the distance in to the solid from the electrolyte/electrode interface, and $\overline{D}$ is the concentration independent chemical diffusion coefficient. Note that, $\overline{D}$ is assumed to be compositional independent during each small step of GITT and PITT measurements for only small amount of charge is being accumulated and the compositional change is reasonably small during each galvanostatic/potentiostatic step.

The initial and boundary conditions for GITT are

$$C_{Li} = C_o \quad 0 \le x \le L, t = 0 \quad (3)$$

$$-\overline{D}\frac{\partial C_{Li}}{\partial x} = I/(Z_{Li}FA_M) \;\; x = 0, t > 0 \quad (4)$$

$$\frac{\partial C_{Li}}{\partial x} = 0 \;\; x = L, t \ge 0 \quad (5)$$

Here C_o is the original Li concentration in the bulk working electrode before each current-on period, $C_s = C_{Li}(x = 0, t)$ is the Li concentration at the electrode/electrolyte interface. Equation

4 means that the Li movement (flux) is controlled by the current flux. Equation 5 means that the interface between Cu current collector and M layer is impermeable to Li.

With these initial and boundary conditions, the solution of Fick's second law gives a relationship between $\overline{D}$, E_s and E_t in the short-time approximation, $t \ll \frac{L^2}{\tilde{D}}$, as shown below

$$\overline{D} = \frac{4}{\pi}\left(\frac{IV_M}{Z_{Li}FA_M}\right)^2 \left[\left(\frac{dE_s}{d\delta}\right) / \left(\frac{dE_t}{d\sqrt{t}}\right)\right]^2 \quad (6)$$

Here V_M is molar volume of M.

Thus, the chemical diffusion coefficient $\overline{D}$ of Li in M could be calculated from experiment measurable data. $\frac{dE_s}{d\delta}$ is the slope of steady-state cell potential vs. stoichiometric change of $Li_\delta M$. $\frac{dE_t}{d\sqrt{t}}$ is the slope of transient cell potential vs. $\sqrt{t}$ for each current-on period.

Potentiostatic method—PITT involves constant voltage steps across the cell voltage. Assuming that the working electrode has a uniform concentration of Li , $C_{Li,o}$, throughout the M layer before each voltage step. During each step at voltage of E, the concentration of Li at the electrode/electrolyte interface is displaced from $C_{Li,o}(x = 0, t = 0)$ to $C_{Li,s}(x = 0, t > 0)$ till the current change is comparably low ($\frac{dI}{dt}$ < set value) for a time interval, τ. Whenever the voltage is on, there exists a concentration gradient in the LiM alloy between $C_{Li,o}(x = 0, t = 0)$ and $C_{Li,bulk}(x, t)$. Chemical diffusion of Li will occur until the bulk Li concentration is the same as the surface Li concentration, $C_{Li}(x = 0, t) = C_{Li,bulk}(x, t)$. Thus, the chemical diffusion coefficient, $\overline{D}$, is related to the transient current measured during the voltage step. The schematic

diagram of applied current and recorded voltage for the first two discharging PITT steps of the working electrode is shown in Fig. 1.10.

The chemical diffusion of Li is assumed to obey Fick's 2nd Law (eq. 2). The initial and boundary conditions for PITT are

$$C_{Li} = C_o \quad 0 \le x \le L, t = 0 \tag{7}$$

$$C_{Li} = C_s \;\; x = 0, t > 0 \tag{8}$$

$$\frac{\partial C_{Li}}{\partial x} = 0 \;\; x = L, t \ge 0 \tag{9}$$

Equation 7 means the bulk Li concentration is assumed to be homogenized before the starting of each potentiostatic step; equation 8 means the Li concentration at the electrode/electrolyte interface is kept constant by controlling constant potential. Equation 9 means that the interface between Cu current collector and M layer is impermeable to Li.

The solution of Fick's 2nd Law with these initial and boundary conditions (eq. 7-9) gives the relationship between $\overline{D}$, I, ΔQ, and t as shown in eq. 10 for short time approximation and in eq. 11 for long time approximation.

$$I(t) = \frac{\Delta Q}{L}\sqrt{\frac{\overline{D}}{\pi}} \cdot \frac{1}{\sqrt{t}} \qquad t \ll L^2/\widetilde{D} \tag{10}$$

$$I(t) = \frac{2\Delta Q \overline{D}}{L^2} \exp\left(-\frac{\pi^2 \overline{D} t}{4L^2}\right) \qquad t \gg L^2/\widetilde{D} \tag{11}$$

Here, ΔQ is the accumulated charge during each potentiostatic step.

Thus, the chemical diffusion coefficient of Li could be calculated according to eq. 12 in the short time approximation ($t \ll L^2/\overline{D}$).

$$\overline{D} = \frac{\pi L^2}{\Delta Q^2}\left(\frac{dI}{d\sqrt{t}}\right)^2 \quad (12)$$

In the long time approximation ($t \gg L^2/\overline{D}$), the chemical diffusion coefficient of Li could be calculated from the slope of lnI vs. t, $d(lnI)/dt$, or the intercept of lnI vs. t, as shown in eq. 13, and eq. 14, respectively.

$$\overline{D} = -\frac{d(lnI)}{dt}\frac{4L^2}{\pi^2} \quad (13)$$

$$\overline{D} = \frac{L^2}{2\Delta Q}\exp(intercept) \quad (14)$$

DS measurement—The Devanathan–Stachurski permeation cell is an electrochemical double cell set-up first innovated to study hydrogen permeation in metals [73]. As shown in figure 1 in [73], DS cell consists of sandwiching a thin metal sheet between two independent electrochemical cells with their own sets of counter and reference electrodes. In one cell the sample is potentiostatically/galvanostatically or stepwise charged with hydrogen (entry side). As soon as the cathodic polarization is on, hydrogen atoms start to adsorb on the sample surface and absorb into the bulk membrane. In the other cell, the other side of the sample is polarized anodically so that the permeated hydrogen atom is oxidized (exit side). Direct and sensitive hydrogen permeation information can be determined by the measured anodic current response. The DS measurement is a powerful tool for investigating hydrogen permeation in metals [73]–[75] and

alloys[76]–[79]. DS measurements were also employed for direct measurement of the lithium transport rate in anode of LIBs. Kostechki [80] measured the transport rate of lithium through aluminum (Al) membranes by DS measurement using two Teflon electrochemical cell separated by an Al membrane with non-steady-state potentiostatic method. The measured diffusion coefficients for Li in Al varied between 4.1×10^{-10} cm^2s^{-1} and 1.5×10^{-9} cm^2s^{-1}, which is in good agreement with the previously reported D values. Persson [81] conducted DS measurement to investigate lithium ion diffusivity in highly oriented pyrolytic graphite (HOPG). The cathodic side was galvanostatically lithiated at current density of 25 μA cm^{-2}, while the anodic side was polarized at high anodic potential. The Li diffusion coefficient calculated by fitting calculated current response to the experimental anodic current response was 8.7×10^{-12} cm^2s^{-1} in the direction perpendicular to graphene planes and 4.4×10^{-6} cm^2s^{-1} in the direction parallel to graphene planes. The experimental results were in good agreement with lithium diffusivity calculated by kinetic Monte Carlo simulations.

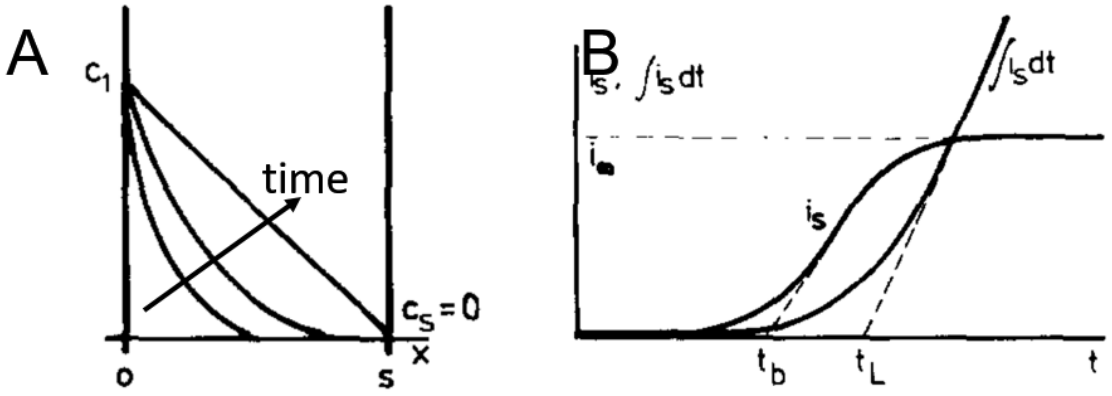

Figure 1.11. A. Li concentration gradient evolution as Li permeates through a metal membranes during DS measurement. s refers to the thickness of metal membrane. C_1 is the constant Li concentration introduced by constant voltage lithiation at entry side of Li. **B**. Theoretically anodic current response according to Fick's 2nd Law's solution of non-steady-state potentiostatic DS measurements. S-shape curve is the anodic current versus permeation time. The other curve refers to integration of current over time as a function of time. Revised from figure 3 of [82].

DS measurement can be performed following different initial and boundary conditions. Due to the simplicity of experiment, non-steady-state potentiostatic method was chosen here to investigate the diffusion coefficient of Li in Li-Sn and Li-Pb alloys. Under this condition, the cathodic side of DS cell is potentiostatically lithiated to maintain a constant Li concentration on the cathodic surface of the metal sheet; the anodic side of DS cell is delithiated at constant voltage to efficiently oxidize any Li atom reaches the exit side. The corresponding evolution of Li concentration gradient in metal membrane is schematically shown in Fig. 1.11 A [82]. The chemical diffusion of Li is assumed to obey Fick's 2nd Law (eq. 2). The initial and boundary conditions for DS measurements are

$$C_{Li} = 0 \quad 0 \le x \le L, t = 0 \tag{15}$$

$$C_{Li} = 0 \;\; x = L, t > 0 \tag{16}$$

$$C_{Li} = C_1 \;\; x = 0, t > 0 \tag{17}$$

Eq. 16 states that Li concentration is uniformly zero at time, t=0. Eq. 17 and 18 refers to the boundary conditions at exit and entry side, respectively. At exit side, all Li atoms were immediately oxidized to Li cation and dissolved into electrolyte. At entry side, Li concentration is kept constant at a certain concentration, C_1.

A solution satisfying the initial and boundary condition is [82]:

$$C_{x,t} = C_1 - C_1\frac{x}{L} + \frac{2}{\pi}\sum_{1}^{\infty}\frac{-C_1}{n}\sin\frac{n\pi x}{L}\exp(-\frac{\bar{D}n^2\pi^2 t}{L^2}) \tag{18}$$

Eq. 19 corresponds to an s-shape curve as shown in Fig. 1.11 B. The diffusion coefficient of Li can be calculated from this s-shape current response in as many as five different ways [73]. Here, diffusion coefficients were derived from time lag methods. The time-lag, t_L, is the time required to obtain a steady-stat flow of Li through the metal membrane after applying the cathodic polarization on the entry side. Classically, t_L could be evaluated by the integration of the anodic current with time. As shown in Fig. 1.11 B, as Li diffuses through the membrane, the slope of integral of current increases until a stationary linear concentration gradient is established since the total quantity of hydrogen emerging from the exit side reaches a steady-state value. t_L is defined by the intercept of t-axis and the extrapolation of the integral of current straight line [83], [84]. According to Devanathan, the same value can be readily obtained by spotting the time at which the anodic current is 0.63 of its steady-state value. Devanathan evaluated the t_L obtained by both methods and found the differences was always within 2% [73]. When diffusion coefficient is determined using the t_L the diffusion constant is independent of membrane thickness and cathodic polarization potential, as shown in figure 4 in [85]. Diffusion constant could be calculated from the t_L and the thickness of the sample, L, by eq.19.

$$\overline{\mathrm{D}} = L^2/(6t_L) \qquad (19)$$

1.6.2 Reviews Of Diffusion Coefficient Measurements For Li-Sn And Li-Pb Systems

Since Li insertion or diffusion through anode is often the rate-limiting step in battery processes [81], [86], there have been a number of published studies of the ambient temperature Li diffusivity in Li-Sn alloys as shown in Table 1.5. These results vary by as much as 5 orders of magnitude.

Huggins [44], [45], [87], [88] investigated chemical diffusion coefficient of Li in Li-Sn system by both GITT and PITT measurements at ambient and elevated temperature, respectively. Chemical diffusion of Li in intermediate Li_xSn phases were studied at 415 ˚C using a three-electrode cell of the type Al, "LiAl"|LiCl-KCl(eut.)|Li_xSn by PITT measurement with voltage step of 4-8 mV [87]. Li_xAl used was a two-phase mixture of Li-Al with Li composition ~50 at.% prepared by melting Li and Sn in molybdenum (Mo) crucible. The molten salt LiCl and KCl was mixed at their eutectic composition. By analyzing the PITT data using eq. 15, diffusion coefficient of intermediate LiSn phases existed at 415 ˚C was found to be $\sim 10^{-4} - 10^{-6}$ cm^2s^{-1} as summarized in Table 1.5. Li diffusion coefficients of Li-Sn intermediate phases at ambient temperature were studied by GITT measurements [44], [45], [88]. Ambient temperature GITT measurements were conducted with a three-electrode cell configuration of the type (-) Li|1 M LiAsF6-PC|Li_xSn (+), where Li_xSn was synthesized by melting weighted Li and Sn in Mo crucible. The GITT experiment showed chemical diffusion coefficient of LixSn was in the range of $\sim 10^{-7} - 10^{-8}$ cm^2s^{-1} as indicated in Table 1.5. The diffusion coefficient obtained by Huggins is to the order of magnitude ~ 5 larger than those obtained by other researchers.

Table 1.5. Summary of existing literature values of the intrinsic Li diffusivity, $\bar{D}_{Li}$, in Li-Sn alloys.

x in Li_xSn	$\bar{D}$ (cm^2 s^{-1})	technique	Temperature (K)	direction	cite
0.7	$6 - 8 \times 10^{-8}$	Galvanostatic*	298.15	lithiation	[45]
2.33	$3 - 5 \times 10^{-7}$	Galvanostatic*	298.15	lithiation	[45]
4.4	$1.8 - 5.9 \times 10^{-7}$	GITT	298.15	both	[88]
1	$2.24 - 4.1 \times 10^{-6}$	Potentiostatic*	688.15	lithiation	[87]
2.33-4.4	$2.57 - 75.9 \times 10^{-5}$	Potentiostatic*	688.15	lithiation	[87]
full range	$10^{-15} - 10^{-10}$	GITT	253	both	[89]
full range	$10^{-14} - 10^{-9}$	GITT	273	both	[89]
full range	$4 \times 10^{-13} - 4 \times 10^{-10}$	GITT	333	both	[89]
full range	$3 \times 10^{-16} - 6 \times 10^{-14}$	GITT	293.15	lithiation	[90]

full range	$6 \times 10^{-17} - 3 \times 10^{-13}$	GITT	-	lithiation	[91]
full range	$4 \times 10^{-18} - 4 \times 10^{-12}$	GITT	-	delithiation	[91]
< 1	$7 \times 10^{-8} - 6 \times 10^{-7}$	neutron depth profiling	-	lithiation	[92]

-Experimental temperature was not specified in original papers.
*PITT and GITT measurements performed in certain voltage ranges.

In order to get lithium diffusion coefficient in electrodeposited Sn film on Cu, Madden also performed GITT measurements at ambient temperature [91]. GITT measurements were conducted in a three-electrode pouch cell configuration with 1 μm thick Sn foil as working electrode and two pieces of Li foils as counter and reference electrodes in 1 M $LiClO_4$ in PC. In order to minimize the influence of unstable SEI layer, Sn electrode was galvanostatically activated at descending current densities from 100 μA cm^{-2} to 20 μA cm^{-2}. This activation cycles were than proved to be unnecessary in our results of Li-Sn system. According to eq. 7, the diffusion coefficients of Li in Li-Sn alloys as a function of Li composition was obtained in the range between 4×10^{-18} cm^2s^{-1} and 4×10^{-12} cm^2s^{-1}.

Pridatko [89] calculated Li diffusion coefficient as a function of Li composition for different Li_xSn phases at 253 K, 273 K and 333 K by GITT measurements for an industrially manufactured tinplate. The cell used for GITT measurement includes one piece of tinplate as working electrode, two pieces of Li foils as counter and reference electrode and electrolyte of 1 M $LiClO_4$ in PC/dimethoxyethan (7:3). Similar to what Madden [91] did, several charge-discharge galvanostatic cycles were performed before GITT measurements to form stable SEI layer. Interestingly, at certain Li composition, the Li diffusion coefficient obtained at higher temperature (333 K) was lower than that at lower temperature (273 K). The chemical diffusion coefficient was reported to be ~ $10^{-15} - 10^{-10}$ cm^2s^{-1}, $10^{-14} - 10^{-9}$ cm^2s^{-1}, and $10^{-13} - 10^{-10}$ cm^2s^{-1} at temperature of 253 K, 273 K and 333 K, respectively.

Xie [93] conducted GITT measurements of 3.2 μm thick RF magnetron sputtered Sn layer on Cu substrate at 20 ˚C. Three electrode beaker cell filled with 1 M $LiClO_4$ in a mixture of ethylene carbonate/diethyl carbonate (1:1 in volume ratio) was used as reservoir, in which sputter Sn and two pieces of Li foils were used as working, counter and reference electrode, respectively. Similar to Madden [91] and Pridatko [89], Xie also performed galvanostatic cycles before the GITT measurement. Including the large dips of diffusion coefficients in phase transformation regions, Li diffusion coefficient was in the range of 10^{-16} to 10^{-14} cm^2s^{-1}.

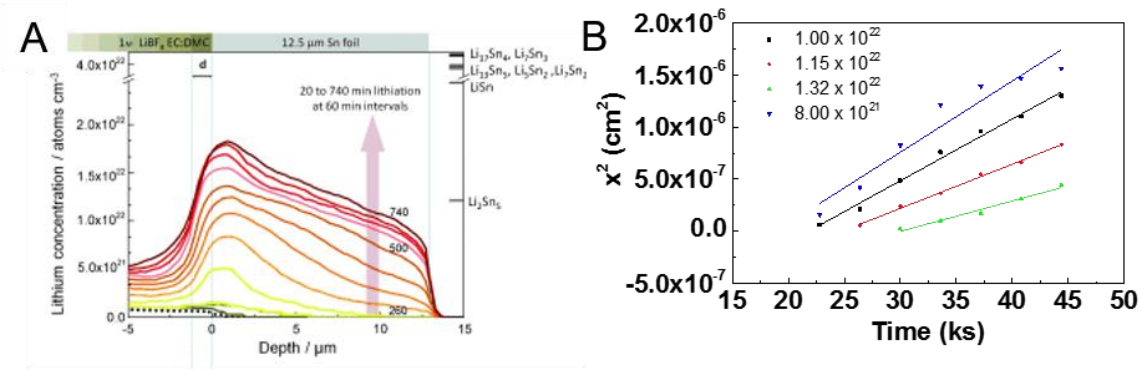

Figure 1.12. A. Lithium concentration profiles within a 12.5 μm Sn foil as a function of time detected by NDP. Dashed lines: before electrochemical lithiation. NDP spectra were plotted every 60 min interval from 20 min to 740 min at 0.4 V versus Li/Li^+. Figure 2 of Co's work [92]. **B.** Lithium penetration depth as a function of time at different Li concentrations (atom cm^{-3}) digitized from **A**. The data were linear fitted according to $x^2 \sim 2\bar{D}t$.

Table 1.6. Summarization of diffusion coefficient calculated by linear fitting of penetration depth square versus time of NDP data.

Lithium concentration (atoms cm^{-3})	$\bar{D}$ (cm^2s^{-1})	R^2
8.00×10^{21}	7×10^{-11}	0.9334
1.00×10^{22}	6×10^{-11}	0.9911
1.15×10^{22}	4×10^{-11}	0.9964
1.32×10^{22}	3×10^{-11}	0.9777

Co [92] reported lithium concentration profiles as a function of Sn layer depth by using in situ neutron depth profiling (NDP). A special designed coin cell with Kapton film window allowing

nuclear reaction products to pass through was used. 12.5 μm thick Sn foil and 300 μm thick Li foil was separated by a 25 μm Celgard separator immersed in electrolyte of 1 M $LiBF_4$-EC:DMC (1:1). As the half cell was potentiostatically lithiated and delithiated at potential of 0.4 V and 1 V vs. Li^+/Li, respectively, sequential NDP spectra were recorded in a time interval of 5 min. Fig.1.12 A, shows the lithium concentration profile obtained from NDP spectra with time interval of 60 min [92]. By plotting the penetration depth squared versus time at a fixed Li concentration, the diffusion coefficient could be estimated by fitting the plotted data points into eq. 21. As shown in Fig.1.12 B, the penetration depth square could be easily fitted to a straight line as a function of time with R^2 larger than 0.933. The Li diffusion coefficient calculated by digitizing Co's Li concentration profile was in the range of 3×10^{-11} cm^2s^{-1} and 7×10^{-11} cm^2s^{-1} as shown in Table. 1.6, which was in the same scale of diffusivity obtained from PITT and GITT measurements (except for those from Huggins).

$$x^2 \approx 2\bar{D}t \tag{20}$$

CHAPTER 2

MORPHOLOGY EVOLUTION IN LI-SN SYSTEMS

2.1 Methods

Sample preparation. Tin foils (ESPI metals, 5N purity) were cold rolled to 0.001'' (25.4 μm) and stored at room temperature for three months before the experiments described below. GITT and PITT diffusion measurements were performed on electrodeposited Sn layers. These Sn layers were electrodeposited onto Cu foils following Ivey's procedure [94]. The native oxide on the Cu foils was cleaned by dipping into concentrated sulfuric acid for 5 seconds followed by rinsing with nanopure water. This cleaning procedure was repeated 3 times prior to electrodeposition. The electroplating cell was in a standard three-electrode configuration with platinum wire as the reference and counter electrodes and Cu foil as the working electrode. The Cu foil was partially covered by Kapton tape leaving only an area of 0.25 cm^2 immersed in the electrolyte and facing the counter electrode. The electrolyte contained 0.22 mol/L stannous chloride dihydrate ($SnCl_2 \bullet H_2O$) and 0.31 mol/L tri-ammonium citrate ($HOC(CO_2NH_4)(CH_2CO_2NH_4)_2$). Sn layer with thickness around 300 nm were electrodeposited by repeating chronopentiometry and Sn layer with thickness ~2 and 7 μm were electrodeposited by chronopotentiometry. The pulsed electroplating was carried out at a constant current density of 20 mA/cm^2 for $t_{nucleation}$ = 0.3 s, then another current density at 0.1 mA/cm^2 for t_{growth} = 120 s. The number of cycles for pulse deposition is 50 cycles to control the thickness of Sn layer about 300 nm. The constant current electroplating was performed at a current density of 10 mA/cm^2 for 1200 s or 5 mA/cm^2 for 800 s to control the thickness of the Sn layer to about 7 μm and 2 μm,

respectively. Thickness of electrodeposited films was confirmed by SEM (Nova 200 NanoLabUHRFEG system) at a tilt angle of 52˚.

GITT and PITT measurements. A 3-neck round bottom flask containing 10 mL of 1 M $LiClO_4$ in polypropylene carbonate (PC) was used as the electrolyte. Li foil was used as the counter and reference electrodes. Electrodeposited 2 μm thick Sn layers on Cu foil served as the working electrode. In order to minimize the folding effect of internal stress induced by discharging volume expansion, the tin working electrode (on the Cu foil) was sealed onto a piece of mica with Kapton tape leaving an area of 0.25 cm^2 facing the counter electrode. Prior to initiating a PITT or GITT experiment, the working electrode was maintained at voltage of 1 V until the current density was below 10 $\mu A/cm^2$. Galvanostatic activation cycles in the voltage range 1 V - 50 mV were sequentially performed at current densities of 500 $\mu A/cm^2$, 250 $\mu A/cm^2$ and 100 $\mu A/cm^2$. Without galvanostatic activation cycles, the GITT procedure consisted of pulses at a current density of 250 $\mu A/cm^2$ for 50 s, followed by a relaxation period of 100 s at both ambient temperature and elevated temperature. GITT measurements conducted at elevated temperatures were performed after temperature inside the reaction reservoir is stable, which usually happened after the heating plate being on for at least half an hour. For the PITT measurements with galvanostatic activation cycles, potential steps of 10 mV were applied and the current was measured as a function of time. The potential was stepped to the next 10 mV increment either when the current reached 10 $\mu A/cm^2$ or if time exceeded 5000 s.

Devanathan-Stachurski cell experiment. As described in the original work by Devanathan and Stachurski[73], the electrochemical cell consisted of two cylindrical glass compartments sealed at the bottom by two size 12 O-ring joints, between which a Sn foil of thickness of 25.4 μm and

active area of 0.1963 cm^2 was sandwiched. The Sn foil served as shared working electrode for both compartments. Each compartment carried two pieces of Li foils serving as reference and counter electrodes. The cathodic side of the Sn foil was potentiostatically lithiated at voltage of 400 mV vs. Li^+/Li, while the anodic side of the Sn foil was maintained at a fixed voltage corresponding to the open circuit potential of Sn insuring that Li could be oxidized to Li^+. The compartments were filled with 1 M $LiClO_4$ in polypropylene carbonate.

Morphology evolution. The experiment set-up was the same as that of GITT and PITT measurements except for the working electrode here used was 25.4 μm thick Sn sheets. Potentiostatic lithiation of 25.4 μm thick Sn sheets was performed by maintaining the working electrode at prescribed potential until the current density was below 10 $\mu A/cm^2$. Galvanostatic delithiation was performed at prescribed current densities in the voltage range of 0.4-2.5 V. Linear sweep delithiation was carried out at different sweep rates at 0.087 mV/s, 0.017 mV/s and 0.0017mV/s in the voltage range from 0.4—1.5 V.

All electrochemical measurements and morphology evolution experiments were conducted inside an ultrahigh-purity argon-purged MBraun LABMaster glove box (H_2O and O_2 < 0.1 ppm) using either a Gamry series-G or BioLogic SP-150 potentiostat. All potentials mentioned in this work are referred to the Li^+/Li electrode.

Focused ion-beam milling (FIB) and SEM. After delithiation, fully delithiated Sn foils were immersed in acetonitrile for 12 h to dissolve the SEI layer and then transferred to the SEM chamber. While partially delithiated Sn foils were carefully dried with Kimi wipe and then transferred in a sealed aluminum laminated bag filled with Ar. The air exposure of partially delithiated Sn foils was less than 5 s when transferred into SEM chamber. Scanning electron

microscope (SEM) and focused ion beam (FIB) milling was conducted in a dual-beam Nova 200 NanoLabUHRFEG system at a 52˚ tilted angle.

2.2 Composition-Dependent Intrinsic Diffusion Coefficient Of Li In Li-Sn Alloy Measured By GITT

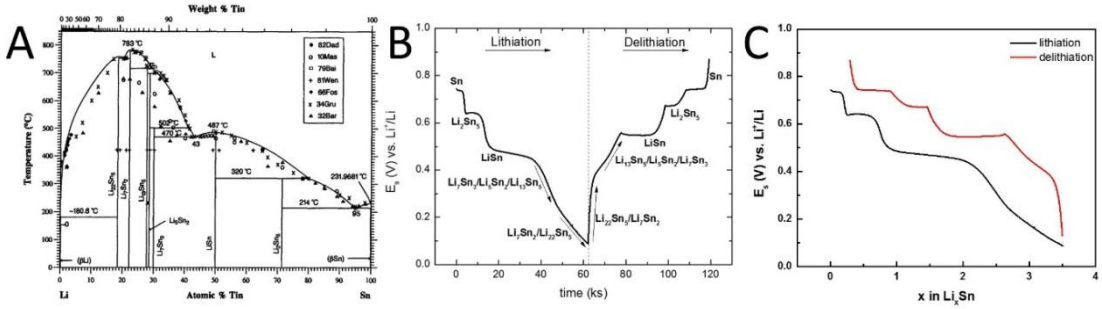

Figure 2.1. A. Li-Sn phase diagram [40]. **B**. Plot of E_s as a function of time with single phase and mixed phase transformation regions defined by voltage ranges obtained from ambient temperature GITT measurement with galvanostatic cycling. **C**. Plot of E_s as a function of Li composition obtained from GITT measurement with galvanostatic cycling.

The experimentally measured equilibrium titration curve (quasi-equilibrium potential, E_s, versus composition plot) together with phase diagrams are useful tools for understanding and presenting the relation between working electrode potential and phase(s) preexisted and evolving at the electrode surface. Even though the dynamic electrochemical delithiation in chronopotentiometry at low dealloying rate can be described as selective equilibrium, where equilibrium was only obtained in the mobile species but not in the host structure lattice [95], the voltage behavior under dynamic conditions in chronopotentiometry still deviate from equilibrium values. Different from which shown in Fig. 2.8 J, K and L, the lithiation and delithiation voltage profile shown in . 2.1 B and C shows clear differentiation between one-phase and two-phase region. Thus, as shown in Fig. 2.1, the steady-state potential as a function of composition and charging/discharging duration obtained from GITT measurements at ambient temperature with

galvanostatic cycling is used to assign single phase and phase transformation regions according to the phase diagram of Li-Sn system (Fig. 2.1 A). The assigned correlation between phases and electrode potentials was used to determine Li composition of Li-Sn alloys prepared by potentiostatic lithiation for dealloying morphology evolution characterization and in the GITT measurement results.

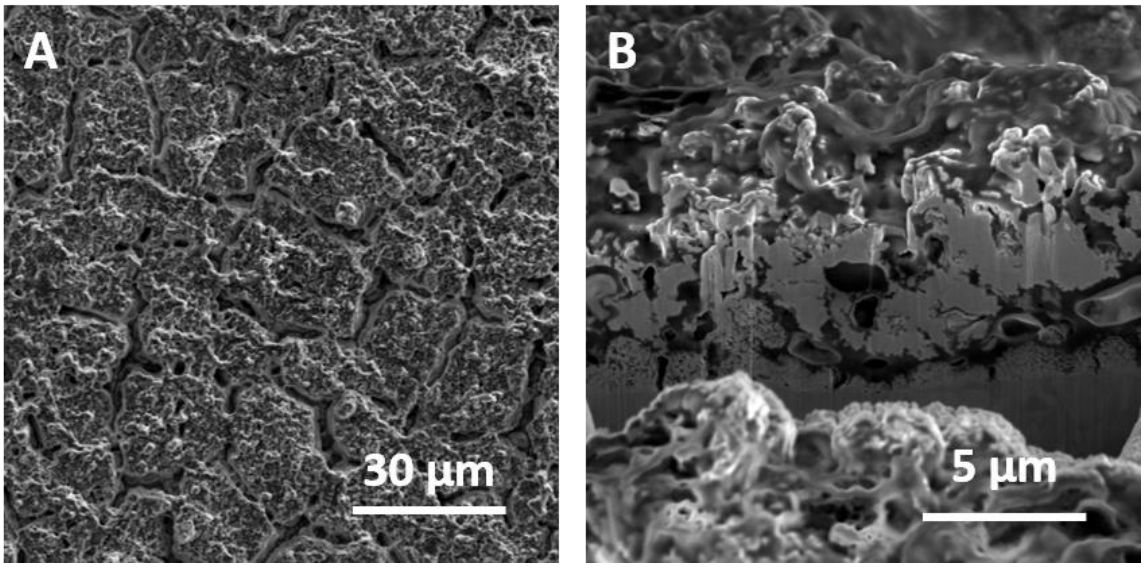

Figure 2.2. SEM images of electrodeposited Sn layer on Cu foil following 3 galvanostatic activation cycles at current density of 50 µA/cm^2 in the voltage range from 1 V to 0.05 V. A. surface of Sn layer shows cracks. **B**. FIB-milled cross-section view of Sn layer shows negative dendrites and Kirkendall voids.

The GITT measurements in literature[90], [96], [97] were usually done after several galvanostatic activation cycles at current densities in the range from 40 to 500 µA/cm^2 in order to form stable solid-electrolyte interface (SEI) layer. However, based on our morphology evolution results performed by galvanostatic cycles at a current density of 50 µA/cm^2 for 3 cycles (Fig. 2.2), the galvanostatic activation cycles will definitely generate pores, which would make the Sn layers not fulfilling the assumption of the linear diffusion equation (Fick's second law). What's more, based on Cui proposed mechanism of SEI layer formation-deconstruction

during charge-discharge cycles [98], SEI layer formed by galvanostatic cycling could not be more stable than that formed during the first charging-discharging cycle. In order to check the effect of SEI layer formation on the GITT measurements, GITT measurements with and without activation cycles were performed with results shown in Fig 2.3. The voltage profile of GITT measurements in the lithiation direction (Fig 2.3 A), two plateaus corresponding to phase transformation between Sn, Li_2Sn_5 and LiSn were shown to have higher quasi-equilibrium voltage and shorter duration of GITT without activation. Also, in the lithiation direction the calculated diffusion coefficients from GITT without activation were higher than those from GITT with activation by an order of 2 in the voltage range from 0.5 V to 0.8 V. These phenomenon might be caused by the fast kinetics of unstable SEI layer formation during the first two phase transformation reaction in the lithiation direction. The voltage profile (Fig 2.3 B) and the composition dependent calculated diffusion coefficients (Fig 2.3 D) of GITT measurements with and without activation in the delithiation direction were shown in good agreement with each other, which means the SEI layer were stable and not affecting the GITT measurement in the delithiation direction. Thus, the diffusion coefficient calculated from GITT measurement without activation in the delithiation direction would avoid impacts from both porous generated from galvanostatic cycles and unstable SEI layer. Thus, all diffusion coefficient calculated from GITT measurement in this work was hereafter obtained without galvanostatic cycling.

As shown in Fig 2.3 C and Fig 2.3 D, it is obvious that diffusion coefficients were much smaller in the phase transformation regions than in the single phase region. This is reasonable for during the phase transformation reaction, current was consumed by both new phase formation and Li diffusion, and $\frac{\partial E_s}{\partial \delta}$ would be extremely small in voltage plateaus for equilibrium potential should

be a constant value according to the Gibbs Phase Rule. The diffusion coefficient obtained from GITT measurements in-between phase transformation regions were summarized in Table 2.1. Relatively higher $\overline{D}_{Li}^{Sn}$ was observed in delithiation direction. While the diffusion coefficient tends to be constant in the lithiation direction, it exhibits a decreasing trend as Li composition in Li-Sn alloy is decreasing in the delithiation direction.

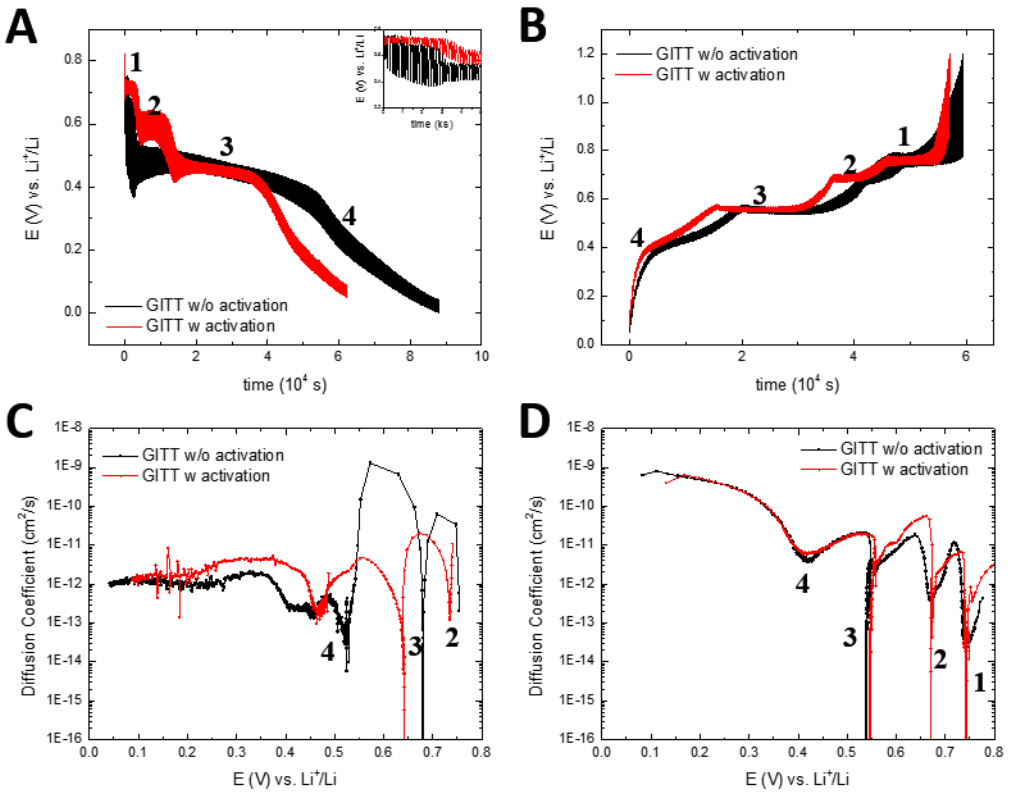

Figure 2.3. Effect of SEI layers on GITT measurements. GITT results with (red) and without (black) galvanostatic activation cycles. A, B. voltage profile of GITT measurement in the (**A**) lithiation and (**B**) delithiation direction with inset showing the first 5000 s of lithiation by GITT. **C, D**. diffusion coefficient results from GITT measurement in the (**C**) lithiation and (**D**) delithiation direction. Plateaus labeled as 1-3 depicts phase transformation reactions in eq. 1-3, respectively. Labeled region 4 corresponds to mixture of Li_xSn ($x > 2.33$).

Table 2.1. Summarize of diffusion coefficients calculated from GITT measurements.

	Lithiation direction	**Delithiation direction**

Diffusion Coefficient (cm^2s^{-1})	$10^{-12} - 10^{-11}$	$10^{-13} - 10^{-9}$

Typically in GITT measurements, the relaxation period is 2 to 10 times longer than the charging duration. The ratio between relaxation period and charging duration has to be carefully chosen so that the Li composition in the electrodeposited Sn layer tends to become homogeneous at the end of relaxation period and the measurement should not be tedious with too long relaxation duration. Thus, it is necessary to investigate the effect of relaxation period on diffusion coefficient obtained from GITT measurements. The differences in diffusion coefficients calculated from GITT measurements with relaxation versus charging duration ratio of 2 and 12 were compared in Fig. 2.4. Both GITT measurements were conducted without galvanostatic activation cycling. Thus, abnormal high diffusion coefficient was obtained in the first two phase transformation regions in the lithiation direction similar to that shown in Fig. 2.3 C. Except for the regions affected by unstable SEI layer formation, the differences in diffusion coefficient measured by GITT in the full Li composition range with two different relaxation durations were less than a factor of 10. Thus, the relaxation duration was chosen to be 100 s in this work hereafter.

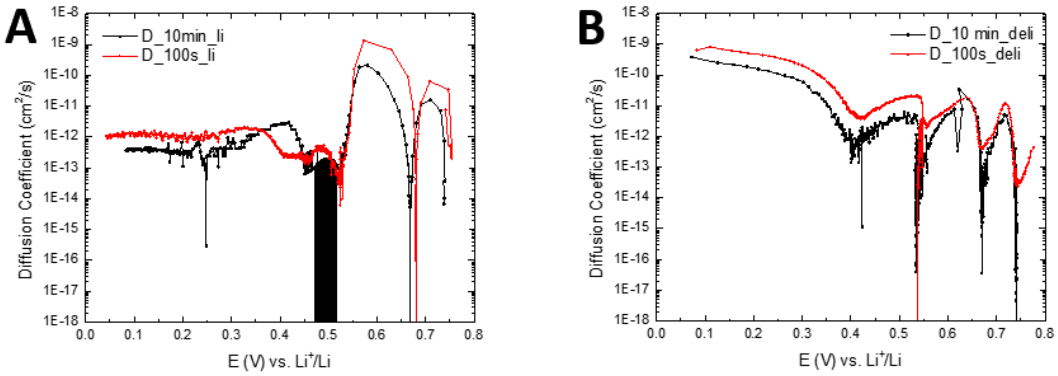

Figure 2.4. Effect of relaxation duration on GITT measurements. GITT results with relaxation duration of 100 s (red) and 10 min (black) were in good agreement in both (**A**) lithiation and (**B**) delithiation directions.

2.3 Composition-Dependent Intrinsic Diffusion Coefficient Of Li In Li-Sn Alloy Measured By PITT

Fig. 2.5 shows the potential dependence of the differential capacitance, C_{diff}, for lithiation and delithiation determined by PITT measurements. The three maxima labeled as peak 1-3 in Fig. 2.5 can be ascribed to phase transformation reaction happened on the three plateaus labeled as plateau 1-3 in Fig. 2.3 A and B. The relatively wide potential range labeled as peak 4 in Fig. 2.5 corresponds to the closely spaced phase transformation reactions happened on the slope changing region 4 in Fig. 2.3 A and B.

The voltage dependence of $\overline{D}_{Li}^{Sn}$ was obtained by PITT with galvanostatic activation cycles (Fig. 2.6). When comparing Fig. 2.5 and Fig. 2.6, it is seen that the minima in $\overline{D}_{Li}^{Sn}$ vs. E curve corresponded to the maxima on the C_{diff} vs. E curve. This phenomenon could be explained by current being consumed by phase transformation reactions. The $\overline{D}_{Li}^{Sn}$ obtained by long time approximation did not show clear trends and peaks since current measured during the last stage of potential step was almost constant. Thus, the $\overline{D}_{Li}^{Sn}$ obtained by the short time approximation seemed to be more reliable than that by the long time approximation. As shown in Fig. 2.6 C, the $\overline{D}_{Li}^{Sn}$ tends to decrease as E increases (and x of Li_xSn increases) is in consistent with $\overline{D}_{Li}^{Sn}$ from GITT measurements (Fig. 2.3 D). The diffusion coefficient obtained from PITT measurements outside phase transformation regions are summarized in Table 2.2.

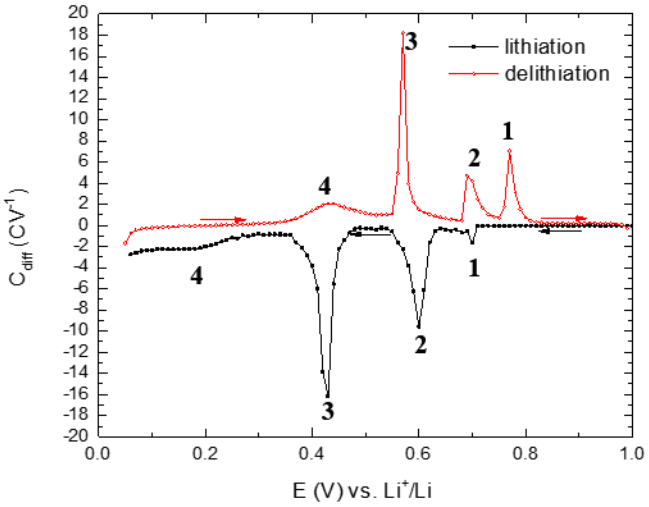

Figure 2.5. Plot of the differential capacity, C_{diff}, as a function of the electrode potential, E, obtained by PITT during lithiation (black) and delithiation (red). Labeled peaks correspond to two-phase coexistence region: **1**, Sn and Li_2Sn_5; **2**, Li_2Sn_5 and LiSn; **3**, LiSn and Li_7Sn_3; **4**, closely spaced transformation between the phases: Li_7Sn_3, Li_5Sn_2, $Li_{13}Sn_5$, Li_7Sn_2, and $Li_{22}Sn_5$.

Table 2.2. Summary of diffusion coefficient calculated from PITT measurements.

Diffusion Coefficient (cm^2s^{-1})	**Short time approximation**	**Long time approximation**
lithiation	$10^{-13} - 10^{-12}$	$10^{-12} - 8 \times 10^{-10}$
delithiation	$10^{-14} - 10^{-8}$	$2 \times 10^{-12} - 8 \times 10^{-12}$

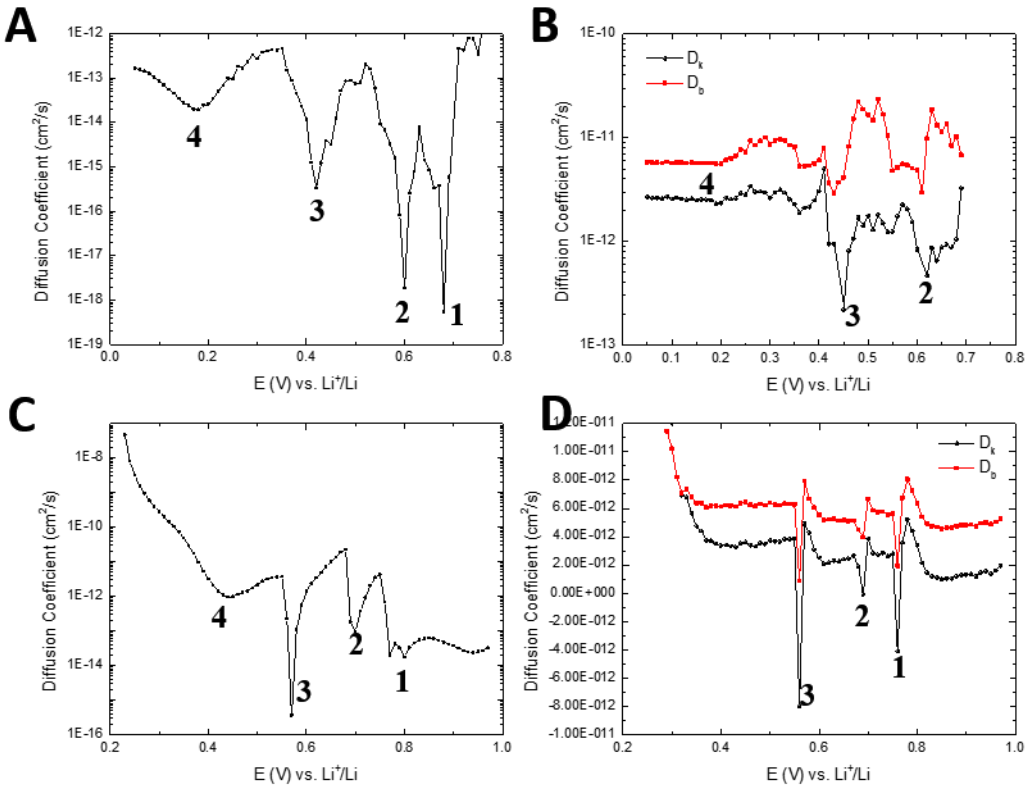

Figure 2.6. Plots of the interdiffusion coefficient of Li in LiSn, $\overline{D}_{Li}^{Sn}$, as a function of the electrode potential, *E*, obtained by PITT after galvanostatic activation cycles. A, C. $\overline{D}_{Li}^{Sn}$ calculated by PITT measurements with short time approximation for (**A**) lithiation and (**B**) delithiation. **C, D**. $\overline{D}_{Li}^{Sn}$ calculated by PITT measurements with long time approximation for (**A**) lithiation and (**B**) delithiation, where D_k and D_b stands for $\overline{D}_{Li}^{Sn}$ obtained by slope and intercept of *lnI* vs. *t*, respectively. Numbered regions correspond to phase transformation reactions between different phases: **1**, Sn and Li_2Sn_5; **2**, Li_2Sn_5 and LiSn; **3**, LiSn and Li_7Sn_3; **4**, closely spaced phase transformation between the phases: Li_7Sn_3, Li_5Sn_2, $Li_{13}Sn_5$, Li_7Sn_2, and $Li_{22}Sn_5$.

2.4 Diffusion Coefficient Of Li In Li-Sn Alloy Measured With Devanathan-Stachurski Cell

Both GITT and PITT measurements are time transient electrochemical titration technique. Here, a time-of-flight technique using the Devanathan Stachurski cell was applied to calculate the diffusion coefficient of Li in Li-Sn alloy. This technique is abbreviated to be DS measurement hereafter. In order to relate the diffusion coefficient of Li in Li-Sn alloy obtained from DS measurement to the morphology evolution results discussed in chapter 2.7-2.10, cathodic

polarization voltage of 400 mV was chosen for Sn sheets with thickness of 25 μm. According to the linear sweep voltammetry (Fig. 2.7) of the 25.4 μm thick Sn sheet recorded at 10 mV s^{-1} scan rate, the initial threshold of the anodic current was at voltage of 2.83 V. In order to rapidly oxidize any atomic Li reached the anodic side of the DS cell but not causing localized attack, the anodic polarization potential was chosen to be the open circuit potential of Sn sheets (~2.5 V < 2.83 V).

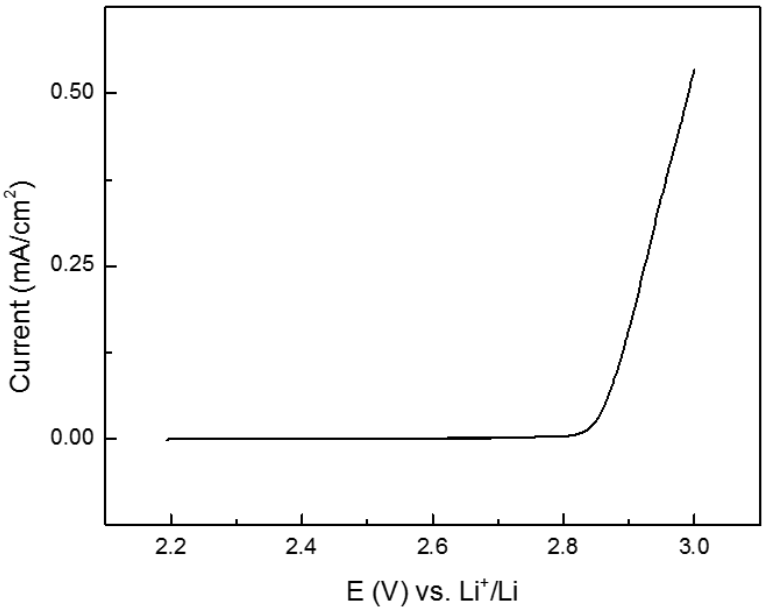

Figure 2.7. Linear sweep voltammetry of a piece of Sn sheet with thickness of 25.4 μm in electrolyte of 1 M $LiClO_4$ in propylene carbonate at sweep rate of 10 mV/s.

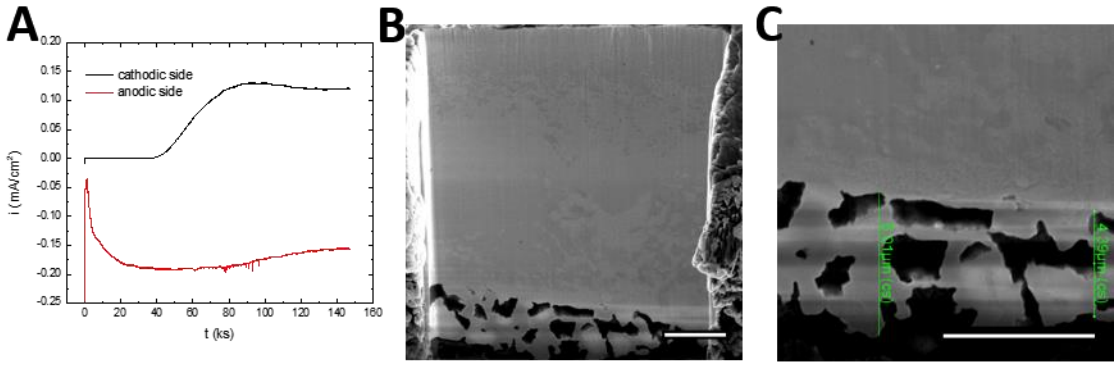

Figure 2.8. Results of Devanathan-Stachurski cell measurements at ambient temperature before pore penetrating through Sn sheets. A. plot of current density as a function of time shows cathodic plateau current is slightly smaller than the absolute value of anodic current. **B, C**. cross-section view of Sn foil after the D-S cell experiment shows negative nodule morphologies with penetration length of 4 to 6 µm at the anodic side (bottom). Scale bars, 5 µm.

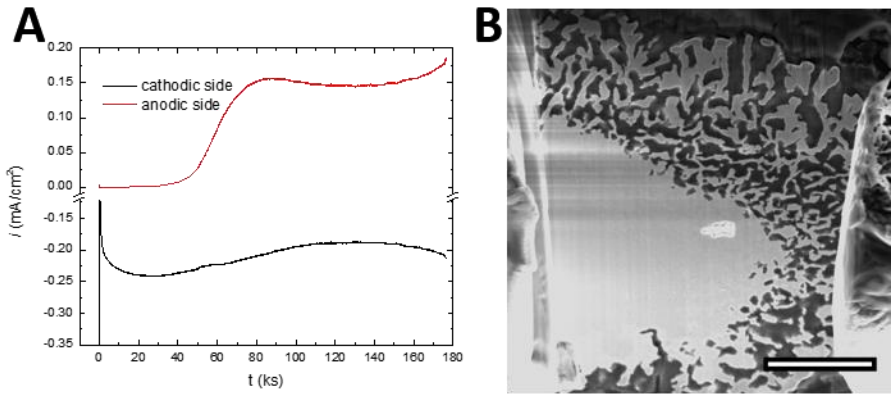

Figure 2.9. Results of Devanathan-Stachurski cell measurements at ambient temperature after pore penetrated through Sn sheets. A. plot of current density as a function of time shows cathodic plateau current is the same as the absolute value of anodic current. **B**. cross-section view of Sn foil after the D-S cell experiment shows negative dendrite morphologies penetrated through the full thickness. Scale bar, 5 µm.

Fig. 2.8 and Fig. 2.9 show current-time responses and resulted cross-section morpholoies from DS measurements at total experiment duration of 145 ks and 178 ks. Fig. 2.8 A shows typical DS measurement current-time responses on anodic side (black line) to potentiostatic polarization on cathodic side (red line). The anodic current-time response can be divided into three distinguished

stages: stage 1, zero-current stage corresponds to atomic Li not passing through the full thickness of 25.4 μm thick Sn sheet and not reaching the anodic side of DS cell; stage 2, current-rising stage depicts Li concentration gradient transferring into a linear gradient as a function of distance to the anodic side Sn surface; stage 3, current plateau corresponds to steady-state oxidation condition of lithium that was inserted in the A-side and reached the B-side of DS cell. The difference between plateau current in the B-side and corresponding current in the anodic side is attributed to Li diffusion into but not through the Sn sheet. As shown in Fig. 2.8 B and C, the cross section morphology of Sn sheet after DS measurement shows negative dendrite structures in the anodic side. This phenomenon proved that Li permeation through Sn sheet is a diffusion-limited process. Fig. 2.9 A shows anodic current-response with one more current rising stage other than the three typical stages in Fig. 2.8 A. This additional current rising stage can be attributed to the formation of cracks and negative dendrite structures penetrating through the Sn sheets during the course of dealloying. A typical SEM image of the cross section of Sn sheet is shown in Fig. 2.9 B. The cross section shows perfect negative dendrite structures oriented perpendicular to the anodic surface of Sn sheet and penetrated throughout the full thickness of Sn sheet.

To calculate the diffusion coefficient of Li in Li-Sn alloy the surface concentration on the cathodic side is maintained at a constant level by maintaining the potential to be 400 mV, while on the anodic side it is always zero by oxidizing any atomic Li reaching the anodic surface of Sn sheets at voltage ~ 2.5 V. With the record of the instantaneous rate of Li permeation shown in Fig. 2.9 A the Li diffusion coefficient in Li-Sn alloy, $\overline{D}_{Li}^{Sn}$, can be calculated from the lag time, t_{Lag}, according to eq. 19. Here the t_{Lag} was obtained by spotting the time at which the anodic current is 0.63 times the steady-state value, J_{∞} [73]. Volume expansion and phase transitions of

Sn sheets during dealloying were not taken under consideration when calculating the diffusion coefficients of Li in Li-Sn alloy.

$$t_{Lag} = 0.63J_{\infty} = \frac{L^2}{6\overline{D}_{Li}^{Sn}} \tag{21}$$

where t_{Lag} is the time lag, which is the time at which the current reaches 63% of the steady-state anodic current flow , J_{∞}. The $\overline{D}_{Li}^{Sn}$ obtained from three repeating DS cell measurements is $1.683 \times 10^{-11} \pm 5.312 \times 10^{-14}$ cm^2/s, which is in good agreement with the GITT and PITT measurements at similar Li composition.

2.5 Comparison Of Diffusion Coefficients Of Li In Li-Sn Measured By PITT, GITT And DS Techniques.

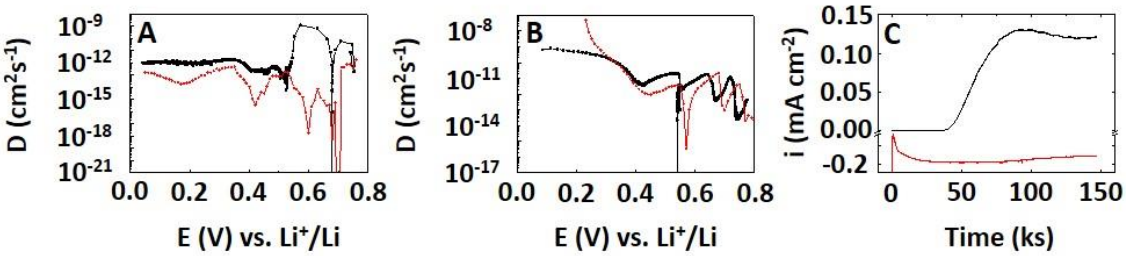

Figure 2.10. Ambient temperature measurements of the intrinsic Li diffusivity. A. $\overline{D}_{Li}(E)$ determined from lithiation titrations, GITT (black curve) and PITT measurements (red curve). **B.** $\overline{D}_{Li}(E)$ determined from de-lithiation titrations GITT (black curve) and PITT measurements (red curve). **C.** Devanathan-Stachurski cell result showing chronocoulometry at 0.400 V Li+/Li for lithiation (red curve) and the evolution of the current density on the anodic side of the membrane.

Values of $\overline{D}_{Li}^{LiSn}$ obtained by PITT, GITT with short time approximation and DS measurements are compared in Fig. 2.10. Similar to the results from other researchers [89]–[91], large dips in diffusion coefficients were found in phase transformation regions since the current was consumed by both new phase formation and Li diffusion (PIIT) or because the electrochemical

potential is constant in the two-phase regions (GITT). Since the diffusion coefficients in the phase transformation regions are inaccurate, only those in the single-phase regions are taken into consideration hereafter. Table 2.3 shows that the calculated values of $\overline{D}_{Li}^{LiSn}$ from PITT and GITT measurements for lithiation and delithiation were in reasonable agreement. As discussed in chapter 2.2 (GITT for Sn), the unusually large $\overline{D}_{Li}^{LiSn}$ determined from GITT measurements in the Li_2Sn_5 and LiSn phases might be caused by fast kinetics of unstable SEI layer formation during the pre-charging stage of GITT measurements. Except for this pre-charging stage, the differences in $\overline{D}_{Li}^{LiSn}$ determined from PITT and GITT measurements were less than a factor of 100 in the lithiation direction. Not including the data for the Li_7Sn_2/Li_{22}Sn5 phases, the differences in diffusion coefficients calculated from PITT and GITT measurements were less than a factor of 6. The reason why $\overline{D}_{Li}^{LiSn}$ increases with increasing Li composition in delithiation is still unknown. Considering both the GITT and PITT measurement results, the diffusion coefficients are of order 10^{-13} - 10^{-12} cm^2s^{-1} in the lithiation direction and 10^{-12} - 10^{-11} cm^2s^{-1} in the delithiation direction. One typical current response of DS measurements is shown in Fig. 2.10 C. The $\overline{D}_{Li}^{LiSn}$ obtained from three separate experiments in the Devanathan-Stachurski cell was $1.7 \times 10^{-11} \pm 5 \times 10^{-14}$ cm^2s^{-1}, which is in good agreement with the GITT and PITT results.

Table 2.3. Summarize of $\overline{D}_{Li}^{Sn}$ (cm^2s^{-1}) calculated from GITT and PITT measurements in corresponding single-phase regions.

phase	**GITT**		**PITT**	
	lithiation	delithiation	lithiation	delithiation
Li_2Sn_5	6.4×10^{-11}	1.2×10^{-11}	1.9×10^{-12}	4.3×10^{-12}
LiSn	1.3×10^{-9}	1.9×10^{-11}	2.1×10^{-13}	2.2×10^{-11}
Li_7Sn_3/Li_5Sn_2/$Li_{13}Sn_5$	1.8×10^{-12}	2.1×10^{-11}	4.6×10^{-13}	3.7×10^{-12}
Li_7Sn_2/ $Li_{22}Sn_5$	1.4×10^{-12}	8×10^{-10}	1.7×10^{-13}	4.7×10^{-8}

2.6 Diffusion Coefficients Of Li In Li-Sn Alloys As a Function of Temperature

In order to get the activation energy of diffusion, GITT measurements were conducted at different temperature of 30, 51, 80, 100 and 110 ˚C. The potential dependence of the chemical diffusion coefficient at five different temperatures from 30 ˚C to 110 ˚C is shown in Fig. 2.11 A. The influence of quasi-equilibrium potential, E, on $\overline{D}_{Li}^{Sn}$ seemed to be similar at all temperatures with large dips appeared in phase transformation regions. As temperature increases, $\overline{D}_{Li}^{Sn}$ in single phase regions of Li_2Sn_5, LiSn and Li_7Sn_3/Li_5Sn_2/$Li_{13}Sn_5$ all increased. In these three single phase regions, the plot of $\overline{D}_{Li}^{Sn}$ versus 1/T (Fig. 2.11 B) could be fit to three straight lines, whose R-squared value are all larger than 0.97. Fits to the Arrhenius equation, $\overline{D} = \overline{D}_o \exp(-\frac{E_a}{RT})$ are summarized in Table 2.4. The activation energy of single phase Li-Sn alloy is in the same magnitude of activation energy of Li diffusion in Li-Al alloy with 50-55 at.% Li (47.7 kJ/mol obtained by Huggins and Weppner [72]).

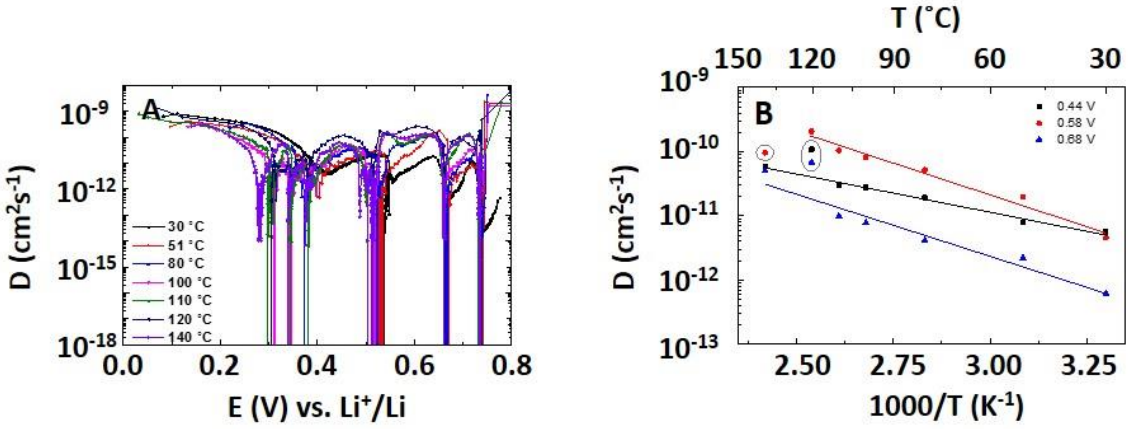

Figure 2.11. Results from GITT measurements obtained at elevated temperature in the delithiation direction. A. plot of $\overline{D}_{Li}^{Sn}$ as a function of quasi-equilibrium potential, E. **B**. Arrhenius plots of $\overline{D}_{Li}^{Sn}$ versus 1/T at different quasi-equilibrium potentials of 0.44 V, 0.58 V and 0.68 V, which corresponds to single phase regions of Li_2Sn_5, LiSn and Li_7Sn_3/Li_5Sn_2/$Li_{13}Sn_5$, respectively.

Table 2.4. Summarize of E_a （J/mol） and $\bar{D}_0$ (cm^2s^{-1}) calculated from GITT measurements at elevated temperature in corresponding single phase regions.

phase	E_a （J/mol）	$\bar{D}_0$(cm^2s^{-1})
Li_2Sn_5	37374.08	1.69×10^{-6}
LiSn	37861.81	1.86×10^{-5}
Li_7Sn_3/Li_5Sn_2/$Li_{13}Sn_5$	22489.71	3.82×10^{-8}

2.7 Effect Of Li-Sn Alloy Dealloying Potential On Morphology Evolution In Linear Sweep Voltammetry And Chronoamperometry

Owing to the fragility of fully lithiated Sn sheets, samples were potentiostatically alloyed only to a voltage of 400 mV vs. Li+/Li to form the phases Li_2Sn_5, LiSn and Li_7Sn_3. The fragility results from diffusion-induced stresses and micro-cracking of the 25 μm-thick Sn sheets used in this portion of our work. These cracks appeared mainly toward the middle of the Sn sheet and did not obscure our ability to identify the smaller length scale morphologies that evolve upon de-lithiation. As a note, we observed no such cracking in the electrodeposited 2 μm-thick electrodeposited films used for the determination of the Li diffusivities. It is difficult to determine whether in addition to Li_7Sn_3, higher concentration Li phases such as Li_5Sn_2, $Li_{13}Sn_5$, Li_7Sn_2 and $Li_{22}Sn_5$ formed since (as shown later in Fig. 2.13 A) the ambient temperature lithiation/delithiation voltage vs. Li concentration behavior for LixSn for x > 2.33 behaves as if the system was single-phase [39–41]. Clearly, not all of the intermetallic phases that appear on the equilibrium Li-Sn phase diagram are accessible by electrochemical lithiation at 300 K.

To investigate the effect of dealloying potential and phase transformation reactions on morphology evolution, dealloying polarization behavior for Sn sheets with normalized current

density, i^* (=current density/$\sqrt{scan\ rate}$), as a function of potential at different scan rates were examined (Fig. 2.12 A). At sweep rate of 0.3 mV/s, since the voltage sweeping rate is much faster than the dealloying rate of Li from surface present Li-Sn phases, only one broad convoluted wave were observed. At sweep rates of 0.017 mV/s, 0.03 mV/s and 0.087 mV/s, the three waves labeled in Fig. 2.12 A correspond to delithiation of Li-Sn phases initially present and those that may be evolving on the electrode surface during potential scanning. At sweep rates lower than 0.087 mV s^{-1}, three waves are apparent that we associate with dealloying of Li_xSn ($x \geq 2.33$), LiSn and Li_2Sn_5.

According to the solution of Fick's 2nd law with initial and boundary conditions of linear sweep voltammetry at room temperature (eq. 22), the normalized peak current density should be independent of scan rate for diffusion-controlled process [99]. Accordingly, the current density, *i*, has been scaled by the square root of the voltage scan rate, $i^* = i/\sqrt{dV/dt} = i/\dot{V}^{1/2}$, in order to identify the waves in the LSV associated with diffusion-limited dealloying from those that are not. Thus, wave 2 and 3 in Fig. 2.12 A were concluded to be diffusion controlled dealloying peaks associated to the negative dendrite structure formation. On the other hand, Wave 1 in Fig. 2.12 A was predicted to be the percolation dissolution peak associated to bicontinuous porous morphology evolution for the peak scaled current of Wave 1 increased with the sweep rate. This hypothesis was proven by following results of potentiostatic dealloying. One can see that wave 1 shifts to higher potentials with increasing sweep rate displaying a shift of +17 mV for sweeps of 0.17 and 0.30 mVs^{-1}. This shift is consistent with the association of wave 1 with an irreversible process such as percolation dissolution [99].

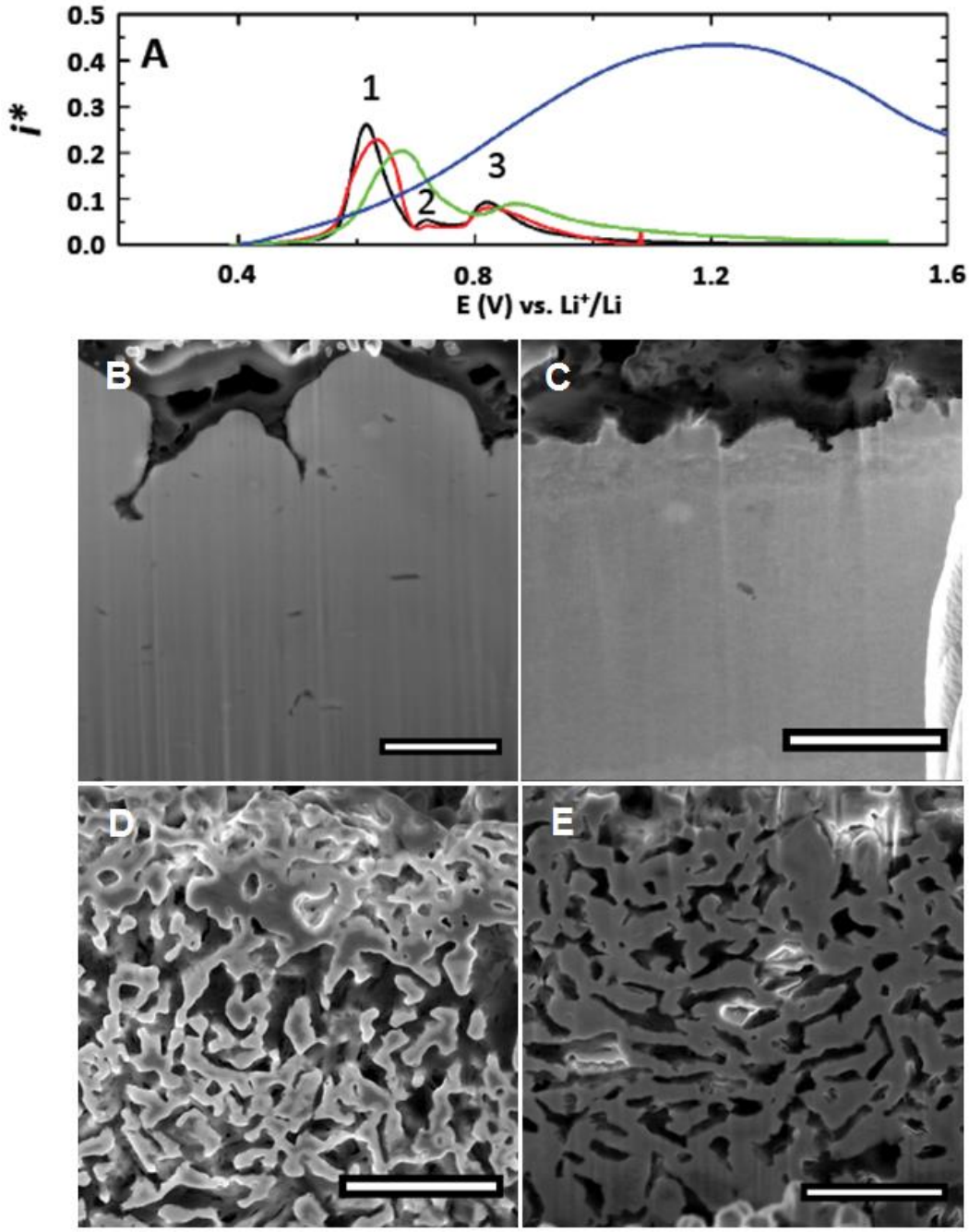

Figure 2.12. Linear sweep voltammetry and morphology evolution at fixed potential vs. Li^+/Li. A. LSV showing the normalized current, i^* (= current /$\sqrt{scan\ rate}$) vs. potential at scan rates of 0.017 mV/s (black), 0.03 mV/s (red), 0.087 mV/s (green) and 0.3 mV/s (blue). Labels 1-3 refer to waves discussed in the text. **B, C**. Morphology obtained at a potential of 0.53 V (**B**) and 0.60 V (**C**) showing surface perturbations resulting from de-lithiation below the critical potential for porosity evolution. **D, E**. Bi-continuous morphologies evolving from percolation dissolution obtained at a potential of 0.70 V (**D**) and 0.75 V (**E**). All scale bars are 2 μm.

To further prove that wave 1 was associated to percolation dissolution, the potentiostatic dealloying morphology evolution of electrodeposited Sn layer on Cu with thickness of 7 μm was examined. The width of wave 1 at half-maximum is ~ 100 mV, so based on the LSV behavior we estimate E_{crit} is 600 ± 50 mV. In order to test this hypothesis, mixture of LiSn and Li_7Sn_3 was prepared by potentiostatic lithiation at voltage of 400 mV and then potentiostatically delithiated at voltage of 530 mV (Fig. 2.12 B), 600 mV (Fig. 2.12 C), 700 mV (Fig. 2.12 D), and 750 mV (Fig. 2.12 E). As shown in Fig. 2.12 B and C, the cross-section view of the Sn layer delithiated at voltage lower than peak 1 potential showed the evolution of a roughened surface that we associate with layer-by layer dissolution of finite-size Li-rich (Li_xSn; $x \geq 2.33$) surface domains. In Fig. 2.12 B, Kirkendall voids shown are smaller near the surface and larger into the alloy. Such a size distribution was observed in noble-metal dealloy at elevated temperature [100] and could be contributed to a consequence of the decreasing vacancy supersaturation as a function of distance into the alloy. As shown in Fig. 2.13, at 600 mV the chronoamperometry displays an approximate $t^{-1/3}$ decay for the first 500 s followed by a steeper decay of $\sim t^{-1}$. At 530 mV we observed weaker power-law behavior that we associate with mixed diffusion and activation control. Fig. 2.12 D and E depict bicontinuous porous morphologies in the cross sections of Sn layers delithiated at voltage higher than the wave potential of wave 1 and the corresponding chronoamperometry shows that the current density maintained a relatively constant value ~ 2 $mAcm^{-2}$ for ~ 800 s until it began a steep decay following $\sim t^{-1}$ behavior that we associate with secondary dealloying occurring from ligaments formed during the initial 800 s. These morphology differences of Sn sheets delithiated at different voltages proved that the critical potential for bicontinuous porous morphology evolution lies in two-phase coexistence voltage

region of LiSn/Li_7Sn_3, which is in good agreement with our results on effect of dealloying rate on morphology evolution.

$$i_P = (2.6 \times 10^5) n^{3/2} A D_{Li}^{1/2} C_{Li}^{*} \nu^{1/2} \quad (22)$$

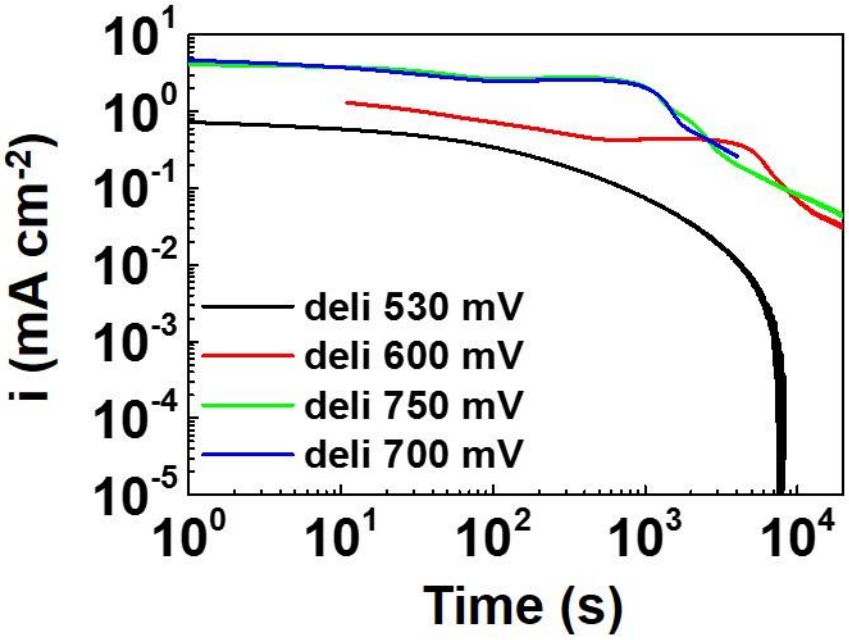

Figure 2.13. Current decay curves for dealloying of Li_xSn (x>2.33, Sn sheets lithiated at 400 mV) at different potentials: black line, 530 mV; red line, 600 mV; green line 750 mV; violet line, 700 mV.

2.8 Composition Dependence Of Morphology Evolution: Planar Li-Sn Sheets

Given that the critical potential for pristine Li_xSn alloy with x higher than 2.33 lies in two-phase coexistence voltage region of LiSn/Li_7Sn_3, we tried to ascertain if dealloying of the LiSn phase, at high enough potentials could result in percolation dissolution and a corresponding bi-continuous morphology. The effect of pristine alloy composition on morphology evolution in chronopotentiometry and chronoamperometry for Sn sheets with thickness of 25.4 μm is shown in Fig. 2.14. Planar Sn hosts charged to varying Li concentrations were fabricated by

potentiostatic lithiation at indicated potential, which defines the designated alloy composition [44], [46], [54]. Here, the one to one correspondence of voltage and Li content was assigned according to lithium-tin voltage profile (Fig. 2.14 A) from GITT measurements in the lithiation direction at room temperature for electroplated 2 μm thick Sn layer with galvanostatic activation cycles. According to the voltage profile shown in Fig. 2.14 A, the dealloyed Sn sheets shown in Fig. 2.14 B and C was lithiated at voltage of 600 mV to obtain an original alloy with mostly LiSn phase with partial Li_2Sn_5 phase (x in Li_xSn ~ 0.7). Similarly, alloy with phase mixture of LiSn and Li_7Sn_3 (Li_7Sn_3 dominated, x in Li_xSn ~ 2.25) was lithiated at voltage of 400 mV for Sn sheets shown in Fig. 2.14 D and E.

The lithiated planar Sn electrodes with well-defined composition of Li were then dealloyed either galvanostatically (Fig. 2.14 B and D) or potentiostatically (Fig. 2.14 C and E) and then got the cross-section morphology characterized by FIB and SEM. Fig. 2.14 D shows bicontinuous porosity evolved from Li-Sn alloy with 41 at.% Li, which was galvanostatically delithiated at current density of 40 mA/cm^2. Similarly, when Li-Sn alloy with 69 at.% Li was dealloyed potentiostatically at voltage of 1 V, bicontinuous porous morphology formed as shown Fig. 2.14 E. Such bicontinuous porous morphology in analogous with noble-metal alloy dealloyed morphology is consistent with the percolation-based model of dealloying [17]. Our results demonstrate that bicontinuous porous morphology could evolve through percolation dissolution in dealloying of certain Li-Sn alloy, whose Li composition is equal to or above a threshold composition, Li_7Sn_3 (~ 52 at.% Li).

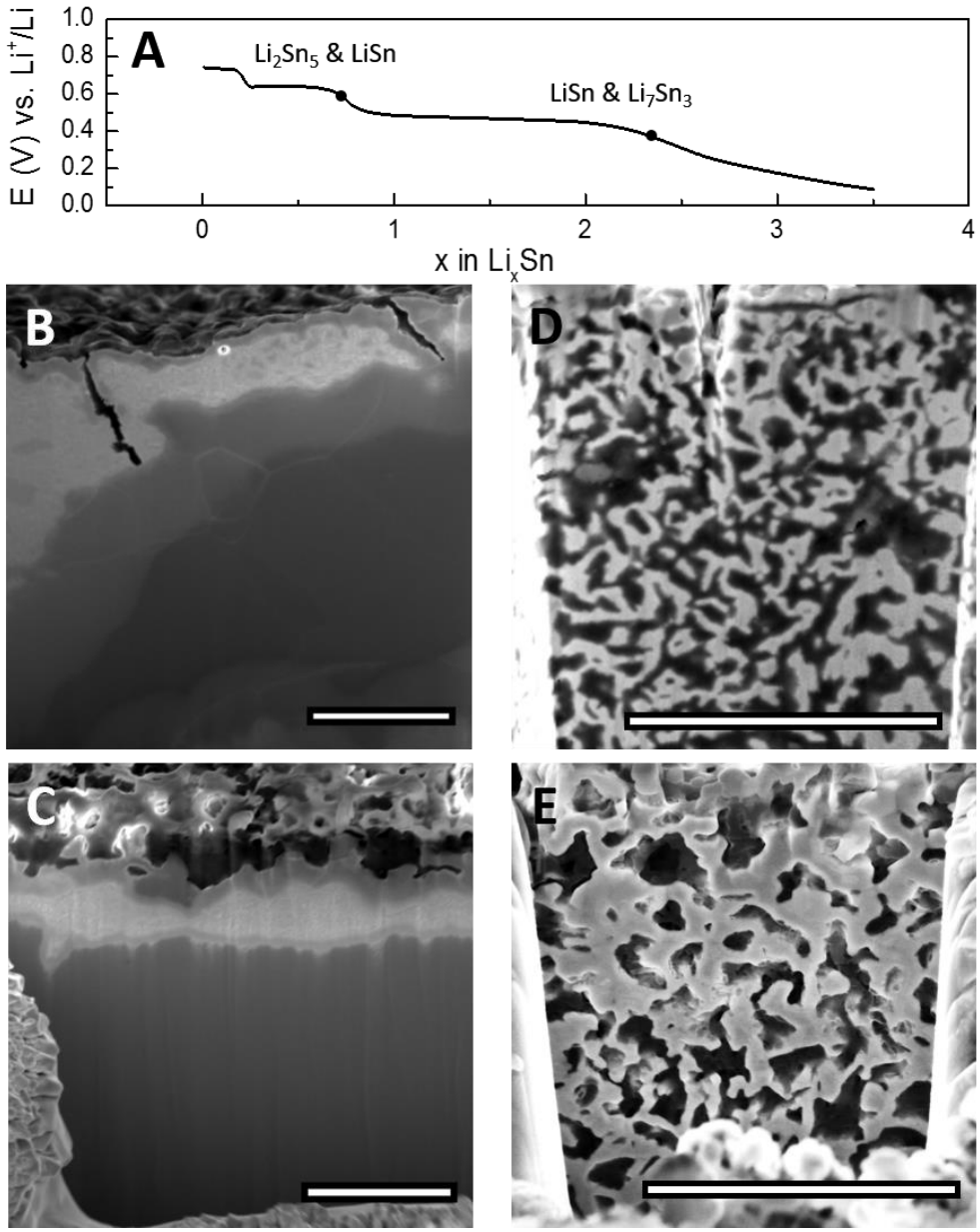

Figure 2.14. The effect of alloy composition on morphology evolution in galvanostatic (B, D) and potentiostatic (C, E) dealloying. A. Quasi-equilibrium potential as a function of alloy composition obtained by GITT measurement for electrodeposited Sn layer on Cu in the lithiation direction at ambient temperature with galvanostatic activation cycles. **B, C**. Negative dendrite structures obtained from mixture of Li_2Sn_5 and LiSn dealloyed at current density of 40 mA/cm^2 (**B**) or at potential of 2.5 V (**C**). **D, E**. Bicontinuous porous morphology resulted from mixture of LiSn and L_7Sn_3 dealloyed at current density of 40 mA/cm^2 (**D**) or at potential of 1 V (**E**). Scale bars, 4 μm.

Below this threshold composition, dealloying is supported by Li bulk diffusion process. As a process isomorphic to dendrite formation in electrodeposition, for high enough dissolution rate and large enough dealloying driving force, negative dendrites could evolve from diffusion-limited dealloying. Here, Fig. 2.14 B shows the negative dendrite morphology resulted from galvanostatic delithiation at current density as high as 40 mA/cm^2 of 41 at.% Li Li-Sn alloy. As shown in Fig. 2.14 C, even though the dealloying potential was as high as 2.5 V (which is the highest selective dissolution potential allowed on dealloying of Li-Sn system), only sinusoidal-like surface roughness with a mean wavelength and amplitude corresponding respectively to the mean separation and diameter of Li deficient phase, Li_2Sn_5, were observed (Fig. 2.14 C). When Li-Sn alloy contains mostly LiSn but small amount of Li_2Sn_5, even though the dealloying driving force was as large as 2.5 V and dealloying rate was as fast as at a current density of 40 mA/cm^2, dealloying morphology evolution was still dominated by diffusion limited dealloying since Li composition was below the percolation threshold for percolation dissolution. These experiments are consistent with the LSV data and revealed that for the conditions employed, the Li_2Sn_5 and LiSn phases do not dealloy by a percolation dissolution mechanism.

In analogous with dealloying morphology evolution in noble-metal alloys at ambient temperature [25], [101], [102], there exists a composition threshold for bicontinuous porosity to evolve in Li-Sn alloy systems. Above this composition threshold, percolation dissolution dominated the dealloying mechanism of Li-Sn system for high enough selective dissolution rate. In noble-metal alloys, the lower active element composition bound is called the parting limit, below which only surface dealloying could happen and dealloying cannot proceed for bulk diffusion of alloy elements is negligible at ambient temperature and passivation layer of noble component would form through surface diffusion [103], [104]. Different from the case of noble-metal alloy

dealloying, even though no bicontinuous porosity were formed in Li-Sn system when Li composition is below the composition threshold, dealloying still proceeded through bulk diffusion of Li. Negative dendrite structures were evolved at high enough selective dissolution rate.

2.9 Effect Of Li-Sn Alloy Dealloying Rate On Morphology Evolution In Chronopotentiometry

The effect of dealloying rate on morphology evolution in chronopotentiometry for Sn foils is shown in Fig. 2.15. For low enough dealloying rates, we expect the chronopotentiometry to result in at least four regions or stages of behavior: region 1, corresponding to dealloying of the single-phase-like behavior of high concentration Li phases (Li_xSn, $x \geq 2.33$); region 2, corresponding to a voltage plateau resulting from dealloying within two-phase $LiSn/Li_7Sn_3$; region 3 corresponding to a voltage plateau resulting from dealloying within two-phase $Li_2Sn_5/LiSn$ and region 4 corresponding to dealloying within two-phase Li_2Sn_5/Sn. At higher dealloying rates (above ~ 40 □Acm^{-2}) several or all of these regions become convoluted. Based on the LSV and chronoamperometry results, as discussed above, we can expect the formation of bicontinuous structures so long as the dealloying potential achieves a value of 550 mV (lower bound of E_{crit}) prior to delithiation of the parent phase to the LiSn composition. Otherwise dealloying will be supported by solid-state diffusion and the corresponding morphologies that will form are negative dendrite structures and/or Kirkendall voids.

When dealloying current density is equals to or higher than 4 mA/cm^2, bicontinuous porous morphologies were observed both at the surface (Fig. 2.15 A) and the cross sections (Fig. 2.14 D and Fig. 2.15 D, G) of dealloyed Sn sheets. By comparing Fig. 2.14 D and Fig. 2.15 A, it is obvious that the length scale of bicontinuous porous morphology of the surface is larger than that

of the cross section. This surface larger length scale could be a combination result of surface diffusion smoothening and collapse of ligament. In noble-metal alloys, an analogous larger surface ligament size after post-dealloying annealing phenomenon was referred to surface diffusion [105], [106] and Rayleigh instability[31]. The ligament size of those bicontinuous porous morphologies increased from 164±52 nm, to 251±96 nm, and then to 321±104 nm as dealloying current densities decreased from 40 mA/cm^2, to 20 mA/cm^2, and to 4 mA/cm^2. As the dealloying rate increased the ligament size decreased and this behavior is typical of percolation dissolution in noble metal alloy systems such as AgAu. The bicontinuous porosity formation could be predicted from the corresponding chronopotentiometry as shown in Fig. 2.15 J, which demonstrates that the dealloying voltage achieved values of 550 mV within 1-10 s at these current densities.

At dealloying current densities of 2 mA/cm^2 and 0.4 mA/cm^2 (Fig. 2.15 B, E, H), the FIB cross-sections show a bi-continuous structure with ligament diameters ~ 1□□m with a substructure within the ligaments. As shown in Fig. 2.15 H, this substructure corresponds to a smaller length scale bi-continuous structure. We can understand the evolution of this based on the chronopotentiometry (Fig. 2.15 K) showing that the region 1 voltage was below 500 mV. During this stage, delithiation was supported by Li-diffusion to the alloy/electrolyte interface, since the potential was not large enough for a percolation dissolution process to operate. However, the total charge associated with dealloying in this region was ~ 0.03 of the total lithiation charge of ~ 6 C. Within region 2, the voltage plateau at ~ 555 mV was of ~36,000 s in duration after which ~ 0.50 of the lithiation charge remained. Region 3 delithiation was characterized by a voltage plateau at ~800 mV that lasted for ~18,000 s (after which ~ 0.25 of the lithiation charge remained). This suggests that the larger length-scale bi-continuous structure

evolved in the second stage after which the remaining lithium was partitioned into LiSn and Li_7Sn_3. Our results suggest that the ligaments comprising this porous structure retained a mole fraction of Li ~ 0.50 or slightly larger. Subsequent dealloying of the retained Li within the ligaments likely occurred in region 3 (~ 750 mV) by percolation dissolution resulting in the smaller length scale bi-continuous structure. For larger length scale bicontinuous porosity, the ligament size is evident to increase with decreasing dealloying rate (Fig. 2.15 E).

Fig. 2.15 C, F, I depict negative dendrite with Kirkendall voids along grain boundaries morphologies of Sn sheets following dealloying at current density of 40 $\mu A/cm^2$. As shown in Fig. 2.15 C, negative dendrite structures formed from diffusion-limited dealloying were separated from each other. This is because the Li concentration gradient region formed surrounding each negative dendrite determined the only definite diffusion path for Li atom in the adjacent parent phase region. No bicontinuous porous morphology was formed for selective dissolution was not sufficient enough comparing to the comparably fast surface diffusion smoothening process. When a compact Sn-rich layer formed at the electrode/electrolyte interface, dealloying started to proceed through diffusion-limited mechanism, where negative dendrites and Kirkendall voids take place. Kirkendall voids agglomerated along grain boundaries (Fig. 2.15 I) demonstrating the important role of grain boundary diffusion for solid-state mass transport. Apparently the grain boundaries serve as a sink for vacancies and correspondingly vacancy clusters form by vacancy agglomeration. As shown in Fig. 2.15 L, Region 1 occurs at low potential over 7500 s and region 2 occurs at ~540 mV over ~ 400,000 s. There is a considerable amount of Li removed from the alloy within region 2 (~ 0.53 of the total lithiation charge) and it seems likely that during this time most or all of the high concentration Li phases (Li_xSn, $x \geq 2.33$) disappeared. Region 3 dealloying occurred over ~ 275,000 s during which the potential increased

from about 700 to 800 mV. At this current density all of the higher content Li phases susceptible to percolation dissolution disappeared prior to the time the voltage reached the critical potential.

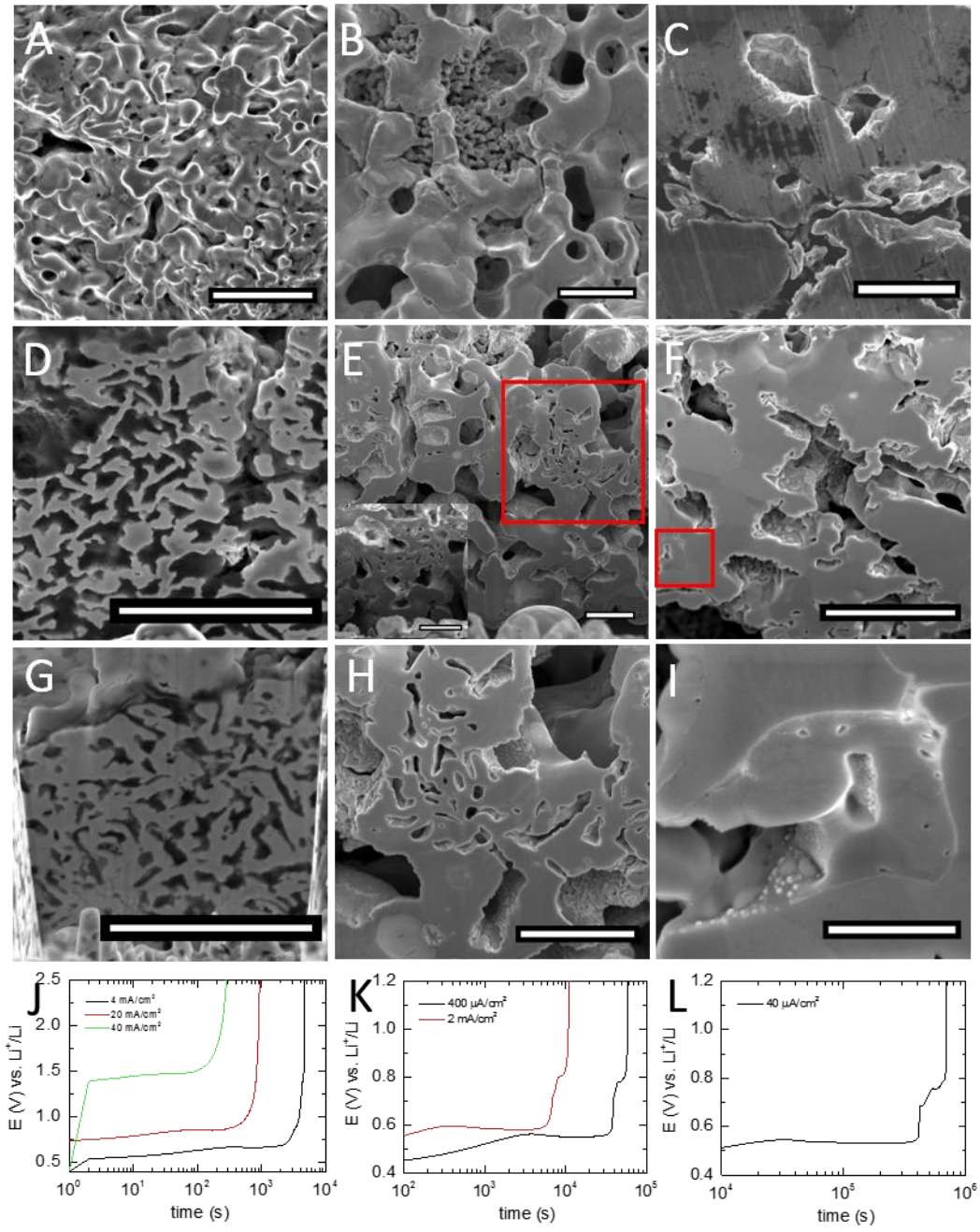

Figure 2.15. Effect of dealloying rate on morphology evolution. Sn sheets with thickness of 25 um were potentiostatically lithiated to $LiSn/Li_7Sn_3$ at voltage of 0.4 V and then galvanostatically delithiated at different current densities/dealloying rates: A, 40 mA/cm^2; **D**, 20 mA/cm^2; **G**, 4 mA/cm^2; **E inset**, 2 mA/cm^2; **B, E, H**, 0.4 mA/cm^2; and **C, F, I**, 40 µA/cm^2.

A – C. Surface view SEM images of Sn sheets. **D – I**. FIB cross-sections of Sn sheets. **J – L**. Voltage profile for Sn sheets delithiation. **A, D, G**. Bicontinuous porous morphologies with ligament diameter increases with decreasing dealloying rate. **B, E, H**. Bicontinuous porous with different length scale; **H** is the magnified squared cross section of **E** showing smaller scale bicontinuous porosity. **C, F, I**. Negative dendrite with Kirkendall void structures; **I** is the magnified squared cross section of F showing grain-boundary segregated Kirkendall voids. All scale bars are 4 μm except for that in (**I**), which is 800 nm.

2.10 Effect Of Sn Planar Host Thickness On Dealloying Morphology Evolution In Chrono-Amperometry And Potentiometry

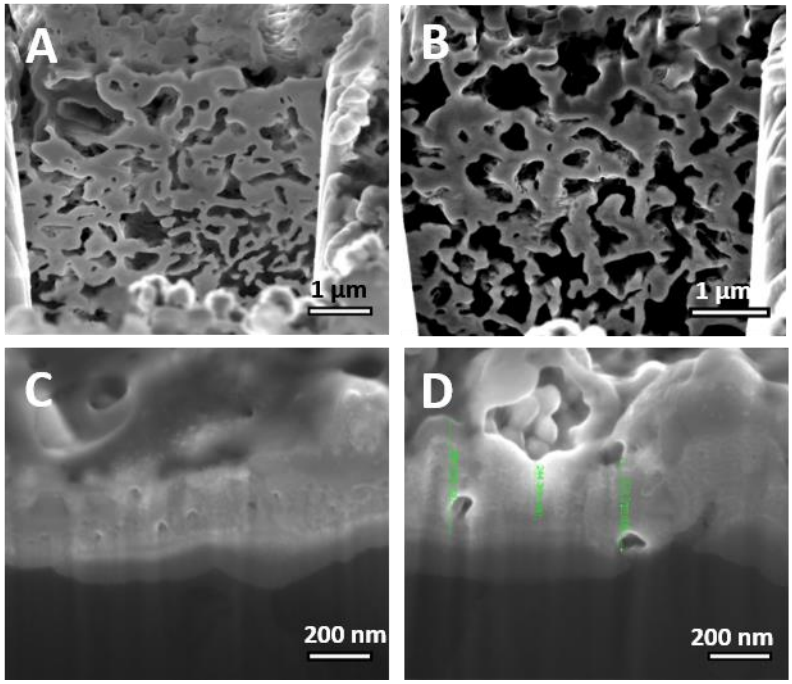

Figure 2.16. Potentiostatic dealloying (at potential of 1 V) results of planar host LiSn/Li_7Sn_3 FIB milled cross-section views with different Sn layer thickness. A, B. Bicontinuous porous morphology with larger ligament size near grain boundary and electrode/electrolyte interface of free standing Sn sheets with thickness of 25 μm, which was potentiostatically lithiated at 400 mV. **C, D**. Kirkendall voids and nanopores (residual of ligament collapsing) structures near Sn and Cu interface of electrodeposited Sn layer with thickness around 300 nm, which was potentiostatically lithiated at 50 mV.

Similar to the particle size effect on dealloying morphology evolution mentioned in our previous work [35], the thickness effect on bicontinuous porous morphology evolution in chronoamperometry was examined with free standing Sn sheets (thickness = 25 μm) and

electrodeposited Sn layers (thickness = 300 nm) on Cu as shown in Fig. 2.16. Bicontinuous porous morphologies were observed in delithiated Sn sheets with thickness of 25 μm (Fig. 2.16 A and B), while only Kirkendall voids and some nanopores near the Cu/Sn interface were shown in delithiated electrodeposited Sn layer with thickness of 300 nm (Fig. 2.16 C and D). The clear dealloying morphology differences between Sn sheets (25 μm) and Sn layers (300 nm) is analogous to behaviors observed on dealloying of Li-Sn microparticles [35] and noble-metal alloy nanoparticles [107], [108], where the dimension limit to produce bicontinuous porous morphology is 2-3 times of the ligament size (here means the bulk ligament size).

As shown in Fig. 2.16 A and B, the bicontinuous porous structures showed larger size ligament (~350 nm) near the surface and grain boundary/crack and smaller ligament size (~150 nm) in the bulk. The relatively larger ligament near the surface and grain boundary/crack might be formed by surface diffusion smoothening and ligament collapsing process. As all dealloying structures seen in the noble-metal alloy, bicontinuous porosity herein undergoes rapid coarsening/reconstruction by surface diffusion [105]. The mechanism of ligament coarsening and collapsing was speculated by Erlebacher [31] to be surface-diffusion-controlled solid-state Rayleigh instability based on large-scale kinetic Monte Carlo simulations. According to Rayleigh instability, materials would be pulled away from saddle-point curvature ligament, which leads to ligament pinch-off. The pinched off ligament will be consumed to enlarge others, which caused ligament collapsing. Comparing to ligament in bulk porosity, under-connected ligaments at surface/crack/grain boundary had larger surface energy and are more likely to collapse through repetition of ligament pinch-off and ligament reattachment/accumulation. The resulted surface larger ligament-bulk narrower ligament structure is favorable in fuel cell membrane [109].

As shown in Fig. 2.16 C and D, dealloyed Sn layer with thickness of 300 nm shows nanopure structures. Nanopores in Fig. 2.16 D are similar to encased voids inside ligament structures in dealloyed Ag-Au [110], where Rayleigh instability of pore channels was employed to explain the formation of encased voids [111]. Even though the morphology shown in Fig. 2.16 A and B proved the possibility to form bicontinuous porous structure under the same experiment conditions, no ligament of bicontinuous porous morphology was observed in the cross sections of dealloyed thin Sn layers. One possibility is that during the dealloying process of thin Sn layers with thickness of 300 nm, the favorable tendency of ligament collapsing near the electrode/electrolyte interface might have caused collapsing of preexisted bicontinuous porous structure and leaving only nanopores near the interface of Cu and Sn (Fig. 2.16 D). Different from nanopores in Fig. 2.16 D, those in Fig. 2.16 C were of smaller diameter and distributed throughout the whole cross section area. These smaller scale nanopores might be Kirkendall voids, which predict delithiation of in-ligament Li proceeded through diffusion-limited dealloying at high enough dealloying rate but below dealloying dimension limit.

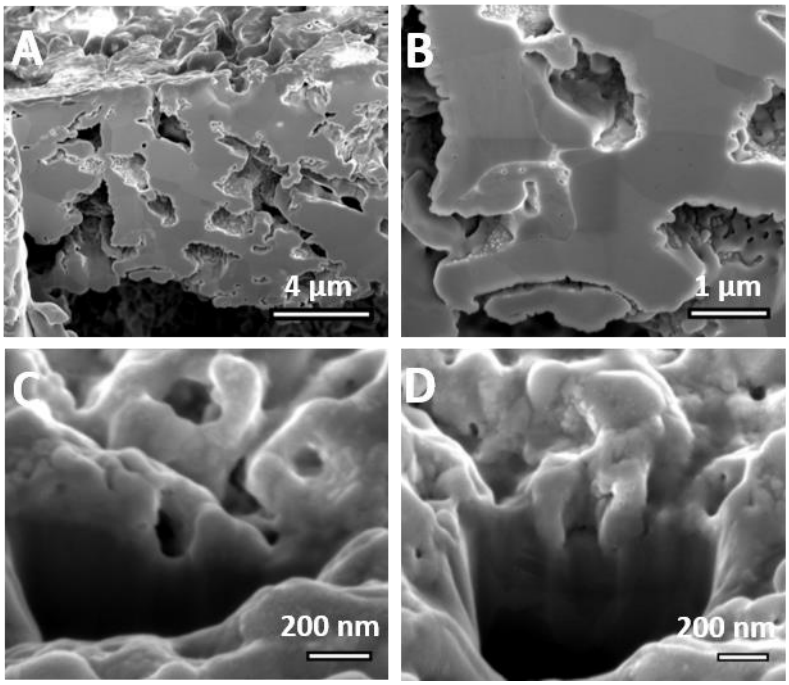

Figure 2.17. Galvanostatic dealloying (at current density ≤ 50 µA/cm^2) results of planar host LiSn/Li$_7$Sn$_3$ (potentiostatically lithiated at 400 mV) FIB milled cross-section views with different Sn layer thickness. A,B. Negative dendrites with Kirkendall voids along grain boundaries of free standing Sn sheets with thickness of 25 µm galvanostatic delithiated at current density of 40 µA/cm^2. **C,D**. Void nodules with Kirkendall voids structures of electrodeposited Sn with thickness ~300 nm galvanostatically delithiated at current density of 50 µA/cm^2.

To further investigate the dimension effect on dealloying morphology evolution, we also examined the effect of sheet thickness on negative dendrite and Kirkendall voids formation in chronopotentiometry (Fig. 2.17). Similarly, the diffusion-limited dealloying dimension limit was examined with free standing Sn sheets (thickness = 25 µm, Fig. 2.17 A and B) and electrodeposited Sn layers (thickness = 300 nm, Fig. 2.17 C and D). As shown in Fig. 2.17 A and B, negative dendrite and Kirkendall voids evolved when free standing Sn foils with thickness of 25 µm were dealloyed at current density of 40 µA/cm^2; void nodule/wedge and Kirkendall voids were produced when electrodeposited Sn layers with thickness of 300 nm were delithiated at current density of 50 µA/cm^2. All of these structures were typical morphology resulted from diffusion-limited dealloying, where the void nodule structures might be related to surface

smoothening or non-branched pre-negative dendrites. Thus, we concluded that there was no dimension limit observed for diffusion-limited dealloying.

CHAPTER 3

MORPHOLOGY EVOLUTION IN LI-PB SYSTEMS

3.1 Methods

Sample preparation: Pb foils (United Metal & Chemical Corp., 5N purity) were cold rolled to 0.0005'' (~12.7 μm) and shelf stored at room temperature for over three months before use. Li foils (thickness = 0.75 mm, 99.9%, Alfa Aesar) were used as received. The Pb particles with diameter of 1 μm were made following Dr. Younan Xia's procedure[112] with increased amount of lead acetate and decreased amount of poly(vinyl pyrrolidone) (PVP) as shown in Fig. 3.1. Lead acetate (0.94837 g) dissolved in 5 mL tetraethylene glycol (TEG) was added drop by drop into 20mL boiling TEG solution with PVP (0.1 g PVP/10 mL TEG) hosted in a 100 mL three-neck round bottom flask, which was kept in an inert environment with a continuous flow of Ar. The reaction mixture was kept under constant magnetic stirring for 15 min before quenched by cold ethanol (which had been cooled by dry ice). The black-brownish precipitates were harvested and cleaned by centrifuging with ethanol for three times. The product was air dried at room temperature overnight to remove the residual ethanol. Size of Pb micro-particles was confirmed by scanning electron microscopy (Nova 200 NanoLabUHRFEG system). The Pb particle with diameter of 5 or 15 μm was galvanostatically electrodeposited on well-polished Cu disks at a current density of 2.5 mA/cm^2 for duration of 250 or 600 s, respectively. The Cu disk, used as the working electrode, was mechanically polished sequentially to a mirror finish with #P800, #P1200, #P2400, #P4000 SiC abrasive paper and finally polished using 0.5 μm diamond suspension. One piece of Pb foil and one Pb wire was used as the counter and reference electrode, respectively. The aqueous electrolyte contained 0.1 mol/L $Pb(ClO_4)_2$ and 0.1 mol/L $HClO_4$. Size of the electrodeposited particles was checked using Nova 200.

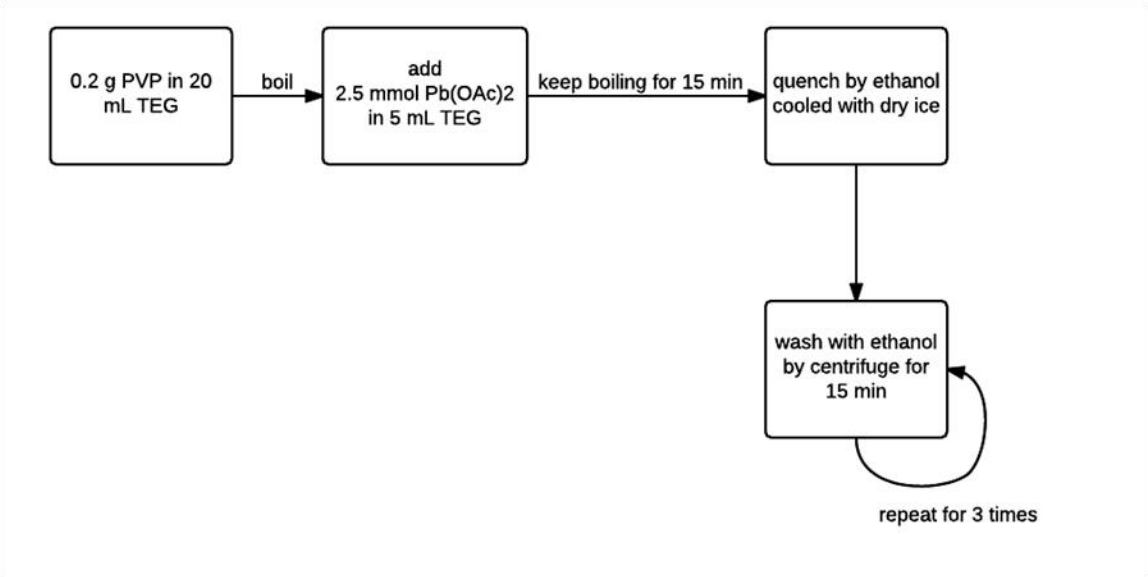

Figure 3.1. Schematic procedure for Pb particle manufacture. PVP: polyvinylpyrrolidone; TEG: tetraethylene glycol; $Pb(OAc)_2$: Lead(II) acetate.

GITT and PITT measurements: Pb layer with thickness of 500 nm vapor deposited on Cu foil was used as working electrode in GITT and PITT measurements. Thickness of Pb layers was checked by Stylus profilometer (Bruker Dektak XT). In order to minimize deformation of the Pb/Cu working electrode during lithiation and delithiation, the electrode was fixed to a piece of mica with Kapton tape leaving an exposed area of 0.25 cm^2. Two pieces of Li foils were used as the counter and reference electrode. A 3-neck round bottom flask containing 10 mL of 1 M $LiClO_4$ in polypropylene carbonate was used as the reservoir. Before GITT and PITT experiment, the working electrode was maintained at voltage of 1 V vs. Li^+/Li until the current density was smaller than 10 $\mu A/cm^2$. The GITT procedure consisted of pulses at a current density of 250 $\mu A/cm^2$ for 50 s, followed by a relaxation duration for 100 s. For the PITT measurements, potential steps of 10 mV were applied and the current was measured as a function of time. The potential was stepped to the 10 mV increment either when the current reached 10 $\mu A/cm^2$ or if time exceeded 5000 s.

Devanathan-Stachurski cell experiment: As described in the original work by Devanathan and Stachurski[73], the electrochemical cell consisted of two cylindrical glass compartments sealed at the bottom by two size 12 O-ring joints, between which a Pb foil with thickness of 0.0006" (15.2 μm) and active area of 0.1963 cm^2 (diameter of 5 mm) was sandwiched. The Pb foil served as shared working electrode for both compartments. Each compartment carried two pieces of Li foils serving as reference and counter electrodes. The cathodic side of the Pb foil was potentiostatically lithiated at voltage of 400 mV, while the anodic side of the Pb foil was maintained at a fixed voltage corresponding to the open circuit potential of Pb insuring that Li could be oxidized to Li^+. Both compartments were filled with 100 mL of 1 M $LiClO_4$ in polypropylene carbonate. Potentiostats connecting to both compartments were operated in floating mode.

Morphology Evolution: The lithiation-delithiation of Pb foils and Pb particles on Cu disks were conducted in a 3-neck round bottom flask cell containing 10 mL of 1 M $LiClO_4$ in polypropylene carbonate. Two pieces of Li foil was used as the counter and reference electrode. The Pb foil used had an active area of 0.25 cm^2 directly facing the counter Li foil. For the particulate host Pb with diameter of 1 μm, electrochemical experiments were performed with a two electrode pouch cell configuration. The working electrode composed of a mixture of Pb particles, Super-C45 carbon black (TIMCAL) and polyvinylidene fluoride (Sigma Aldrich) in a 5:3:2 weight ratio pre-dissolved in N-methyl-2-pyrrolidone (Sigma Aldrich). One piece of Li foil served as both the reference and counter electrode. The working electrode and Li foil was separated by a piece of glass fiber separator, which was soaked in the electrolyte of 1 M $LiPF_6$ in diethylene carbonate/ dimethylene carbonate/ethylene carbonate in a 2:1:2 ratio by volume (MTI corp.). These Pb particle working electrode, glass fiber separator and Li counter electrode were sealed into a

pouch cell under Ar. Potentiostatic lithiation and delithiation was performed by maintaining the working electrode at prescribed potential until the absolute current density is lower than 10 $\mu A/cm^2$. Galvanostatic delithiation was performed at different current densities between 0.4-2.5 V.

All electrochemical measurements and morphology evolution experiments were conducted inside an ultrahigh-purity argon-purged MBraun LABMaster glove box (H_2O and O2 < 0.1 ppm) using either a Gamry series-G or BioLogic SP-150 potentiostat. All potentials mentioned in this work were versus pure Li (vs. Li^+/Li).

Focused ion-beam milling and SEM: After delithiation, the Pb foil was immersed in acetonitrile for 5 s to remove part of the SEI layer and then transferred into the SEM chamber while sealed in Ar. The air exposure was less than 5 s when transferred into SEM chamber. SEM and focused ion-beam milling was conducted in a dual-beam Nova 200 NanoLabUHRFEG system at a 52˚ tilted angle.

3.2 Diffusion Measurements Of Li In Li-Pb Alloys By GITT, PITT And DS Measurements

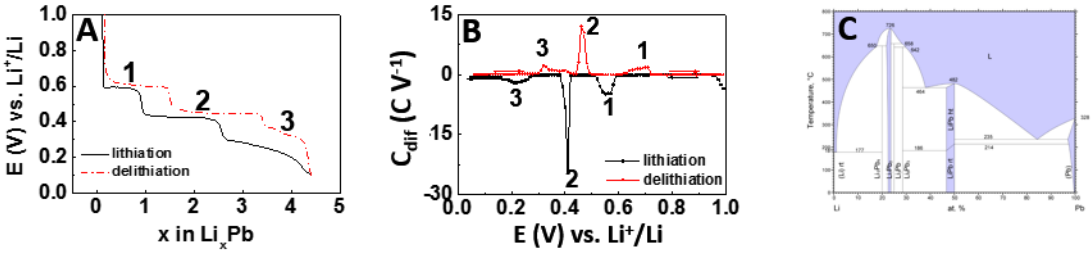

Figure 3.2. Relationship of phase transformation reactions with electrode potential obtained from PITT and GITT measurements. **A**. The quasi-equilibrium potential of Li-Pb alloys by GITT measurements on a 500 nm-thick Pb layer vacuum deposited on Cu foil. **B**. Differential capacitance as a function of potential by PITT measurement on a 500 nm-thick Pb layer vacuum deposited on Cu foil. **C**. The Li-Pb phase diagram.

Experimentally measured coulometric titration curves (quasi-equilibrium potential versus Li composition plot) and differential capacity plots together with phase diagrams are useful tools for understanding and presenting the correlation between working electrode potential and phase(s) preexisted and evolving at electrode surface. According to the Gibbs phase rule, under conditions of constant temperature and pressure, all intensive parameters (including activity or chemical potential) of the system are constants in a two phase coexistent region of Li-Pb alloy. While in a single-phase region, there is one independent intensive parameter. This rule is reflected in the coulometric titration curve obtained from GITT measurements with two types of behavior: 1, the quasi-equilibrium potential changes with the state of charge in the single-phase region; 2, constant activity or chemical potential corresponds to two-phase mixtures. Based on phase diagram of Li-Pb (Fig. 3.2C) [41], [70], [113], there are five possible intermetallic compounds existing at room temperature: LiPb, Li_8Pb_3, Li_3Pb, Li_7Pb_2 and $Li_{17}Pb_4$. Fig. 3.2A shows a plot of quasi-equilibrium potential as a function of alloy composition for 500 nm Pb layer vapor-deposited on Cu foil determined by GITT measurements in lithiation and delithiation direction. Clearly, not all of the intermetallic phases are accessible by electrochemical lithiation at ambient temperature. Taken the Li composition calculated from charge consumed in GITT lithiation measurements into consideration, plateaus labelled as 1, 2 and 3 in Fig. 3.2A were related to phase transformation reactions shown in eq. 23, eq. 24, and eq. 25, respectively. The differences in Li composition of single-phase regions between lithiation and delithiation directions are similar to the results in chronopotentiometry curves obtained by other researchers[46], [54]. These differences were caused by non-equilibrium conditions of the GITT measurements.

Fig. 3.2B shows potential dependence of the differential capacitance, C_{dif}, for lithiation and delithiation of 500 nm Pb layer vapor-deposited on Cu foil determined by PITT measurements. In analogous to peaks shown in a linear sweep voltammogram, peaks shown in a differential capacity curve also represent different surface reactions occurring in corresponding voltage range. Since the plateau potential of plateau 1, 2 and 3 in Fig. 3.2A are the same as the peak potential for peak 1, 2 and 3 in Fig. 3.2B, the differential capacitance wave 1, 2 and 3 are also related to phase transformation reactions shown in eq. 23, eq. 24, and eq. 25, respectively. Our phase assignment is in good agreement with Huggins' coulometric titration curve[49] and Sánchez's differential capacity curves[51], [52].

$$Pb + Li^+ + e^- \rightarrow LiPb \quad (23)$$

$$3LiPb + 5Li^+ + 5e^- \rightarrow Li_8Pb_3 \quad (24)$$

$$4Li_8Pb_3 + 19Li^+ + 19e^- \rightarrow 3Li_{17}Pb_4 \quad (25)$$

Similar to diffusion measurements of Li-Sn systems, the composition-dependent intrinsic diffusion coefficient, $\overline{D}_{Li}^{Pb}$, of Li in Li-Pb alloys was measured by GITT, PITT, and DS measurements. In this work, $\overline{D}_{Li}^{Pb}$ was calculated from GITT, PITT and DS measurements using eq. 6, 12 and 19, respectively. Since lithiation of Pb sheets at voltage of 50 mV had high propensity of volume expansion, cracking and fracture, DS measurements were conducted at cathodic polarization voltage of 400 mV with 15.2 μm thick Pb sheets. According to the Linear sweep voltammogram of Pb sheets (Fig.3.3), Pb dissolution takes place at voltage ~2.75 V. The anodic polarization was kept at open circuit potential of Pb sheets (~2.6 V) in order to rapidly oxidize any atomic Li reached the anodic side of the DS cell but not causing localized attack. Volume expansion and phase transitions of Pb sheets during dealloying were not taken under consideration when calculating the diffusion coefficients of Li in Li-Pb alloy.

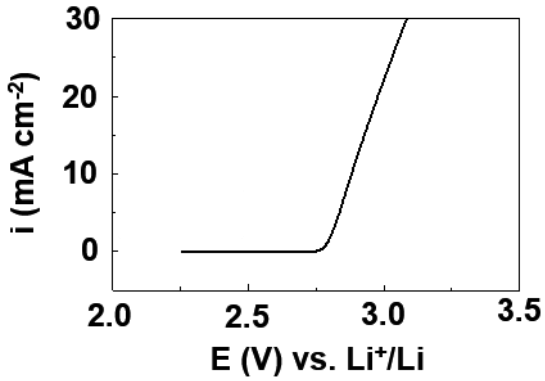

Figure 3.3. Linear sweep voltammetry of a Pb sheet with thickness of 25.4 µm in 1 M $LiClO_4$ in propylene carbonate. Sweep rate of 10 mV/s.

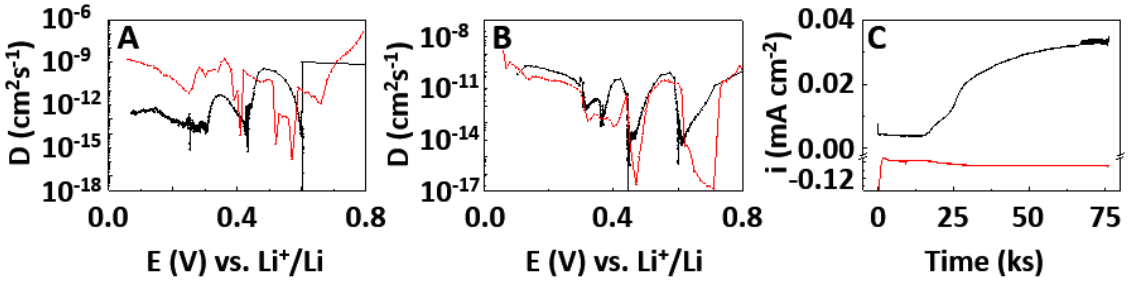

Figure 3.4. Results of PITT, GITT and DS measurements of Li diffusivity in Pb at ambient temperature. $\bar{D}_{Li}^{Pb}$ as a function of E obtained from GITT (black) and PITT (red) measurements in the (**A**) lithiation and (**B**) delithiation direction. **C.** DS measurement for a 15.2 µm-thick Pb sheet showing current on the cathodic side (red) and anodic side (black).

The results for $\bar{D}_{Li}^{Pb}$, as a function of potential, E, obtained at ambient temperature from GITT and PITT measurements in the short time approximation for the lithiation and delithiation directions are compared in Fig.3.4A and B. Similar to results of Li-Sn systems, large dips in diffusion coefficients were found in the phase transformation regions since the current was consumed by both new phase formation and Li diffusion (PIIT) or because the electrochemical potential is constant in the two-phase co-existence regions (GITT). Since the diffusion coefficients in the phase transformation regions are inaccurate, only those in the single-phase regions are taken into consideration hereafter. Table 3.1 shows that the calculated values of

$\bar{D}_{Li}^{Pb}$ from PITT and GITT measurements for lithiation and delithiation were in reasonable agreement. The differences in $\bar{D}_{Li}^{Pb}$ determined from PITT and GITT measurements were less than a factor of 1000 and 10 in the lithiation and delithiation direction, respectively. Li diffusion coefficient of order 10^{-8}-10^{-9} was observed in the FCC Pb phase in lithiation direction. These higher diffusion coefficients might be caused by the fast kinetics of SEI formation at initial lithiation stage. Considering both the GITT and PITT measurement results in Li-Pb alloy phases, the diffusion coefficients are of order 10^{-13} - 10^{-10} cm^2s^{-1} in the lithiation direction and 10^{-12} - 10^{-10} cm^{2-1} in the delithiation direction. One typical current response of Devanathan-Stachurski cell measurements is shown in Fig.3.4 C. The $\bar{D}_{Li}^{Pb}$ obtained from DS measurement was 1.36×10^{-11} cm^2s^{-1}, which is in good agreement with the GITT and PITT results.

At ambient temperature, and at lithiation voltage of 50 mV, it requires ~128 hours to fully lithiate the 12.7 μm-thick Pb sheet and using a simple $x^2 \sim \bar{D}_{Li} t$ estimate for $\bar{D}_{Li}$ yields an average compositional value of the intrinsic Li diffusivity ~5 x 10^{-12} cm^2s^{-1}. The DS time-of-flight measurement for $\bar{D}_{Li}$ is also a compositionally averaged number that yielded 1.36 x 10^{-11} cm^2s^{-1}, which is in reasonable agreement with our simple estimate. Both of these numbers are also in reasonable agreement with both the GITT and PITT values.

Table 3.1. Summarize of $\bar{D}_{Li}^{Pb}$ (cm^2/s) calculated from GITT and PITT measurements in corresponding single-phase regions.

phase	**GITT**		**PITT**	
	lithiation	delithiation	lithiation	delithiation
Pb	1.1×10^{-9}	6.5×10^{-11}	~1.5×10^{-8}	2.2×10^{-10}
LiPb	2.3×10^{-10}	8.3×10^{-11}	8.8×10^{-11}	3.0×10^{-11}
Li_8Pb_3	5.2×10^{-12}	3.3×10^{-11}	2.6×10^{-10}	4.5×10^{-12}
$Li_{17}Pb_4$	5.7×10^{-13}	1.2×10^{-10}	9.5×10^{-10}	3.6×10^{-11}

3.3 Composition Dependence Of Dealloying Morphology Evolution:Planar Li-Pb Sheets

Parent-phase alloy composition is one of those key features controlling dealloyed morphology. For low homologous temperature dealloying (like in Ag-Au alloys), there exists a lower Ag composition bound, the parting limit, below which dealloy does not occur. In the Li-Sn system (one case of high homologous temperature dealloying), bicontinuous porous morphology from percolation dissolution can only evolve when Li composition is equal to or higher than 70 at. %. In order to understand the effect of Li composition on dealloying morphology evolution of Li-Pb alloys, Pb sheets with thickness of 12.7 μm charged to varying Li concentrations were dealloyed potentiostatically or galvanostatically after which FIB cross-sections were examined. According to the correlation between potential and the Li-Pb phases shown in Fig.3.5 A, potentiostatic lithiation of LiPb, Li_8Pb_3 and $Li_{17}Pb_4$ was performed at potentials of 500 mV, 400 mV and 50 mV, respectively. Li-Pb alloys were then dealloyed in chronoamperometry at constant voltage higher than the highest Li-Pb alloy equilibrium potential (0.6 V) and lower than Pb dissolution potential (2.75 V) or in chronopotentiometry at high current densities/dealloying rates (10 or 40 mA/cm^2).

Fig.3.5B-D shows results for Li-Pb alloys potentiostatically dealloyed at 2 V (C) or 2.5 V (B and D). For Pb sheets with Li concentrations ~81 at. % (highest accessible Li concentration in Li-Pb alloys with phase $Li_{17}Pb_4$), localized bicontinuous porosity and Kirkendall voids with width ~2-3 μm are evident. We believe this is a result of two phases being present at the 81 at. % Li composition. Some Kirkendall voids have a hexagon shape, while others do not hinting that there may have been several phases present. At concentrations of the order of 73 at.% Li, Kirkendall voids with size ~0.5-1 μm are present. The disconnected holes holes parallel to the surface shows that the dealloyed morphology was Kirkendall voids and not bicontinuous porosity. Both

Fig.3.5C and D show that Kirkendall voids were larger near the Pb surface and smaller in the bulk. While Kirkendall voids were only seen near the surface for Pb sheets with Li concentration ~50at.%. Also, a trend of larger Kirkendall voids and higher void volume to solid material ratio with higher staring Li concentration of Li-Pb alloy was observed. The decreasing size and population of voids results from smaller quantities of Li being removed as the effective dealloying potential is decreasing.

Fig.3.5 E-G shows that the dealloyed morphology of Pb sheets changes from negative dendrites to bicontinuous porosity as the Li concentration of Li-Pb alloy increases from ~50at.% to ~73 at.% in galvanostatic delithiation. As shown in Fig.3.5F and G, for Li concentrations larger than ~73 at.%, a bicontinuous morphology similar to that of nanoporous gold and Sn evolves with dealloying current density higher than 10 mA/cm^2. Close inspection of Fig.3.5F and G shows that the length scales of porosity in delithiated Li_8Pb_3 and $Li_{17}Pb_4$ are ~35 nm and ~60 nm, respectively. The difference in the ligament size is a result of the difference in starting composition of the alloy. Dealloyed Pb sheets containing ~50 at.% Li showed negative dendrites resulting from diffusion-limited dealloying. As shown in Fig.3.5 F, at current density of 10 mA/cm^2, the dealloying potential was high enough to dissolve Li from highly coordinated terrace sites. Thus, the differences in morphology apparent by comparison of Fig.3.5E and F are results of the differences in starting composition of the alloy. Our results demonstrate that the threshold composition for percolation dissolution to happen is ~73 at.% Li in Li-Pb alloy which likely corresponds to the Li_8Pb_3 phase.

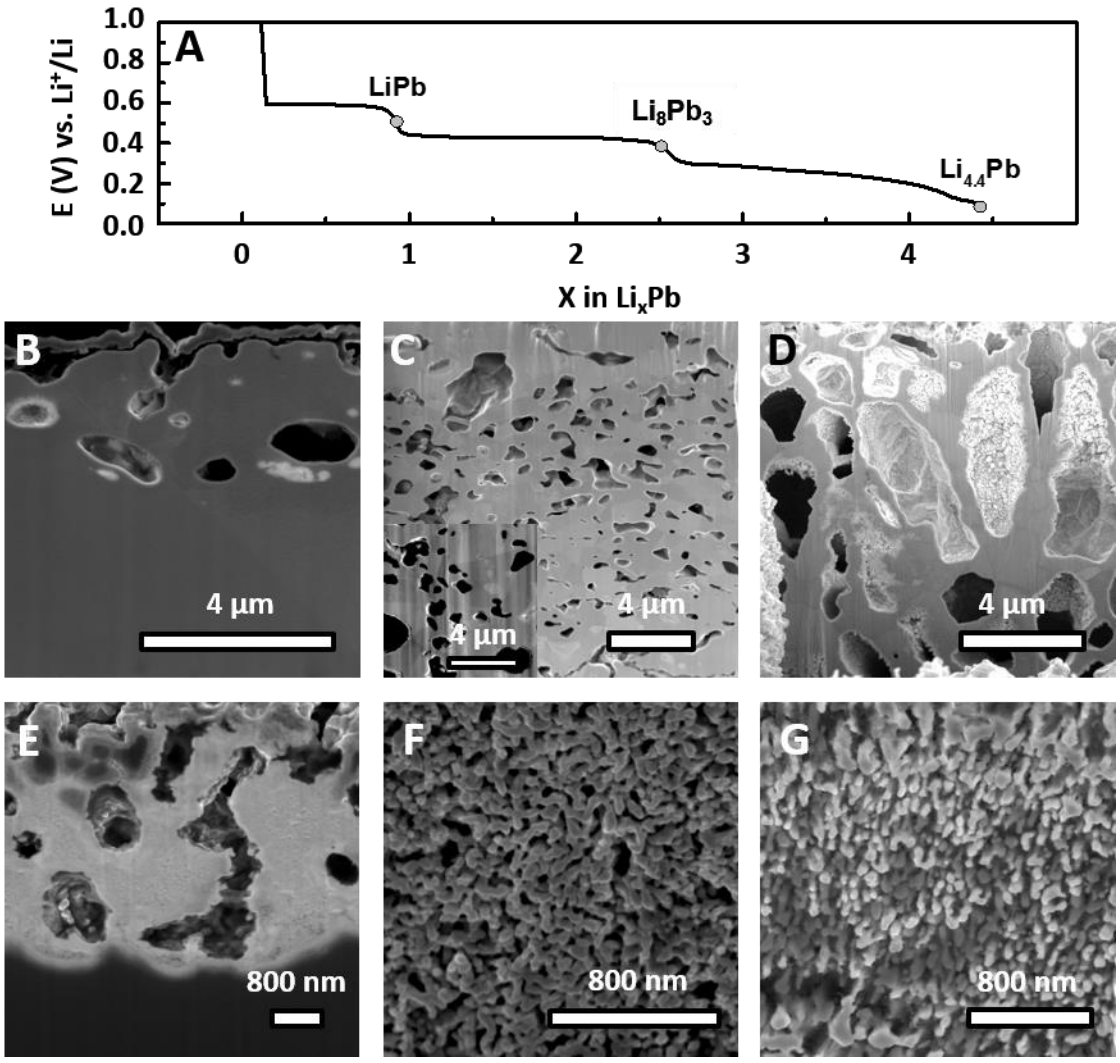

Figure 3.5. The effect of alloy composition on morphology evolution in potentiostatic and galvanostatic dealloying. A. The quasi-equilibrium potential as a function of alloy composition obtained from GITT for a vapor-deposited 500 nm-thick Pb layer on Cu in the lithiation direction at ambient temperature. **B-D.** Cross-section views showing Kirkendall voids obtained from potentiostatic dealloying of (**B)** LiPb at 2 V, (**C**) Li_8Pb_3 at 2.5 V, and (**D**) $Li_{17}Pb_4$ at 2 V. Inset in image C shows a surface view of Kirkendall voids. **E-G.** Cross-section views of delithiation morphologies obtained by galvanostatic dealloying. **E.** LiPb at 10 mA/cm^2 showing negative dendrites. **F.** Li_8Pb_3 at 10 mA/cm^2 bicontinuous porosity and **G.** $Li_{17}Pb_4$ at 40 mA/cm^2 both showing bicontinuous porosity.

3.4 Effect Of Dealloying Rate On Morphology Evolution In Chronopotentiometry: Planar Host Li-Pb Alloy Sheets

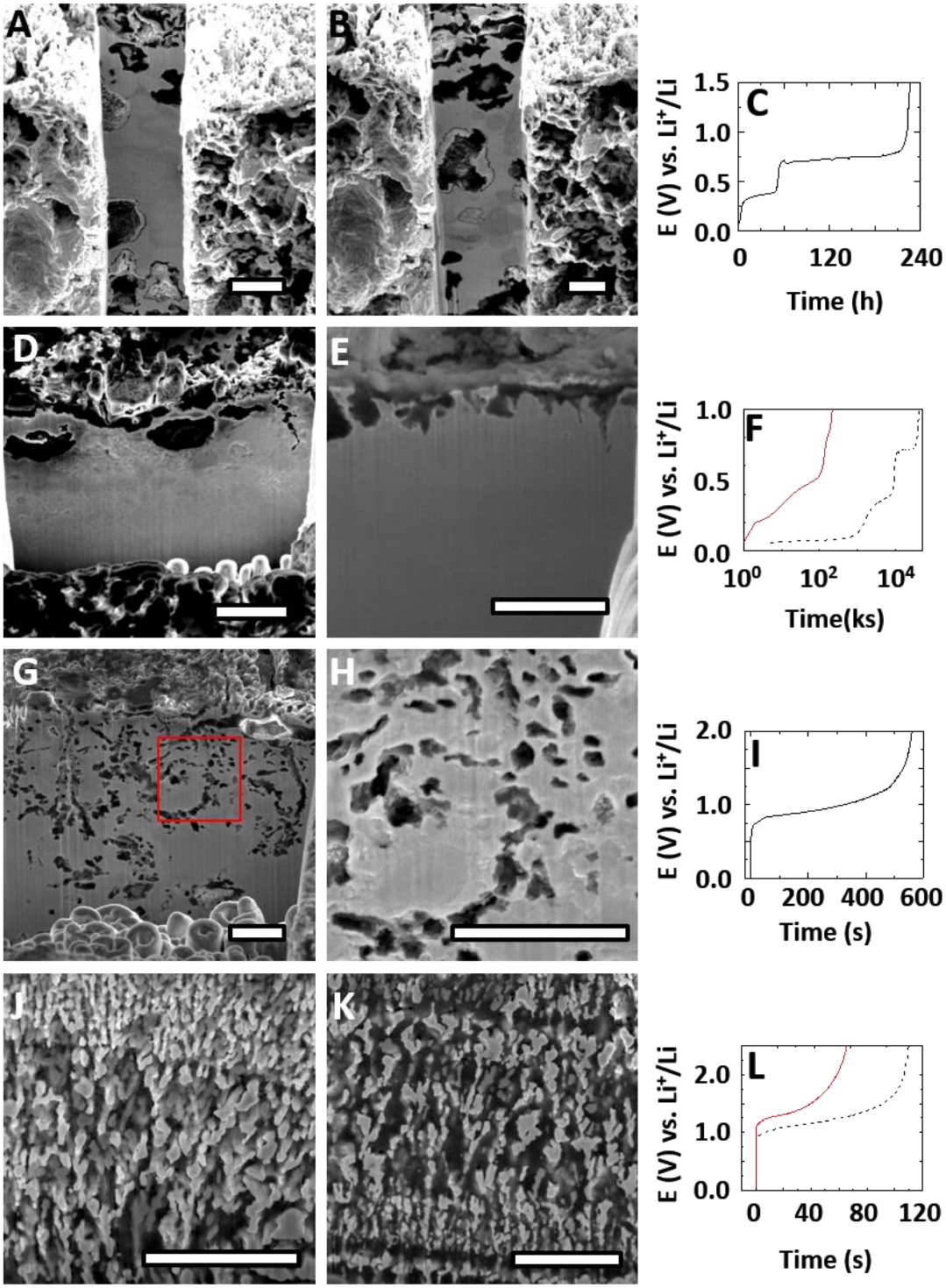

Figure 3.6. Effect of dealloying rate on morphology evolution and corresponding chronopotentiometry for 12.7 μm-thick Pb sheets lithiated at a voltage of 50 mV to the $Li_{17}Pb_4$ composition followed by galvanostatic delithiation. A-C. Delithiation at 5 μA/cm^2 showing Kirkendall voids. **D,** Delithiation at 50 μA/cm^2 (black curve in **F**) and **E,** 500 μA/cm^2

(red curve in **F**) showing negative dendrites and void nodules. **G-I.** Delithiation at 10 mA/cm^2 showing Kirkendall voids. Image I shows a magnified view of the highlighted region G. **J**-**K**, Delithiation at 40 mA/cm^2 (black curve in **L**) and **K**, 80 mA/cm^2 (red curve in **L**) showing bicontinuous porosity. All scale bars are 2 μm.

There are also effects on the dealloyed morphology connected to the dealloying rate or dealloying current density in galvanostatic delithiation. Here, polycrystalline planar host LiPb system was investigated by performing galvanostatic dealloying of $Li_{17}Pb_4$ at different current densities: 5 μA/cm^2, 50 μA/cm^2, 500 μA/cm^2, 10 mA/cm^2, 40 mA/cm^2 and 80 mA/cm^2. Dealloyed morphologies and corresponding voltage profiles are shown in Fig. 3.6. As shown in Fig. 3.6A and B, the FIB cross-sections depict large Kirkendall voids at a current density of 5 μA/cm^2. In contrast, potentiostatic delithiation resulted Kirkendall voids of diameter ~4 μm located both near the electrolyte/electrode interface and well in to the interior of the sheet. When dealloying was performed at current densities of 50 and 500 μA/cm^2, negative dendrite and void nodule structures were observed near the electrolyte/electrode interface (Fig. 3.6D and E). None of those void nodules and negative dendrites were interconnected, which is consistent with an important contribution of solid-state mass transport to dealloying. An interesting morphology was formed when dealloying was carried out at current density of 10 mA/cm^2. Fig. 3.6 G and H show isolated holes similar to Kirkendall voids around the negative dendrite morphology. At dealloying current densities of 40 mA/cm^2 and 80 mA/cm^2, bicontinuous porous morphologies resulting from percolation dissolution form (Fig. 3.6J and K). For larger dealloying rates, the bicontinuous structures have smaller ligament size.

In contrast to the titration result during lithiation shown in Fig. 3.5A, only two phase transformation plateaus were shown in delithiation voltage profile at dealloying current density as low as 5 μA/cm^2, 50 μA/cm^2 and 500 μA/cm^2 (Fig. 3.6C and F). Total charge consumed by

phase transformation at voltage of 745 mV is three times for a voltage of 375 mV. Taking GITT results (Fig. 3.5A) and other researchers' results [44], [49], [51]–[53] into consideration, the plateau at voltage of 375 mV and 745 mV were associated to phase transformation reactions between $Li_{17}Pb_4$ and Li_8Pb_3 (eq. 25) and between Li_8Pb_3 and Pb (eq. 24). No plateaus below 1 V were observed in chronopotentiometry at current densities of 40 mA/cm^2 and 80 mA/cm^2, which indicated that during delithiation no phase transformation reactions occured. By comparing the chronopotentiometry curves (Fig. 3.6C, F, I and L) with the corresponding morphologies (Fig. 3.6A, B, D, E, G, H, J, K), it is safe to draw the conclusion that both of the two phase transformation reactions shown in eq. 24 and eq. 25 are related to the solid-state mass transport processes, which results in the Kirkendall voids, negative dendrite and void nodule structures. When the imposed dealloying rate is so fast, such that no phase transformation reactions occur at the alloy/electrolyte interface, bicontinuous porous morphologies form (Fig. 3.6J and K). The voltage profile of percolation dissolution dominated delithiation (Fig. 3.6L) can be divided into three stages: stage 1, voltage jump in several seconds due to IR drop; stage 2, a pseudo voltage plateau at voltage around 1 V; and stage 3, corresponding to the voltage jump to over 2 V. Based on the charge percentage of each stage, we can expect the formation of bicontinuous porous structures within stage 2, while stage 3 may be associated with dealloying of residual Li within the ligaments of the porous structure.

3.5 Effect Of Dealloying Rate On Morphology Evolution In Chronopotentiometry: Particulate Host Li-Pb

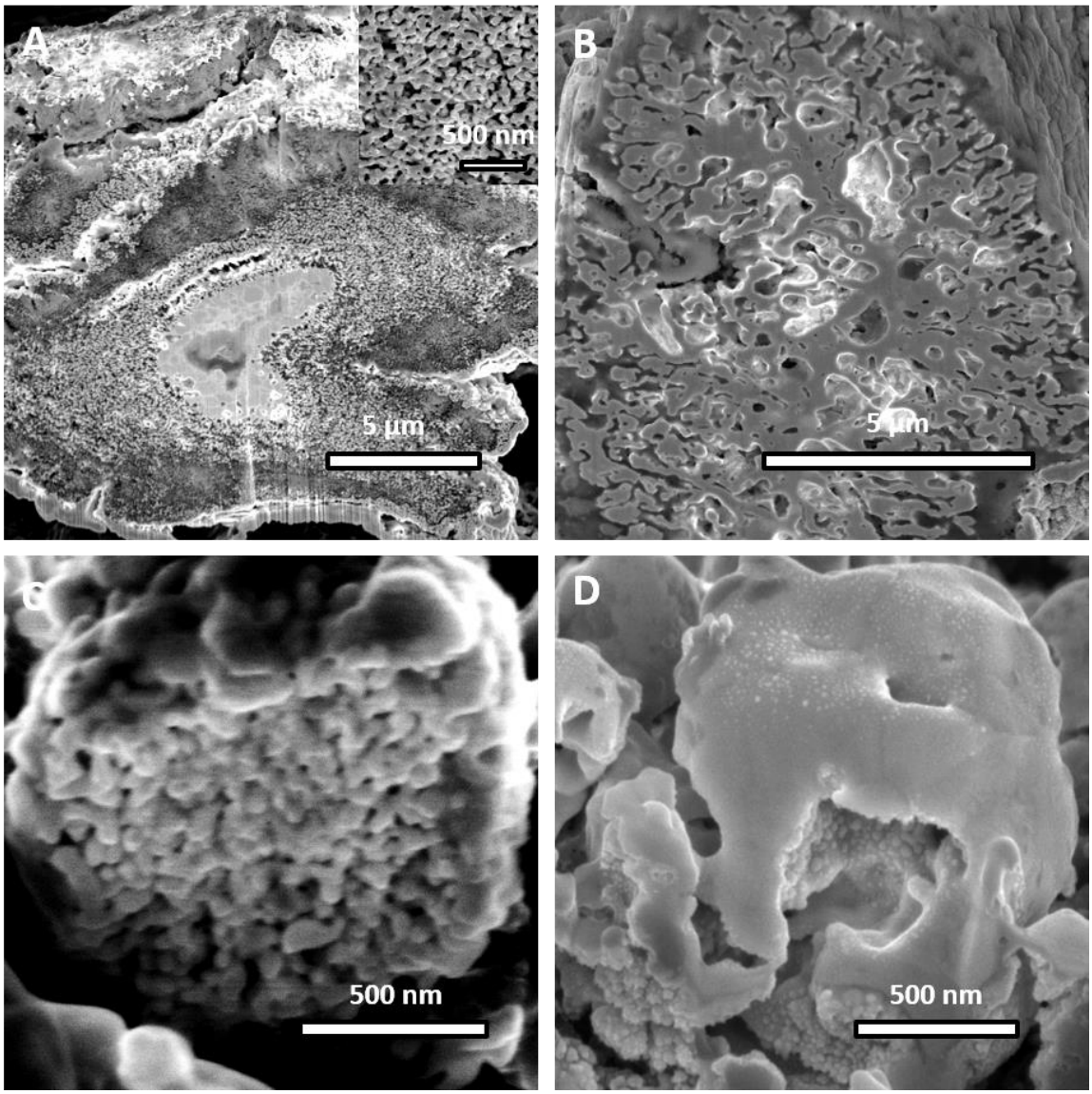

Figure 3.7. FIB cross-sections and corresponding chronopotentiometry of Pb particles potentiostatically lithiated at 50 mV followed by galvanostatic dealloying at indicated C rates. **A.** 60 C; solid core and a bicontinuous porous shell in a ~15 µm diameter particle. Inset shows magnified view. **B.** 18/5 C; negative dendrite and void nodules in a ~15 µm diameter particle. **C.** 15 C; bicontinuous porosity in a ~1 µm diameter particle. **D.** 9/5 C; negative dendrite and void nodules in a ~1 µm diameter particle.

The effect of dealloying rate on morphology evolution in chronopotentiometry in particulate host LiPb systems was also investigated by conducting galvanostatic dealloying of the alloy $Li_{17}Pb_4$ at different C rates. $Li_{17}Pb_4$ particles were fabricated by potentiostatic lithiation at voltage of 50

mV until the current density was lower than 10 μA/cm^2. Delithiated cross-section morphologies of Pb particle with diameter of 15 μm and 1 μm are summarized in Fig. 3.7. In analogy to dealloying rate effect on dealloying morphology evolution of Li-Pb planar host system, percolation dissolution tends to dominate the dealloying mechanism at high dealloying rates. As shown in Fig. 3.7A and C, at comparably higher dealloying rate (60 C for 15 μm particles and 15 C for 1 μm particles), dealloying produced bicontinuous porous morphologies. While dealloying yields negative dendrite structures evidenced Li diffusion for relatively lower dealloying rate (18/5 C for 15 μm particles and 9/5 C for 1 μm particles). Close inspection of Fig. 3.7A inset and C shows that ligament sizes are different in Pb particles with different sizes. For both size Pb particles, Li-Pb alloy starting composition was kept at $Li_{17}Pb_4$. The average ligament size of delithiated 15 μm Pb particles was ~70 nm. However, for 1 μm Pb particles, the average ligament size was ~35 nm. The reason for different length scale of ligament size is presently unclear, however, we suspect that this may be a result of iR effects within the pores of the larger particles.

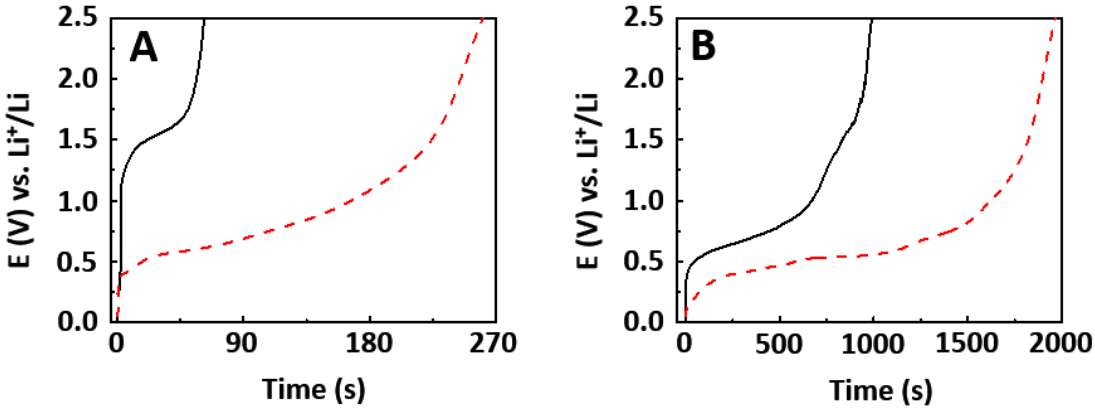

Figure 3.8. Chronopotentiometry delithiation profiles as a function of Pb particle size and C-rate. A. Voltage profile corresponding to bicontinuous porosity; 15 μm particle size at 60 C (black solid curve) and 1 μm particle size at 15 C (red dashed curve). **B.** Voltage profile

corresponding to negative dendrites and void nodule formation, 15 μm particle size at 18/5 C (black solid curve) and 1 μm particle size at 9/5 C (red dashed curve).

The corresponding chronopotentiometry results for Pb particle delithiated at the indicated rates are shown in Fig. 3.8. Similar to the results for Pb sheets, no Li-Pb alloy phase transformation plateaus were evident in the voltage profile when bicontinuous porous structures evolve (Fig. 3.8A). The voltage profile corresponding to negative dendrite and nodule structures (Fig. 3.8B) showed one 'plateau' at voltage ~530 mV. This plateau corresponds to delithiation phase transformation reactions occurring at lower voltages causing the Li concentration to drop below the composition limit for percolation dissolution. Consequently as the voltage increases Li dealloying from terrace sites becomes feasible resulting in negative dendrite structures.

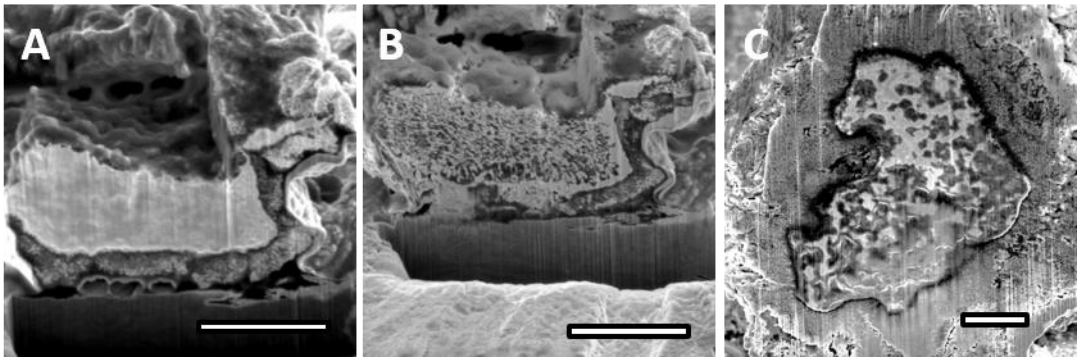

Figure 3.9. FIB cross-sections of Pb particle (lithiated at 50 mV) followed by galvanostatic dealloying at indicated C rates. A. 14 C, solid core bicontinuous porous shell morphology of as dealloyed Pb particle. **B**. 14 C, bicontinuous porous morphologies of the same Pb particle shown in (**A**). **C**. 60 C, solid core bicontinuous porous shell morphology of as dealloyed Pb particle with lithiation duration of 168 h. All scale bars are 4 μm.

One can see that some delithiated 15 μm particles show a solid core-bicontinuous porous shell structure. The composition of this solid core may correspond to a Li-Pb alloy, which was not fully delithiated. In order to check the composition of the solid core, two sets of experiments were performed. In one set, the lithiation duration was extended from 48 h to 168 h and then

galvanostatically delithiated at rate of 60 C. The resulting cross-section still showed the solid core-bicontinuous porous shell morphology (Fig. 3.9C). While negative dendrite and void nodule structures penetrating throughout the whole delithiated Pb particle was observed in Fig. 3.7B. Thus, we believe that the likelihood of solid core being pure non-lithiated Pb is very low. In order to prove that the solid core is not delithiated, FIB cross-section of one Pb particle as delithiated and after being shelf stored for one week was compared in Fig. 3.9A and B. As shown in Fig. 3.9A, 15 μm Pb particle as delithiated depicts solid core bicontinuous porous morphology, while after being shelf stored for 7 days, the same Pb particle showed bicontinuous porous structures with two distinct regions (Fig. 3.9B). The solid core region in Fig. 3.9A evolved into a new bicontinuous porous region in Fig. 3.9B. Note that the top half of Pb particle shown in Fig. 3.9A and B was damaged by ion beam before generating the FIB cross-sections. Thus, no bicontinuous shell region was shown in the top part of Pb particle in Fig. 3.9A. Considering the results from both of these two sets of experiment, the solid core in Fig. 3.9A and Fig. 3.7A was proved to be related a lack of Li within the core of the particle. It seems likely that the formation of solid core bicontinuous shell structure is connected to IR drop effects occurring inside the porous region of the bicontinuous porous structure. As dealloying proceeds, the IR effects increase with increasing thickness of bicontinuous porous shell. The real potential applied at dealloying front is the applied potential minus this generated IR drop. Bicontinuous porosity only evolves above certain dealloying potential threshold. When bicontinuous porous shell thickness is larger than a certain threshold value, the effective dealloying potential at dealloying front would be smaller than the dealloying critical potential. In consequence, dealloying would then proceed through diffusion-limited dealloying.

3.6 Size Effects On Morphology Evolution In Chronoamperometry

In order to understand the effect of particle size on morphology evolution, potentiostatic dealloying of $Li_{17}Pb_4$ was studied with Li-Pb particulate and planar hosts. Potentiostatic lithiation was carried out at voltage of 50 mV until the absolute current density was less than 10 $\mu A/cm^2$ for all Pb host systems examined in this part of the study. The fully lithiated $Li_{17}Pb_4$ was then potentiostatically delithiated at potentials larger than the equilibrium potential of the LiPb phase (0.6 V) and lower than Pb dissolution potential (2.75 V). As shown in Fig. 3.10A, FIB cross-section of delithiated of 1 μm Pb particles evolve a bicontinuous porous morphology. However, no bicontinuous porosity evolved in Pb particles of diameter 15 μm or Pb sheets with thickness of 12.7 μm when dealloying was performed at even higher potential (2 V). FIB cross-section of delithiated 15 μm Pb particle shows negative dendrite structures oriented towards the interface between the Pb particle and the Cu substrate (Fig. 3.10B). Formation of negative dendrite proves that potentiostatic dealloying in 15 μm Pb particle was a diffusion-limited process with dealloying potential large enough to generate surface vacancies. As shown in Fig. 3.10C, large Kirkendall voids were observed in delithiated planar host $Li_{4.4}Pb$ systems following potentiostatic delithiation at voltage of 2 V.

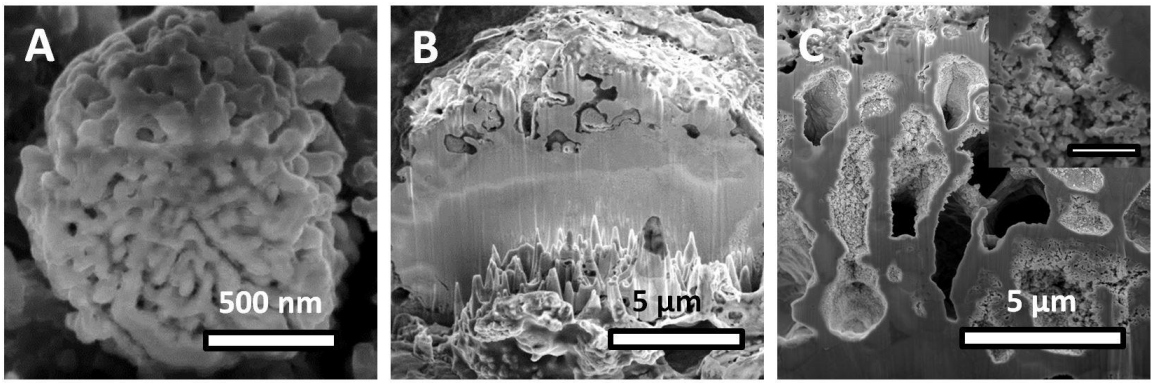

Figure 3.10. Size-effects on dealloyed morphology in the potentiostatic delithiation of Pb particles and sheets lithiated to 5o mV corresponding to $Li_{17}Pb_4$. A. 1 μm diameter Pb particle delithiated at 1 V showing bicontinuous porosity. **B**. 15 μm diameter Pb particle delithiated at 2 V showing negative dendrites. **C**. 25 μm-thick Pb sheet delithiated at 2 V showing negative dendrites and regions of bicontinuous porosity (inset shows bicontinuous porosity with scale bar of 1 μm).

As shown in Fig. 3.10, dealloying morphology changed from bicontinuous porosity (A), to negative dendrite (B) and finally to Kirkendall voids (C) as Pb host size decreased. This phenomenon could be caused by the fact that the effective dealloying potential at dealloying front and the apparent Li diffusion coefficient varies with the Pb host dimension owing to the iR effects previously discussed. For 12.7 μm thick Pb foils, the effective potential might be lower than the threshold potential for new surface area generation and thus, only Kirkendall voids structures were observed in Fig. 3.10C. On the other hand, apparent diffusion coefficient of Li in Li-Pb alloys was related to size of Pb hosts. Grain size of the original Pb hosts was around 2 μm. Grain boundaries were only observed in the FIB cross-sections of larger Pb hosts (12.7 μm Pb sheets and 15 μm Pb particles). For 1 μm Pb particles, diffusion can only proceed through lattice diffusion, which is not fast enough to homogenize the Li composition during dealloying. Thus, bicontinuous porous morphology would form following percolation dissolution. While in larger Pb hosts (12.7 μm Pb sheets and 15 μm Pb particles), both lattice diffusion and grain boundary diffusion can occur. Therefore, the apparent diffusion might be fast enough to homogenize Li composition during dealloying. Thus, negative dendrite and Kirkendall void structures could form.

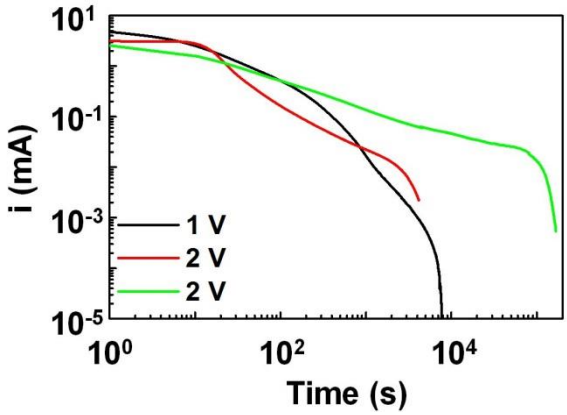

Figure 3.11. Chronoamperometry during potentiostatic delithiation of different Pb hosts lithiated to 50 mV to $Li_{17}Pb_4$. black line, Pb particles with diameters of 1 μm delithiated at 1 V; red line, Pb particles with diameters of 15 μm delithiated at 2 V; green line, Pb sheets with thickness of 12.5 μm delithiated at 2 V.

Fig. 3.11 shows the log-log plot of current-time response at fixed potential corresponding to the morphologies shown in Fig. 3.11. Chronoamperometry of Pb foil with thickness of 12.7 μm displays an approximate $t^{-1/2}$ decay, which is a mark of a diffusion controlled process [114]. The time dependence current corresponding to Pb particle with diameter of 15 μm maintained at a constant value ~3 mA for ~10 s until it began a steep decay following t^{-1} behavior. A similar ~ t^{-1} time dependence was observed in Li-Sn system when Sn sheets were delithiated at voltage of 600 mV (below the critical potential for bicontinuous porosity formation). No power law behavior was obeserved for Pb particle with diameter of 1 μm, which is in good agreement with the percolation dissolution resulted bicontinuous porous morphology. For the first 10 s dealloying current response of these three hosts, it is obvious that the dealloying rate decreases as the host dimension increases. Quanlitatively taking the host dimension and Pb particle coverage ratio into consideration, the current density for the Pb particle delithiation was at least of the order of 100 times larger than that of Pb sheets. One possible explanation for the dependence of dealloying rate on host dimension is that the IR drop near Pb surface increases significantly with increasing Pb host size. Thus, the effective dealloying potential at dealloying front for Pb sheets was so low that only low coordinated kink site Li atoms could be dissolved and resulted in no new surface area generation. The effective dealloying potential of 15 μm Pb particle was apparently large enough to generate new surface area by removing highly coordinated terrace site Li atoms but not high enough to support fast dealloying rate for bicontinuous porosity evolution. While percolation dissolution can only happen in 1 μm Pb particles, whose effective potential was higher than the critical potential for percolation dissolution.

CHAPTER 4

DEALLOYING MORPHOLOGY DIAGRAMS

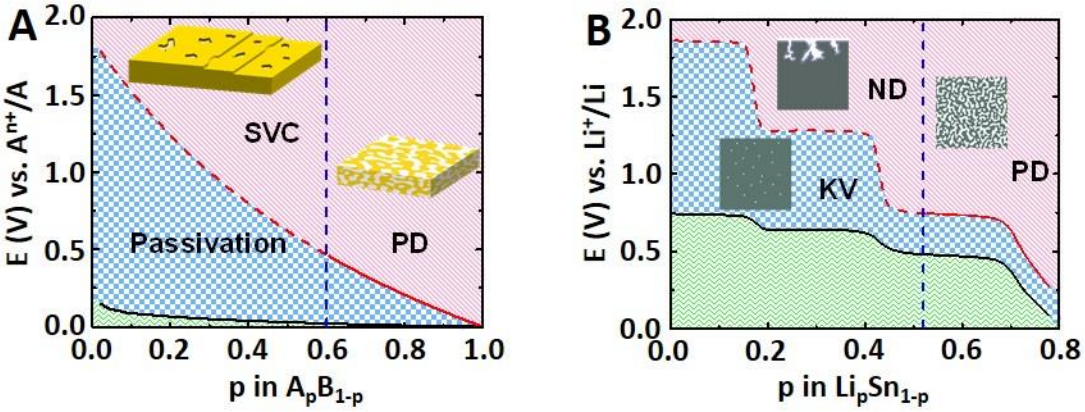

Figure 4.1. Dealloying morphology diagrams. A. Left panel shows the behavior noble metal alloys such as Ag-Au at ambient temperature. **B.** The right panel shows the ambient temperature behavior of Li-Sn alloys. In each of these diagrams the black curve is the metal/metal-ion equilibrium potential of the less-noble component in the alloy and the red curve is the composition –dependent critical potential. In the left panel the dotted blue vertical line corresponds to the dealloying threshold while in the right panel the line corresponds to the threshold composition for percolation dissolution, p_{PD}. In these diagrams the abbreviations PD, SVC ND, and KV respectively represent percolation dissolution, surface vacancy clusters, negative dendrites and Kirkendall voiding.

A useful way to facilitate a discussion of our results is by constructing dealloying morphology diagrams. Fig. 4.1 shows a generic diagram displaying the morphology evolution behavior expected at low T_H of a A_pB_{1-p} alloy (p is the mole fraction of component A) which forms a continuous series of solid solutions and where the A component is selectively dissolved. The behavior of Ag-Au alloys at ambient temperature is the prototypical example of this. The black –colored curve is the equilibrium potential of the more electroactive component and the red-colored curve shows the composition dependent thermodynamic critical potential, V_{crit}. The dashed blue vertical line at $p = p^*$ corresponds to the dealloying threshold or parting limit for the alloy, below which it is not possible to selectively dissolve the more reactive component. The

only mechanism for dealloying the sample throughout its volume is percolation dissolution. In order for this to occur the potential needs to be large enough to result in vacancy cluster injection into terrace surface sites. The approximate size, χ, of the mean diameter of the injected clusters is $(1+p)a/(1-p)$ where a is the nearest neighbor spacing in the alloy. During this process the mean composition at the interface between the dealloyed and the un-dealloyed parent phase is virtually identical to the original alloy composition. For potentials larger than V_{crit}, the sample will form a bicontinuous structure similar to NPG. At lower potentials and for compositions above p^*, surface dealloying occurs and dissolution of A-atoms proceeds in a layer-by-layer process from low-coordinated kink sites at surface steps without the creation of new surface area. Owing to surface step fluctuations, A-atoms in terrace sites eventually find their way to kink sites from which they dissolve. Eventually, this leads to a surface highly enriched in the B component and passivation. Another mechanism for surface passivation occurs at compositions below p^* and potentials higher than V_{crit} for which surface dealloying occurs by a vacancy injection mechanism. A-atoms clusters larger than the mean cluster size, χ, are dissolved (forming surface vacancy clusters) and consequently dissolution is limited to finite penetrations since such large A atom-clusters do not percolate through the solid. As discussed below, for high T_H, dissolution within this potential-composition regime results in the evolution of negative dendrite morphologies.

Morphology evolution on dealloying at low T_H of a 2-phase (α or β) microstructure depends on the volume fraction of the phases as well as their composition. Suppose the α-phase is rich enough in the A component to allow for percolation dissolution at a sufficiently high potential, while the β-phase composition does not. In order for dealloying of the α-phase to occur

throughout the sample volume it is clear that this phase must percolate through the solid. If this is the case then the dealloyed α-phase morphology will resemble that which occurs in a single-phase system, however, the bi-continuous morphology resulting from percolation dissolution will be spatially confined to regions previously occupied by the α-phase domains. During dealloying the β-phase will be essentially passive. A more interesting situation can arise in two-phase systems if the composition of both phases allows for percolation dissolution. At a sufficiently high potential bi-continuous porosity would evolve in each of the phases although the length scales (e.g., mean ligament diameter) of the porous structures would be different owing to compositional effects. Since the spatial distribution of these dealloyed morphologies should correlate with the initial microstructure of the original phases, a multitude of dealloyed bi-continuous microstructures could evolve.

Fig. 4.1B illustrates the dealloying morphology diagram we constructed for the Li-Sn system. The black curve is the equilibrium potential of Li in the alloy referenced to the activity of Li in the electrolyte. The flat regions of this curve correspond to two-phase co-existence regions for which the activity of Li is the same in each phase. We estimated the critical potential in the single-phases, Li_2Sn_5, LiSn and Li_xSn ($x \geq 2.33$) from the equation,

$$V_{crit}\left(p\right) = V_{equil}\left(p\right) + \frac{4\gamma_{Sn}\Omega_{Li}}{F}\frac{\left(1-p\right)}{\left(1+p\right)}a \qquad (26)$$

where, γ_{Sn} ~ 0.6 Jm^{-2}, is the Sn/electrolyte interfacial free energy, Ω_{Li} ~1.5 x 10^{-5} m^3, is the molar volume of Li in the alloy, *F* is Faraday's constant and *a* is the nearest neighbor distance in the structure. We note that, as discussed earlier, the Li titration charge/discharge behavior for Li_xSn ($x \geq 2.33$) is single-phase like and this is the composition range connected to percolation

dissolution. The solid red-colored curve is the compositionally dependent thermodynamic critical potential for bi-continuous porosity formation. This curve has been extended into the region of negative dendrite formation since surface vacancies have to be produced for this morphology to evolve. The large differences in composition among Li_2Sn_5, LiSn and Li_7Sn_3 resulted in large differences in the corresponding V_{crit} values that were spliced together in a manner paralleling the Li^+/Li equilibrium potential. The vertical red-colored dashed line at ~ 0.52 mole fraction Li corresponds to a percolation dissolution threshold, p_{PD}. The percolation dissolution regime is similar to that in Fig. 4.1A and is cut-off at a compositional threshold, p_{PD}, which does not represent a conventional parting limit for the alloy. For Li compositions lower than p_{PD} and below the dashed extension of the critical potential curve, de-lithiation is supported by solid-state mass transport since the dealloying potential is too low to result in vacancy injection. Clearly, p_{PD} does not correspond to a parting limit since de-lithiation below this composition occurs. Another key difference between Fig. 4.1A and B is that there is no passivation region in Fig. 4.1B. At compositions below p_{PD} and above the compositionally dependent critical potential curve there is a morphology region that we have termed negative or void dendrites that form by vacancy injection resulting from dissolution of atoms from terrace sites. In this region dealloying is rate-limited by the solid-state mass-transport of Li and the evolution of this morphology is isomorphic to dendrite formation in electrodeposition. Between the critical potential and the equilibrium potential curves we observe Kirkendall voids. Within this region the electrochemical potential is too low to allow for dissolution of Li from highly coordinated surface terrace sites and so no significant increase in the area of the solid/electrolyte interface occurs. In a two-phase coexistence region such as Li_2Sn_5/LiSn, morphology evolution will depend on the volume fraction of the phases. In this case there is an additional morphology can evolve in addition to

Kirkendall voiding. Assume the volume fraction of the parent phases are such that the LiSn phase is in the form of non-percolating "island" domains within a sea of Li_2Sn_5. For this situation dissolution of Li from LiSn would result in sinusoidal-like surface roughness with a mean wavelength and amplitude corresponding respectively to the mean separation and diameter of the Li_2Sn_5 domains.

CHAPTER 5

CONCLUSION

Titration measurements and a time-of-flight technique were used measure the compositionally dependent Li intrinsic coefficient in Li-Sn, $\overline{D}_{Li}^{Sn}$, and Li-Pb, $\overline{D}_{Li}^{Pb}$, system. At ambient temperature, $\overline{D}_{Li}^{Sn}$, in the lithiation and delithiation direction is $10^{-13} - 10^{-12}$ cm^2s^{-1} and 10^{-12} to 10^{-8} cm^2s^{-1}, respectively. $\overline{D}_{Li}^{Pb}$ at ambient temperature was in the range of 10^{-13} cm^2s^{-1} to 10^{-8} and 10^{-12} to 10^{-10} cm^2s^{-1} in the lithiation and delithiation direction, respectively. The Devanathan Stachurski cell yielded a diffusion coefficient of 1.7×10^{-11} cm^2s^{-1} and 1.4×10^{-11} cm^2s^{-1} for Li-Sn and Li-Pb, respectively. Over the temperature range of 30-140 °C, we found the activation energies for Li diffusion in the phases Li_2Sn_5, LiSn and Li_7Sn_3 to be respectively 37.4, 37.8 and 22.5 kJ/mole.

We described the various dealloyed morphologies that can form in the Li-Sn and Li-Pb systems and showed how dealloying rate, potential, phase transformation reaction and host size affect the dealloying morphology evolution. For alloy systems displaying a significant solid-state mobility or at high T_H there is no parting limit for dealloying, however, there is a compositional threshold (p_{PD}) as well as a critical potential (E_{crit}) for the operation of percolation dissolution and the formation of bi-continuous structures. In planar host Li-Sn systems, p_{PD} was defined to be ~52 at.% Li. While in planar Li-Pb systems, p_{PD} was found to be ~73 at.% Li and ~ 81 at.% Li in chronopotentiometry and chronoamperometry, respectively. E_{crit} was ~ 550 mV and ~ 2V for Li-Sn and Li-Pb systems, respectively. Negative or void dendrite morphologies evolve at compositions below p_{PD} and at large values of the applied electrochemical potential. Kirkendall voiding morphologies evolve below the critical potential over the entire range of alloy compositions. The dealloying mechanism gradually evolved from percolation dissolution

dominated to diffusion–limited dominated dealloying as dealloying rate decreases and dealloying potential decreases. The sample-size limit for the percolation dissolution is 3-4 times the ligament diameter. In particulate hosts for Li-Pb, a bicontinuous shell solid core morphology evolves when particle diameter was larger than 5 μm.

REFERENCES

[1] J. Snyder, T. Fujita, M. W. Chen, and J. Erlebacher, "Oxygen reduction in nanoporous metal–ionic liquid composite electrocatalysts," *Nat. Mater.*, vol. 9, no. 11, pp. 904–907, 2010.

[2] V. R. Stamenkovic, B. S. Mun, K. J. J. Mayrhofer, P. N. Ross, and N. M. Markovic, "Effect of surface composition on electronic structure, stability, and electrocatalytic properties of Pt-transition metal alloys: Pt-skin versus Pt-skeleton surfaces," *J. Am. Chem. Soc.*, vol. 128, no. 27, pp. 8813–8819, 2006.

[3] V. R. Stamenkovic *et al.*, "Trends in electrocatalysis on extended and nanoscale Pt-bimetallic alloy surfaces," *Nat. Mater.*, vol. 6, no. 3, pp. 241–247, 2007.

[4] J. W. Choi, J. McDonough, S. Jeong, J. S. Yoo, C. K. Chan, and Y. Cui, "Stepwise nanopore evolution in one-dimensional nanostructures," *Nano Lett.*, vol. 10, no. 4, pp. 1409–1413, 2010.

[5] K. Wang and J. Weissmüller, "Composites of nanoporous gold and polymer," *Adv. Mater.*, vol. 25, no. 9, pp. 1280–1284, 2013.

[6] K. Wang, A. Kobler, C. Kübel, H. Jelitto, G. Schneider, and J. Weissmüller, "Nanoporous-gold-based composites: toward tensile ductility," *NPG Asia Mater.*, vol. 7, no. 6, p. e187, 2015.

[7] K. Wang, C. Hartig, M. Blankenburg, M. Müller, R. Günther, and J. Weissmüller, "Local flow stresses in interpenetrating-phase composites based on nanoporous gold—In situ diffraction," *Scr. Mater.*, vol. 127, pp. 151–155, 2017.

[8] K. Hu, D. Lan, X. Li, and S. Zhang, "Electrochemical DNA biosensor based on nanoporous gold electrode and multifunctional encoded DNA− Au bio bar codes," *Anal. Chem.*, vol. 80, no. 23, pp. 9124–9130, 2008.

[9] Z. Matharu, P. Daggumati, L. Wang, T. S. Dorofeeva, Z. Li, and E. Seker, "Nanoporous Gold-Based Electrode Morphology Libraries for Investigating Structure-Property Relationships in Nucleic Acid-Based Electrochemical Biosensors," *ACS Appl. Mater. Interfaces*, 2017.

[10] C. A. R. Chapman, L. Wang, H. Chen, J. Garrison, P. J. Lein, and E. Seker, "Nanoporous

Gold Biointerfaces: Modifying Nanostructure to Control Neural Cell Coverage and Enhance Electrophysiological Recording Performance," *Adv. Funct. Mater.*, 2016.

[11] W.-C. Shih, G. M. Santos, F. Zhao, O. Zenasni, and M. M. P. Arnob, "Simultaneous Chemical and Refractive Index Sensing in the 1–2.5 μm Near-Infrared Wavelength Range on Nanoporous Gold Disks," *Nano Lett.*, vol. 16, no. 7, pp. 4641–4647, 2016.

[12] J. Biener *et al.*, "Surface-chemistry-driven actuation in nanoporous gold," *Nat. Mater.*, vol. 8, no. 1, pp. 47–51, 2009.

[13] C. Cheng, J. Weissmüller, and A. H. W. Ngan, "Fast and Reversible Actuation of Metallic Muscles Composed of Nickel Nanowire-Forest," *Adv. Mater.*, vol. 28, no. 26, pp. 5315–5321, 2016.

[14] H. Jin and J. Weissmüller, "Bulk nanoporous metal for actuation," *Adv. Eng. Mater.*, vol. 12, no. 8, pp. 714–723, 2010.

[15] H.-J. Jin, X.-L. Wang, S. Parida, K. Wang, M. Seo, and J. Weissmüller, "Nanoporous Au−Pt alloys as large strain electrochemical actuators," *Nano Lett.*, vol. 10, no. 1, pp. 187–194, 2009.

[16] P. Poizot, S. Laruelle, S. Grugeon, L. Dupont, and J. M. Tarascon, "Nano-sized transition-metal oxides as negative-electrode materials for lithium-ion batteries," *Nature*, vol. 407, no. 6803, pp. 496–499, 2000.

[17] J. Erlebacher, M. J. Aziz, A. Karma, N. Dimitrov, and K. Sieradzki, "Evolution of nanoporosity in dealloying," *Nature*, vol. 410, no. 6827, pp. 450–453, 2001.

[18] J. D. Fritz and H. W. Pickering, "Selective Anodic Dissolution of Cu-Au Alloys: TEM and Current Transient Study," *J. Electrochem. Soc.*, vol. 138, no. 11, pp. 3209–3218, 1991.

[19] D. V Pugh, A. Dursun, and S. G. Corcoran, "Electrochemical and morphological characterization of Pt–Cu dealloying," *J. Electrochem. Soc.*, vol. 152, no. 11, pp. B455–B459, 2005.

[20] K. Sieradzki, R. R. Corderman, K. Shukla, and R. C. Newman, "Computer simulations of corrosion: selective dissolution of binary alloys," *Philos. Mag. A*, vol. 59, no. 4, pp. 713–746, 1989.

[21] J. W. Essam, “Percolation theory,” *Reports Prog. Phys.*, vol. 43, no. 7, p. 833, 1980.

[22] K. Wagner, S. R. Brankovic, N. Dimitrov, and K. Sieradzki, “Dealloying below the critical potential,” *J. Electrochem. Soc.*, vol. 144, no. 10, pp. 3545–3555, 1997.

[23] K. Sieradzki, “Curvature effects in alloy dissolution,” *J. Electrochem. Soc.*, vol. 140, no. 10, pp. 2868–2872, 1993.

[24] J. Rugolo, J. Erlebacher, and K. Sieradzki, “Length scales in alloy dissolution and measurement of absolute interfacial free energy,” *Nat. Mater.*, vol. 5, no. 12, pp. 946–949, 2006.

[25] K. Sieradzki, N. Dimitrov, D. Movrin, C. McCall, N. Vasiljevic, and J. Erlebacher, “The dealloying critical potential,” *J. Electrochem. Soc.*, vol. 149, no. 8, pp. B370–B377, 2002.

[26] S. M. Makin, A. H. Rowe, and A. D. LeClaire, “Self-diffusion in gold,” *Proc. Phys. Soc. Sect. B*, vol. 70, no. 6, p. 545, 1957.

[27] B. Okkerse, “Self-diffusion of gold,” *Phys. Rev.*, vol. 103, no. 5, p. 1246, 1956.

[28] C. T. Tomizuka and E. Sonder, “Self-diffusion in silver,” *Phys. Rev.*, vol. 103, no. 5, p. 1182, 1956.

[29] J. D. Harrison and C. Wagner, “The attack of solid alloys by liquid metals and salt melts,” *Acta Metall.*, vol. 7, no. 11, pp. 722–735, 1959.

[30] H. Kaiser, “Selective dissolution of high and low diffusivity alloys—A comparison of kinetical and micromorphological aspects,” *Corros. Sci.*, vol. 34, no. 4, pp. 683–699, 1993.

[31] J. Erlebacher, “Mechanism of coarsening and bubble formation in high-genus nanoporous metals,” *Phys. Rev. Lett.*, vol. 106, no. 22, p. 225504, 2011.

[32] X. H. Liu, S. Huang, S. T. Picraux, J. Li, T. Zhu, and J. Y. Huang, “Reversible nanopore formation in Ge nanowires during lithiation–delithiation cycling: An in situ transmission electron microscopy study,” *Nano Lett.*, vol. 11, no. 9, pp. 3991–3997, 2011.

[33] S.-C. Chao, Y.-F. Song, C.-C. Wang, H.-S. Sheu, H.-C. Wu, and N.-L. Wu, “Study on

microstructural deformation of working Sn and SnSb anode particles for Li-ion batteries by in situ transmission X-ray microscopy," *J. Phys. Chem. C*, vol. 115, no. 44, pp. 22040–22047, 2011.

[34] Q. Chen and K. Sieradzki, "Mechanisms and morphology evolution in dealloying," *J. Electrochem. Soc.*, vol. 160, no. 6, pp. C226–C231, 2013.

[35] Q. Chen and K. Sieradzki, "Spontaneous evolution of bicontinuous nanostructures in dealloyed Li-based systems," *Nat. Mater.*, vol. 12, no. 12, pp. 1102–1106, 2013.

[36] Y. S. Fung and D. R. Zhu, "Electrodeposited tin coating as negative electrode material for lithium-ion battery in room temperature molten salt," *J. Electrochem. Soc.*, vol. 149, no. 3, pp. A319–A324, 2002.

[37] J. L. Tirado, "Inorganic materials for the negative electrode of lithium-ion batteries: state-of-the-art and future prospects," *Mater. Sci. Eng. R Reports*, vol. 40, no. 3, pp. 103–136, 2003.

[38] I. Kim, G. E. Blomgren, and P. N. Kumta, "Sn/C composite anodes for Li-ion batteries," *Electrochem. solid-state Lett.*, vol. 7, no. 3, pp. A44–A48, 2004.

[39] J. Hassoun, S. Panero, P. Reale, and B. Scrosati, "A new type of lithium-ion battery based on tin electroplated negative electrodes," *Int. J. Electrochem. Sci*, vol. 1, no. 3, pp. 110–121, 2006.

[40] J. Sangster and C. W. Bale, "The li-sn (lithium-tin) system," *J. phase equilibria*, vol. 19, no. 1, pp. 70–75, 1998.

[41] H. Okamoto, "Li-Pb (lithium-lead)," *J. phase equilibria*, vol. 14, no. 6, p. 770, 1993.

[42] W.-J. Zhang, "A review of the electrochemical performance of alloy anodes for lithium-ion batteries," *J. Power Sources*, vol. 196, no. 1, pp. 13–24, 2011.

[43] T. Landoldt-Börnstein, "Structure data of elements and intermetallic phases," *Vol. 6Springer, Berlin*, 1971.

[44] R. A. Huggins, "Lithium alloy negative electrodes," *J. Power Sources*, vol. 81, pp. 13–19,

1999.

[45] J. Wang, I. D. Raistrick, and R. A. Huggins, “Behavior of Some Binary Lithium Alloys as Negative Electrodes in Organic Solvent-Based Electrolytes,” *J. Electrochem. Soc.*, vol. 133, no. 3, pp. 457–460, 1986.

[46] I. A. Courtney, J. S. Tse, O. Mao, J. Hafner, and J. R. Dahn, “Ab initio calculation of the lithium-tin voltage profile,” *Phys. Rev. B*, vol. 58, no. 23, p. 15583, 1998.

[47] M. Winter and J. O. Besenhard, “Electrochemical lithiation of tin and tin-based intermetallics and composites,” *Electrochim. Acta*, vol. 45, no. 1, pp. 31–50, 1999.

[48] I. A. Courtney and J. R. Dahn, “Electrochemical and in situ X-ray diffraction studies of the reaction of lithium with tin oxide composites,” *J. Electrochem. Soc.*, vol. 144, no. 6, pp. 2045–2052, 1997.

[49] J. Wang, P. King, and R. A. Huggins, “Investigations of binary lithium-zinc, lithium-cadmium and lithium-lead alloys as negative electrodes in organic solvent-based electrolyte,” *Solid State Ionics*, vol. 20, no. 3, pp. 185–189, 1986.

[50] R. A. Huggins, “Lithium alloy negative electrodes formed from convertible oxides,” *Solid State Ionics*, vol. 113, pp. 57–67, 1998.

[51] M. Martos *et al.*, “Electrochemical properties of lead oxide films obtained by spray pyrolysis as negative electrodes for lithium secondary batteries,” *Electrochim. Acta*, vol. 46, no. 19, pp. 2939–2948, 2001.

[52] M. Martos, J. Morales, and L. Sanchez, “Lead-based systems as suitable anode materials for Li-ion batteries,” *Electrochim. Acta*, vol. 48, no. 6, pp. 615–621, 2003.

[53] Q. Pan, Z. Wang, J. Liu, G. Yin, and M. Gu, “PbO@ C core–shell nanocomposites as an anode material of lithium-ion batteries,” *Electrochem. commun.*, vol. 11, no. 4, pp. 917–920, 2009.

[54] K. J. Rhodes, R. Meisner, M. Kirkham, N. Dudney, and C. Daniel, “In situ XRD of thin film tin electrodes for lithium ion batteries,” *J. Electrochem. Soc.*, vol. 159, no. 3, pp. A294–A299, 2012.

[55] L. Y. Beaulieu, S. D. Beattie, T. D. Hatchard, and J. R. Dahn, "The electrochemical reaction of lithium with tin studied by in situ AFM," *J. Electrochem. Soc.*, vol. 150, no. 4, pp. A419–A424, 2003.

[56] J. R. Dahn, I. A. Courtney, and O. Mao, "Short-range Sn ordering and crystal structure of Li 4.4 Sn prepared by ambient temperature electrochemical methods," *Solid State Ionics*, vol. 111, no. 3, pp. 289–294, 1998.

[57] D. A. Hansen and L. J. Chang, "Crystal structure of Li2Sn5," *Acta Crystallogr. Sect. B Struct. Crystallogr. Cryst. Chem.*, vol. 25, no. 11, pp. 2392–2395, 1969.

[58] W. Müller and H. Schäfer, "Die Kristallstruktur der Phase LiSn," *Zeitschrift für Naturforsch. B*, vol. 28, no. 5–6, pp. 246–248, 1973.

[59] W. Müller, "Darstellung und Struktur der Phase Li7Sn3/Preparation und Crystal Structure of Li7Sn3," *Zeitschrift für Naturforsch. B*, vol. 29, no. 5–6, pp. 304–311, 1974.

[60] U. Frank, W. Müller, and H. Schäfer, "Die Struktur der Phase Li5Sn2/The Crystal Structure of Li5Sn2," *Zeitschrift für Naturforsch. B*, vol. 30, no. 1–2, pp. 1–5, 1975.

[61] U. Frank and W. Müller, "Darstellung und Struktur der Phase Li13Sn5 und die strukturelle Verwandtschaft der Phasen in den Systemen Li-Sn und Li-Pb/The Preparation and Crystal Structure of Li13Sn5 and the Structural Relations Between the Phases of the Systems Li-Sn and Li-Pb," *Zeitschrift für Naturforsch. B*, vol. 30, no. 5–6, pp. 316–322, 1975.

[62] U. Frank, W. Müller, and H. Schäfer, "Die Kristallstruktur der Phase Li7Sn2/The Crystal Structure of Li7Sn2," *Zeitschrift für Naturforsch. B*, vol. 30, no. 1–2, pp. 6–9, 1975.

[63] H. P. Klug, "A.Redetermination of the Lattice Constant of Lead," *J. Am. Chem. Soc.*, vol. 68, no. 8, pp. 1493–1494, Aug. 1946.

[64] A. Zalkin and W. J. Ramsey, "Intermetallic Compounds between Lithium and Lead. III. The β1-β Transition in LiPb," *J. Phys. Chem.*, vol. 61, no. 10, pp. 1413–1415, 1957.

[65] A. Zalkin, W. J. Ramsey, and D. H. Templeton, "Intermetallic Compounds between Lithium and Lead. II. The Crystal Structure of Li8Pb3.," *J. Phys. Chem.*, vol. 60, no. 9, pp. 1275–1277, 1956.

[66] A. Zalkin and W. J. Ramsey, “Intermetallic Compounds between Lithium and Lead. I. The Structures of Li3Pb and Li7Pb2.,” *J. Phys. Chem.*, vol. 60, no. 2, pp. 234–236, 1956.

[67] G. R. Goward, N. J. Taylor, D. C. S. Souza, and L. F. Nazar, “The true crystal structure of Li 17 M 4 (M= Ge, Sn, Pb)–revised from Li 22 M 5,” *J. Alloys Compd.*, vol. 329, no. 1, pp. 82–91, 2001.

[68] H. Perlitz and E. Aruja, “V. A redetermination of the crystal structure of lithium,” *London, Edinburgh, Dublin Philos. Mag. J. Sci.*, vol. 30, no. 198, pp. 55–63, 1940.

[69] R. A. Dunlap, D. A. Small, D. D. MacNeil, M. N. Obrovac, and J. R. Dahn, “A Mössbauer effect investigation of the Li–Sn system,” *J. Alloys Compd.*, vol. 289, no. 1, pp. 135–142, 1999.

[70] A. Zalkin and W. J. Ramsey, “Intermetallic Compounds between Lithium and Lead. IV. The Crystal Structure of Li 22 Pb 5,” *J. Phys. Chem.*, vol. 62, no. 6, 1958.

[71] W. Weppner, “Determination of the Kinetic Parameters of Mixed-Conducting Electrodes and Application to the System Li[sub 3]Sb,” *J. Electrochem. Soc.*, vol. 124, no. 10, p. 1569, 1977.

[72] C. J. Wen, “Thermodynamic and Mass Transport Properties of ‘LiAl,’” *J. Electrochem. Soc.*, vol. 126, p. 2258, 1979.

[73] M. A. V Devanathan and Z. Stachurski, “The adsorption and diffusion of electrolytic hydrogen in palladium,” in *Proceedings of the Royal Society of London A: Mathematical, Physical and Engineering Sciences*, 1962, vol. 270, no. 1340, pp. 90–102.

[74] Y. C. Chu and H. Y. Yin, “Hydrogen Diffusivity in Pure Aluminum by Using Electrochemical Hydrogen Permeation Technique,” in *Key Engineering Materials*, 1988, vol. 20, pp. 2379–2387.

[75] M. Kurkela and R. M. Latanision, “The effect of plastic deformation on the transport of hydrogen in nickel,” *Scr. Metall.*, vol. 13, no. 10, pp. 927–932, 1979.

[76] M. J. Danielson, “Use of the Devanathan–Stachurski cell to measure hydrogen permeation in aluminum alloys,” *Corros. Sci.*, vol. 44, no. 4, pp. 829–840, 2002.

[77] R. M. Latanision and M. Kurkela, “Hydrogen permeability and diffusivity in nickel and Ni-base alloys,” *Corrosion*, vol. 39, no. 5, pp. 174–181, 1983.

[78] A. Turnbull, M. W. Carroll, and D. H. Ferriss, “Analysis of hydrogen diffusion and trapping in a 13% chromium martensitic stainless steel,” *Acta Metall.*, vol. 37, no. 7, pp. 2039–2046, 1989.

[79] Y. F. Cheng, “Analysis of electrochemical hydrogen permeation through X-65 pipeline steel and its implications on pipeline stress corrosion cracking,” *Int. J. Hydrogen Energy*, vol. 32, no. 9, pp. 1269–1276, 2007.

[80] E. Pollak, I. T. Lucas, and R. Kostecki, “A study of lithium transport in aluminum membranes,” *Electrochem. commun.*, vol. 12, no. 2, pp. 198–201, 2010.

[81] K. Persson *et al.*, “Lithium diffusion in graphitic carbon,” *J. Phys. Chem. Lett.*, vol. 1, no. 8, pp. 1176–1180, 2010.

[82] N. Boes and H. Züchner, “Electrochemical methods for studying diffusion, permeation and solubility of hydrogen in metals,” *J. Less Common Met.*, vol. 49, pp. 223–240, 1976.

[83] R. M. Barrer and E. K. Rideal, “Permeation, diffusion and solution of gases in organic polymers,” *Trans. Faraday Soc.*, vol. 35, pp. 628–643, 1939.

[84] H. A. Daynes, “The process of diffusion through a rubber membrane,” in *Proceedings of the Royal Society of London A: Mathematical, Physical and Engineering Sciences*, 1920, vol. 97, no. 685, pp. 286–307.

[85] M. A. V Devanathan and Z. Stachurski, “The mechanism of hydrogen evolution on iron in acid solutions by determination of permeation rates,” *J. Electrochem. Soc.*, vol. 111, no. 5, pp. 619–623, 1964.

[86] B. Scrosati, “Lithium rocking chair batteries: An old concept?,” *J. Electrochem. Soc.*, vol. 139, no. 10, pp. 2776–2781, 1992.

[87] C. J. Wen and R. A. Huggins, “Chemical diffusion in intermediate phases in the lithium-tin system,” *J. Solid State Chem.*, vol. 35, no. 3, pp. 376–384, 1980.

[88] A. Anani, S. Crouch-Baker, and R. A. Huggins, “Kinetic and thermodynamic parameters of several binary lithium alloy negative electrode materials at ambient temperature,” *J. Electrochem. Soc.*, vol. 134, no. 12, pp. 3098–3102, 1987.

[89] K. I. Pridatko, “Electrochemical insertion of lithium in thin tin films,” *Russ. J. Electrochem.*, vol. 42, no. 1, pp. 63–70, 2006.

[90] J. Xie *et al.*, “Li-ion diffusion behavior in Sn, SnO and SnO 2 thin films studied by galvanostatic intermittent titration technique,” *Solid State Ionics*, vol. 181, no. 35, pp. 1611–1615, 2010.

[91] E. C. W. Fok and J. D. Madden, “Measurement of the Diffusion Coefficient of Lithium in Tin Thin Films Including Phase Transformation Effects,” *ECS Trans.*, vol. 53, no. 30, pp. 131–142, 2013.

[92] D. X. Liu *et al.*, “In situ quantification and visualization of lithium transport with neutrons,” *Angew. Chemie Int. Ed.*, vol. 53, no. 36, pp. 9498–9502, 2014.

[93] J. Xie *et al.*, “Li-ion diffusion behavior in Sn, SnO and SnO2 thin films studied by galvanostatic intermittent titration technique,” *Solid State Ionics*, vol. 181, no. 35, pp. 1611–1615, 2010.

[94] A. He, Q. Liu, and D. G. Ivey, “Electrodeposition of tin: a simple approach,” *J. Mater. Sci. Mater. Electron.*, vol. 19, no. 6, pp. 553–562, 2008.

[95] C. Daniel and J. O. Besenhard, “Handbook of Battery Materials: Second Edition .” 2011.

[96] E. C. W. Fok, A. R. Usgaocar, A. Mahmoudzadeh, and J. D. W. Madden, “Measuring the Lithium Ion Diffusion Coefficient in Tin Thin Films: Comparisons Between Using Impedance Spectroscopy and Galvanostatic Intermittent Titration Technique,” in *Meeting Abstracts*, 2013, no. 14, p. 1024.

[97] A. V Churikov *et al.*, “Impedance spectroscopy of lithium-tin film electrodes,” *Russ. J. Electrochem.*, vol. 44, no. 5, pp. 550–557, 2008.

[98] H. Wu *et al.*, “Stable cycling of double-walled silicon nanotube battery anodes through solid-electrolyte interphase control,” *Nat. Nanotechnol.*, vol. 7, no. 5, pp. 310–315, 2012.

[99] A. J. Bard, L. R. Faulkner, J. Leddy, and C. G. Zoski, *Electrochemical methods: fundamentals and applications*. Wiley New York, 2000.

[100] R. W. Balluffi, "The supersaturation and precipitation of vacancies during diffusion," *Acta Metall.*, vol. 2, no. 2, pp. 194201–199202, 1954.

[101] H. W. Pickering, "Characteristic features of alloy polarization curves," *Corros. Sci.*, vol. 23, no. 10, pp. 1107–1120, 1983.

[102] K. Sieradzki, J. S. Kim, A. T. Cole, and R. C. Newman, "The Relationship Between Dealloying and Transgranular Stress-Corrosion Cracking of Cu-Zn and Cu-Al Alloys," *J. Electrochem. Soc.*, vol. 134, no. 7, pp. 1635–1639, 1987.

[103] I. C. Oppenheim, D. J. Trevor, C. E. D. Chidsey, P. L. Trevor, and K. Sieradzki, "In situ scanning tunneling microscopy of corrosion of silver-gold alloys," *Science (80-.).*, vol. 254, no. 5032, pp. 687–690, 1991.

[104] F. U. Renner, A. Stierle, H. Dosch, D. M. Kolb, T.-L. Lee, and J. Zegenhagen, "Initial corrosion observed on the atomic scale," *Nature*, vol. 439, no. 7077, pp. 707–710, 2006.

[105] R. Li and K. Sieradzki, "Ductile-brittle transition in random porous Au," *Phys. Rev. Lett.*, vol. 68, no. 8, p. 1168, 1992.

[106] A. Dursun, D. V Pugh, and S. G. Corcoran, "Dealloying of Ag-Au alloys in halide-containing electrolytes affect on critical potential and pore size," *J. Electrochem. Soc.*, vol. 150, no. 7, pp. B355–B360, 2003.

[107] J. Snyder, I. McCue, K. Livi, and J. Erlebacher, "Structure/processing/properties relationships in nanoporous nanoparticles as applied to catalysis of the cathodic oxygen reduction reaction," *J. Am. Chem. Soc.*, vol. 134, no. 20, pp. 8633–8645, 2012.

[108] X. Li *et al.*, "Dealloying of noble-metal alloy nanoparticles," *Nano Lett.*, vol. 14, no. 5, pp. 2569–2577, 2014.

[109] C. S. Kong, D.-Y. Kim, H.-K. Lee, Y.-G. Shul, and T.-H. Lee, "Influence of pore-size distribution of diffusion layer on mass-transport problems of proton exchange membrane fuel cells," *J. Power Sources*, vol. 108, no. 1, pp. 185–191, 2002.

[110] Y. K. Chen-Wiegart *et al.*, "Structural evolution of nanoporous gold during thermal coarsening," *Acta Mater.*, vol. 60, no. 12, pp. 4972–4981, 2012.

[111] H. Rösner, S. Parida, D. Kramer, C. A. Volkert, and J. Weissmüller, "Reconstructing a nanoporous metal in three dimensions: An electron tomography study of dealloyed gold leaf," *Adv. Eng. Mater.*, vol. 9, no. 7, pp. 535–541, 2007.

[112] Y. Wang and Y. Xia, "Bottom-up and top-down approaches to the synthesis of monodispersed spherical colloids of low melting-point metals," *Nano Lett.*, vol. 4, no. 10, pp. 2047–2050, 2004.

[113] H. Okamoto, *Binary Phase Diagrams*, II Ed. ASM International, 1990.

[114] A. J. Bard and L. R. Faulkner, *Electrochemical methods: fundamentals and applications*, 2nd ed. Wiley, Hoboken, NJ, 2000.